

R.J. Slager

# From elasticity to equations

Bachelorscriptie, 26 juni 2009

Scriptiebegeleider: dr. V. Rottschäfer



Mathematisch Instituut, Universiteit Leiden



# Contents

<b>1 Abstract</b>	<b>5</b>
<b>2 Setup, measurement procedure and data analysis</b>	<b>7</b>
2.1 Measurement procedure and setup . . . . .	7
2.1.1 Shear modulus . . . . .	7
2.1.2 bulk modulus . . . . .	11
2.2 data analysis . . . . .	15
2.2.1 shear modulus . . . . .	15
2.2.2 bulk modulus . . . . .	16
<b>3 Theory of elasticity</b>	<b>19</b>
3.1 Elasticity in 3-dimensional cartesian coordinates . . . . .	19
3.1.1 Strain in 3 dimensional cartesian coordinates . . . . .	19
3.1.2 Components of stress in 3-dimensional cartesian coordinates . . . . .	22
3.1.3 Hooke's law . . . . .	24
3.1.4 Bulk modulus . . . . .	26
3.2 Elasticity in 2-dimensional cartesian coordinates . . . . .	27
3.2.1 Strain in 2-dimensional cartesian coordinates . . . . .	27
3.2.2 Stress in 2-dimensional cartesian coordinates . . . . .	28
3.2.3 Elastic relations in 2-dimensional cartesian coordinates . . . . .	28
3.2.4 Bulk in two dimensional cartesian coordinates . . . . .	29
3.3 Elasticity in 2-dimensional polar coordinates . . . . .	29
3.3.1 Strain in 2 dimensional polar coordinates . . . . .	29
3.3.2 Stress in 2-dimensional polar coordinates . . . . .	31

3.3.3	Stress-balance in 2-dimensional polar coordinates . . . . .	31
3.3.4	Elastic relations in 2 dimensional polar coordinates . . . . .	33
3.3.5	Bulk modulus in two dimensional cartesian coordinates . . . . .	33
3.4	Theory applied to our experiment . . . . .	33
3.4.1	Shear modulus . . . . .	33
3.4.2	Bulk modulus . . . . .	35
<b>4</b>	<b>Results</b>	<b>39</b>
4.1	Shear modulus . . . . .	39
4.2	Bulk modulus . . . . .	50
<b>5</b>	<b>Frenkel-Kontorova model and sine-Gordon equation</b>	<b>61</b>
5.1	Formulation of the Frenkel-Kontorova model . . . . .	62
5.1.1	Hamiltonian systems . . . . .	62
5.1.2	Equation of motion . . . . .	64
5.2	Modes in the Frenkel-Kontorova system . . . . .	65
5.2.1	Pinned modes . . . . .	65
5.2.2	Sliding solutions . . . . .	66
5.3	The sine-Gordon equation . . . . .	68
5.3.1	Transformation of the sine-Gordon equation . . . . .	69
5.3.2	Soliton en breather solutions . . . . .	70
5.3.3	Lorentz invariance and solutions . . . . .	73
5.3.4	Hamiltonian, Lagrangian and phase portrait . . . . .	75
<b>6</b>	<b>Perturbation of the sine-Gordon equation</b>	<b>79</b>
6.1	General starting point . . . . .	79
6.2	Traveling waves with speed $c=1$ . . . . .	80
6.3	Traveling waves and the Melnikov function . . . . .	83
<b>7</b>	<b>Conclusion</b>	<b>87</b>
<b>8</b>	<b>Appendix</b>	<b>89</b>
8.1	<b>A1:</b> Image analysis . . . . .	89
8.2	<b>A2:</b> <i>idl</i> -code shear modulus . . . . .	90
8.3	<b>A3:</b> <i>idl</i> -code bulk modulus . . . . .	91
8.4	Acknowledgements . . . . .	93

# Chapter 1

## Abstract

This thesis deals with two main issues. 1; the elasticity of disordered materials. 2; the mathematics of systems consisting of elastic materials. It consists of two main parts.

### part 1

In the first part we present our experiments designated to measure the shear modulus,  $G$  and bulk modulus,  $B$ , of foams.

Essential in the description of disordered materials consisting of well defined elements, such as collection of grains or foams, is the concept of jamming. Jamming is the physical process by which these materials become rigid. The jamming transition happens when the density is increased; the crowding of the constituent particles prevents them from exploring phase space, making the aggregate material behave as a solid.

Instead of using the density we use the packing fraction,  $\phi$ , to describe the condition of the foam. The packing fraction refers to the fraction of the volume of the material that is occupied by the particles, and is obviously related to the density. The jamming point is characterized by a critical packing fraction denoted as  $\phi_c$ .

Data from simulations predicts that  $G \sim \sqrt{\Delta\phi}$  and that  $B$  is essentially independent of  $\Delta\phi$ , where  $\Delta\phi$  is defined as  $\phi - \phi_c$ . Our main aim is to verify these predictions empirically.

In chapter 2 we present our setup and strategy to measure  $B$  and  $G$ . These experiments are referred to as shear(modulus) experiment and bulk(modulus) experiment, respectively.

In chapter 3 we derive the elastic equations starting from a first order Taylor expansion. These equations fully describe the system and are implemented to derive equations for the shear modulus and bulk modulus in quantities pertaining to the measurements.

Subsequently we present the results of our measurements in chapter 4. Using the raw data we are able to compute plots of the shear modulus and bulk

modulus versus the packing fraction. This enables us to confirm the prediction for the shear modulus. Unfortunately, our data in the bulk experiment is not convincing enough to make a statement about the validity of the predictions for the bulk modulus.

## **part 2**

The second part deals with the mathematics and physics of systems consisting of two layers of bubbles in a Taylor-Couette geometry.

We consider each layer of bubbles as a chain of particles subordinated to a periodic potential, i.e. the other layer of bubbles. Additionally the interaction potential between the particles of the chain is approximated with a harmonic potential. The resulting model is known as the Frenkel-Kontorova model. This model and its Hamiltonian are presented in chapter 5.

Solving the Frenkel-Kontorova system in general is not possible, only under certain conditions solutions can be obtained. These solutions are described. Subsequently we take the continuum limit of the Frenkel-Kontorova model to obtain the sine-Gordon equation. This equation and its solutions will also be studied in some detail in chapter 5.

The sine-Gordon equation represents a Hamiltonian system, however we can easily add a dissipative term. The resulting equation is analyzed in chapter 6 using perturbation techniques. Using the Melnikov function, we are able to confirm the existence of traveling wave solutions and make some qualitative statements about them.

## Chapter 2

# Setup, measurement procedure and data analysis

### 2.1 Measurement procedure and setup

The experiments we have done are quite straight forward. The experiments concerning the shear modulus are done in a two-dimensional Taylor-Couette geometry. We rotate the inner wheel, which is connected to a rheometer, over a certain angle ( $\theta$ ) and measure the resultant torque ( $T$ ). The setup used in the bulk modulus experiments contains a reservoir with a fixed wall and a wiper, which is attached to the axis of the rheometer. A bidisperse monolayer of bubbles, placed in the compartment enclosed by the fixed wall and the wiper, is compressed as a torque ( $T$ ) is applied on the wiper. The resultant deflection angle  $\theta$  of the wiper is measured. The measured quantities in these experiments can directly be related to  $G$  and  $B$  respectively. In this section the measurement procedures and the corresponding setups are dealt with in detail.

#### 2.1.1 Shear modulus

The shear experiments are done in a two-dimensional Taylor-Couette geometry, shown in Figure 2.1. The rheometer(Anton-Paar dsr301) is the central element. The rheometer can apply very small torques or deflection angles<sup>1</sup> about an axis. Moreover the rheometer can measure the resultant deflection angle and torque, respectively, very accurately<sup>1</sup>.

The axis of the rheometer is connected to a gear wheel, situated in the reservoir, through a centered circular hole in the top plate(thickness 9 mm). In the experiments we use two wheels. One has a radius  $r_i$  of 5 cm and the other 2,5 cm. The circular reservoir has an outer radius  $r_o$  equal to 112.5 mm and has a height of 25 mm from the bottom to the top plate. Note that the outer radius is also grooved, providing no-slip boundary conditions.

---

<sup>1</sup> order  $\mu\text{Nm}$  and  $\mu$

Above the reservoir we place a mirror so that the foam can be imaged by the camera(baslerA622F) equipped with a lens(nikon sigma edxg).

The reservoir is situated on a stage which has three stands denoted by a,b and c, shown in Figure 2.1. Before the measurement we level the stage, by adjusting the three stands until the level confirms that stage is leveled.

When the stage is leveled we pour some soapy solution, consisting of 5 % volume fraction Dawn dishwashing liquid and 15 % glycerol in demineralized water (viscosity  $\eta = 1.8 \pm 0.1$  mPa·s and surface tension  $\sigma = 28 \pm 1$  mN/m), in a bowl. We create a bidisperse bubble monolayer, by flowing nitrogen through two syringe needles immersed at fixed depth in the solution. The resulting bubbles of  $1.8 \pm 0.1$  and  $2.7 \pm 0.1$  mm diameter(65:35 number ratio respectively) are gently mixed to produce a disordered bidisperse monolayer. The weighted average bubble diameter  $\langle d \rangle$  is 2.25 mm. We also fill the reservoir completely with soapy solution.

Subsequently we use a simple spoon to skim of the bubbles in the extern reservoir and transport them through the other circular hole in the glass plate, by putting them on top of the hole and extract some soapy solution from the sides of the reservoir. This creates a bidisperse monolayer in the reservoir trapped by a top plate.

We then make a picture of the bubble layer in order to determine its packing fraction with help of image analysis (for more details see appendix **A1**).

After calibrating the rheometer (which is done automatically by the programme) we perform the measurement. Each measurement is divided in a number of time intervals of equal length. During each interval the rheometer applies a certain deflection angle on the tooth-wheel in the center, and measures the resultant torque a designated number of times. In our experiment we take 200 measurement points per interval which where 0,3 second apart, resulting in 60 second intervals. Every interval the resultant torque relaxes to a certain equilibrium value. We ensure that the time-intervals are long enough to let the system attain its equilibrium value.

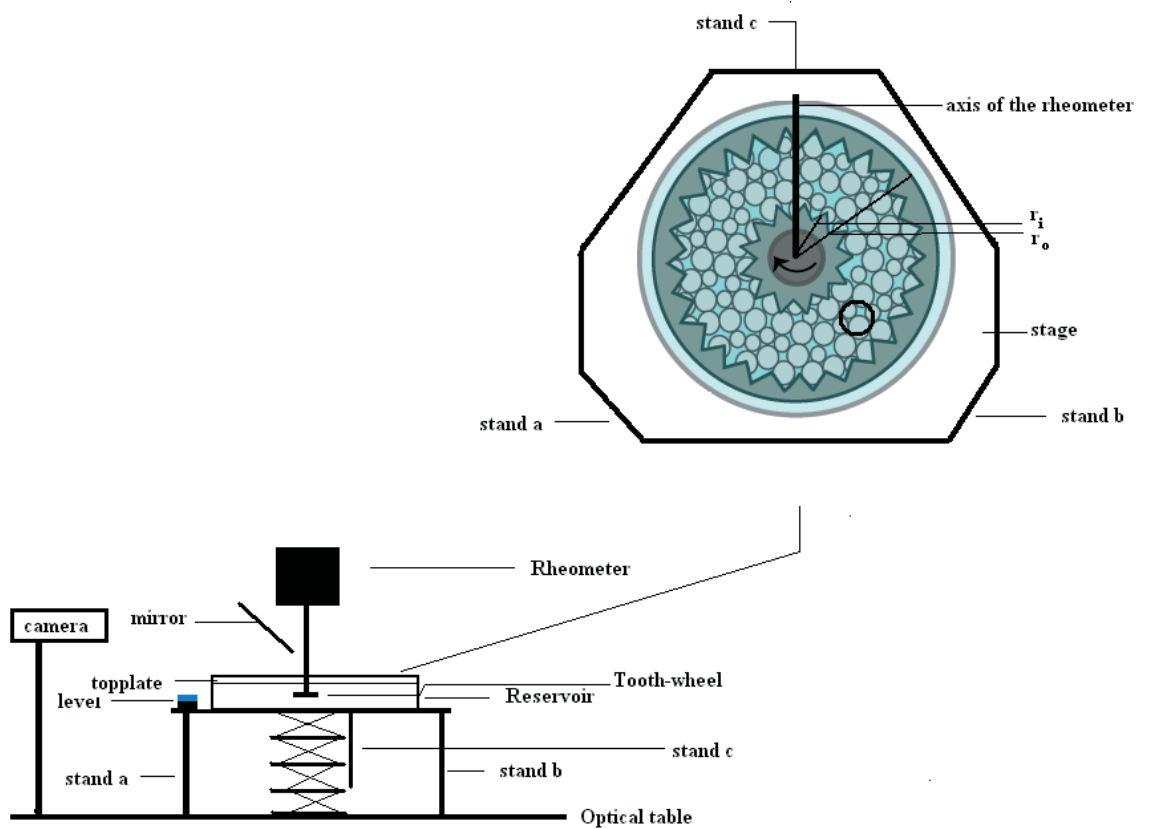


Figure 2.1: *Schematic representation of the setup of the shear experiment. On the right hand side an enlarged schematic representation of the stage on which the reservoir is situated, is shown.*

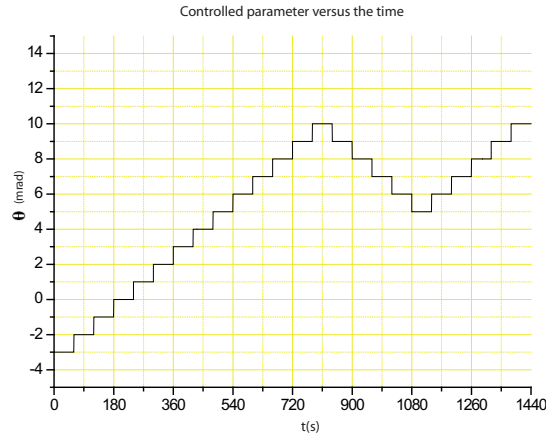


Figure 2.2: Plot of the controlled parameter  $\theta$  versus the time. Recall that our intervals last 60 seconds.

The controlled parameter  $\theta$  is increased and decreased during the measurement in single steps, in order to check whether the system has linear response. Additionally as we impose the same value of  $\theta$  on the wheel several times, we can also see whether the data reproduces. The measurements consist of 24 intervals. Each measurement  $\theta$  equals -3 milirad during the first interval, reached in a single step. Then  $\theta$  ascends one milirad every interval until it has reached a value of 10 milirad. After the fourteenth interval we let  $\theta$  descend a milirad per interval for five intervals. During the last five intervals  $\theta$  is again increased one milirad every interval (Fig. 2.2). The resultant measurement points and their corresponding deflection angle, time and resultant  $T$  are saved in a table by the software used to control the rheometer. Moreover the measured torque as function of time is recorded by the rheometer's software.

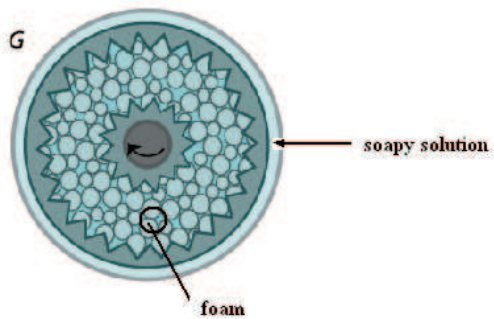


Figure 2.3: *An other schematic representation of the reservoir used in the shear modulus experiment. The tooth-wheel is rotated a certain amount with help of the rheometer, the resultant torque are measured. The packing fraction can be varied by adding or subtracting soapy solutions from the sides.*

When we are done with the measurements at this particular packing fraction, we vary the packing fraction. This can easily be done by adding some soapy solution, which then pushes some bubbles out the reservoir making the foam wetter(Fig.2.3). The packing fraction of the foam can be increased, i.e. making the foam dryer, by subtracting some soapy solution from the sides in order to get some more bubbles in the Taylor-Couette geometry (without creating double layers of bubbles). We again make a picture to determine the new packing fraction and subsequently do some measurements. This process is repeated at several packing fractions, resulting in sets of data for various packing fractions.

### 2.1.2 bulk modulus

For the bulk experiment the reservoir used in the shear experiment is replaced, creating a whole new geometry in a quite similar setup (Fig. 2.4). The new reservoir contains two fixed walls and a smooth outer radius. Moreover it has the same dimensions as the reservoir used in the shear experiments. The top plate, which is also used in the shear experiments, is placed on the reservoir. The axis of the rheometer is connected to a wiper, which has arms  $r'$  that are 97 mm long(Fig. 2.4).

The mirror is placed is such a way that the camera, which is the same one encountered in the previous experiment, can take pictures of the compartment enclosed by the wiper and fixed wall.

After leveling the stage, on which the reservoir is situated, we make bidisperse bubble monolayer similar to the one in the shear experiment.

Subsequently we transport the bubbles in the compartment enclosed by the wiper and the solid wall through the circular hole using a spoon. Finally the glass plate is rotated in order to transport the circular hole away from the

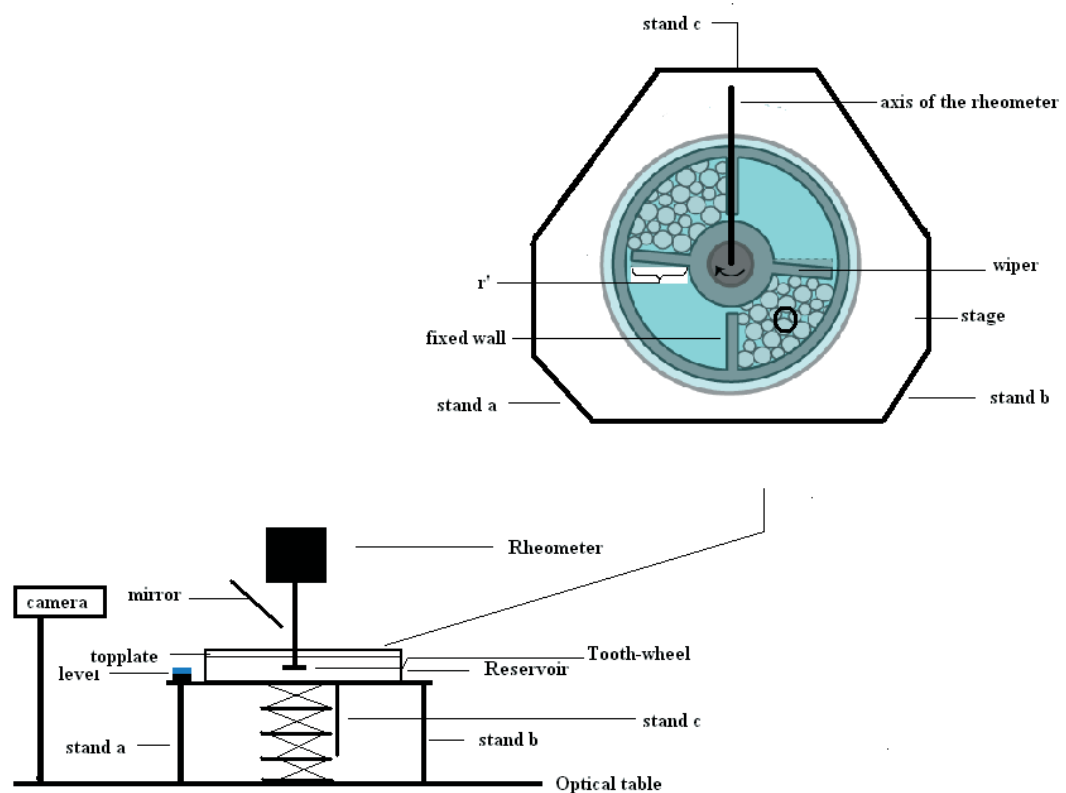


Figure 2.4: *Schematic representation of the setup of the bulk modulus experiment. An enlarged schematic representation of stage with the new reservoir is enlarged and shown on the right.*

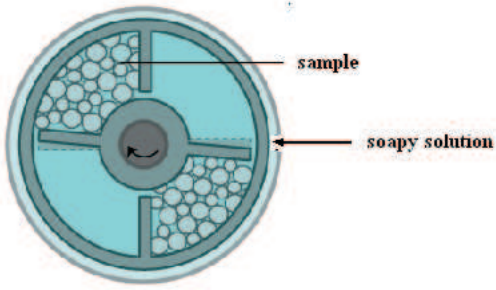


Figure 2.5: *Schematic representation of the reservoir used in the bulk modulus. The wiper compresses the foam as a certain amount of torque is applied on the wiper in each interval. The resulting deflection angle is measured.*

compartment of bubbles, to prevent the bubbles from escaping as the wiper starts the compression of the compartment filled with the bubbles.

Then, the measurement can be started. Again we divide the measurement in intervals. During every interval the wiper is applied with a constant torque  $T$ . The wiper then compresses the bubble layer (Fig. 2.5), by diminishing the compartment enclosed by the fixed wall, wiper, soapy solution and top plate. The resultant deflection angle  $\theta$  is measured at the designated measuring points. The intervals are long enough to let the wiper attain its equilibrium value. The measurements are divided in 16 or 8 intervals. Every interval consists of 300 measuring points, which are parted by 0.3 second resulting in intervals of 1,5 minute.

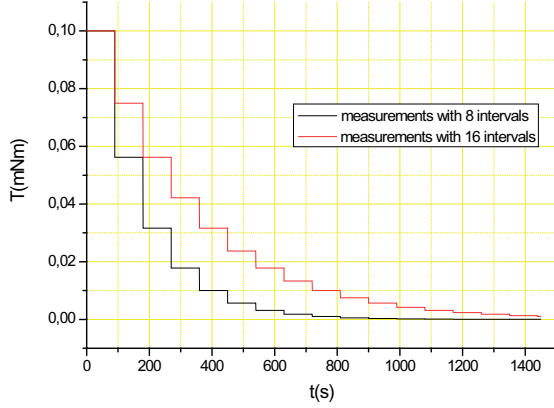


Figure 2.6: Plots of the controlled parameter  $T$  versus time  $t$ , for the measurements consisting of 8 and 16 intervals. Remember that the measurements consist of 90 second intervals,

We take logarithmic steps for  $T$  (Fig. 2.6). Or to put it in formalistic language, the torque in mNm is a simple function of the index  $i$  of the interval. When the measurement consists of sixteen interval this function is <sup>2</sup>

$$T(mNm) = (10)^{-\frac{(7+i)}{8}} \quad (2.1)$$

For the measurements consisting of 8 intervals this function is modified to<sup>2</sup>,

$$T(mNm) = (10)^{-\frac{(3+i)}{4}} \quad (2.2)$$

Note that every interval the system is compressed, so the packing fraction alters as it relaxes to a new equilibrium. Therefore we take pictures every 0.5 second to ensure we can calculate the packing fraction at the reached equilibria. The time, torque and resultant deflection angle are stored by the rheometer's software.

---

<sup>2</sup> with  $i$  in the appropriate range

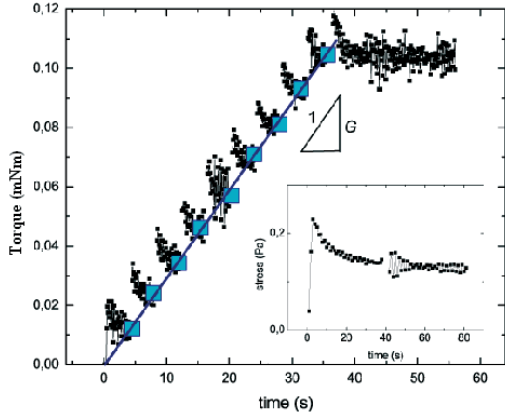


Figure 2.7: *The typical Torque as a function of time, measured in our quasi-static experiment.*

## 2.2 data analysis

*In this section the steps used to analyze the data are presented. The analysis for both the shear modulus and bulk modulus experiments are shown in steps, which gives a kind of 'algorithm-like' touch but ensures that the data is presented in a rather clear and structured way.*

### 2.2.1 shear modulus

#### step 1 exporting the data

First of all the table with the measurement points and their deflection angle are exported as tex-files. The column of the torque is then extracted from this table and loaded in an *idl*-program. The column with the torques measured at the measuring points is also loaded in *origin* in order to look at the data. We can then already mark the measurements displaying rearrangements.

#### step 2 Analysis with *idl*

**step 2a** The plot of the torque versus the time typically looks like the graph displayed in figure 2.7. We measure in the elastic response region (see Chapter " Theory of elasticity " for more details). As the system relaxes, one can expect that the system will reach equilibrium like a damped harmonic oscillator, since in the elastic approximation the system is treated as a harmonic system, with a damping coefficient. Due to dragforces exerted by the top plates this comparative description is not entirely valid. However, motivated by the empirical results, we fitted the data of every interval with a natural exponent. This is done by a simple *idl*-script (see appendix A2). The column with the torque is loaded into the program. Then for every interval the data is fitted with a exponent, i.e.  $A + B \exp(-\frac{t}{\tau})$ , where  $\tau$  has the interpretation of a characteristic

time. These plots are exported and saved. Notice however that every point represents 0,3 second as the measurement points are 0,3 second apart rather than one second. The  $A$ , that represents the value of the torque the system relaxes to every interval of the measurement, and the characteristic time  $\tau$  are stored in array.

**step 2b** The value of  $A$  of each interval is put in a plot versus the deflection angle( $\theta$ ) of the inner wheel in that interval. Subsequently a line is fitted to these points, to determine the slope, i.e. the ratio between the torque  $T$  and deflection angle  $\theta$  in that measurement. This final plot is also exported and saved, as well as the parameters of the fit (Fig. 2.7). These parameters give already a rough indication of the ratio of  $T$  and  $\theta$ . However we can not trust them a priori due to possible rearrangements.

#### **step 3** *Verification step*

If there are rearrangements, the corresponding points should be omitted to find the correct ratio between torque and deflection angle. We load the array with the values of  $A$  of each interval in origin and plot these points as function of  $\theta$ . The points, corresponding to rearrangements are omitted. Subsequently we fit a line through the data. The slope of the line, i.e. the ratio of  $T$  and  $\theta$ , is compared with value obtained from the *idl*-script.

#### **step 4** *Determining the packing fraction*

The packing fraction is determined from the picture taken with help of an other *idl*-program (See appendix A1 for more details).

#### **step 5** *processing the data*

From the ratio of  $T$  and  $\theta$ , obtained using *origin*, the shear modulus is calculated with help of formula 3.73. Recall that during some measurements we used an inner wheel with a radius of 25 mm while during other measurements we used a wheel with a radius of 50 mm. In *origin* we make a table. The measurement is put in the table along with the number of this measurement the packing fraction, shear modulus and the radius of the inner wheel used. Subsequently  $G$  is plotted versus  $\phi$ .

## 2.2.2 bulk modulus

#### **step 1** *exporting the data*

First of all, the table with the measurement point and their resultant deflection angle  $\theta$  are exported as tex-files. The column containing  $\theta$  of each measurement point is then extracted from this table and loaded in an other *idl*-program (see appendix A3).

#### **step 2** *Analysis with idl*

**step 2a** The plot of  $\theta$  versus the time typically looks like the graph displayed in figure 2.8. In the *idl*-program we again fit each interval with a natural exponent, i.e.  $A + B \exp(-\frac{t}{\tau})$ . These fits are also exported and saved. The values of  $A$  represent the angle the wiper relaxes to during that interval and are stored in an array. We will denote this values by  $\theta_e(i)$ . Where the  $i$  is the index of the interval.

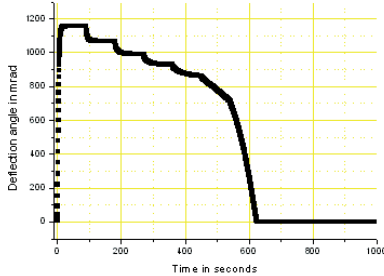


Figure 2.8: *The deflection of the wiper, used in the bulk experiments, as a function of time, due to the various constant torques put on the wiper during the intervals. This is a example how our data looks like.*

### **step 3 Determining the packing fraction**

The packing fraction is determined from the pictures taken during the measurement. The best<sup>3</sup> picture of the system in equilibrium, in that interval, is selected. It is very easy to determine whether the system has reached equilibrium by looking at the motion of wiper and bubbles. In equilibrium the wiper and bubbles do not move anymore. With help of the same programme used in the shear modulus experiment the packing fraction from this interval is then determined from this picture (See appendix A1 for more details).

### **step 4 Calculating the angles in equilibrium and making the table**

The picture used to analyze the data is also used to calculate  $\theta_v(i)$ , i.e. the angle of the compartment in equilibrium during interval  $i$ . This can easily be done with help of the program *ImageJ*. We basically load the picture<sup>4</sup> in the program and draw lines over the edges of the compartment enclosed by the fixed wall and the wiper. The program calculates the angle between these lines. Then we calculate  $\Delta\theta = \theta_e(i+1) - \theta_e(i)$  and  $\Delta T = T(i+1) - T(i)$  where  $T(i)$  denotes the torque at interval  $i$ . Subsequently,  $G+B$  is calculated with help of formula 3.85. Using the table and the results from the previous experiment, the bulk modulus can be plotted versus the packing fraction.

---

<sup>3</sup>With best we mean the picture which shows the best contrast between the bubbles and the bottom of the reservoir

<sup>4</sup>Which is scaled t

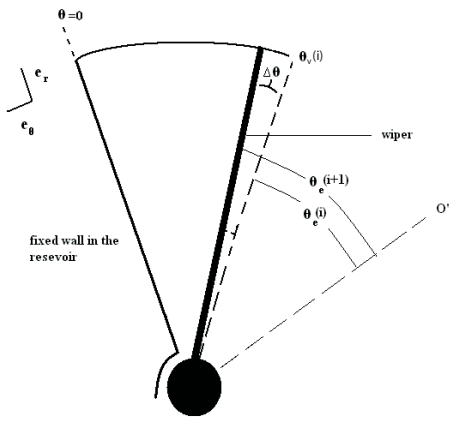


Figure 2.9: *Schematic illustration of the compartment and the corresponding angles.*

# Chapter 3

## Theory of elasticity

*This chapter will deal with the concepts of stress and strain, and their relating equations. Starting from a simple Taylor expansion I will derive some general results, in a rather alternative manner. From these general results I shall then derive some equations describing the physics of our specific experiments.*

*Generally, the displacement of a body has two components; a rigid-body displacement, i.e. translations and rotations that do not alter the body's size, and a deformation, which is the change in shape and/or size of the body from an initial or undeformed configuration. However, in this discussion of the displacement of a continuum body it will assumed that there are enough physical constraints to prevent the body from moving as a rigid body, so that no displacements of particles of the body are possible without a deformation of it. Which is obviously the case in our experiments.*

### 3.1 Elasticity in 3-dimensional cartesian coordinates

#### 3.1.1 Strain in 3 dimensional cartesian coordinates

Consider a continuum body and a three dimensional cartesian coordinate-system, with standard variables x,y and z. A change in the configuration of the body results in a displacement. This can be represented by a vector-field;  $\psi: \mathbb{R}^3 \rightarrow \mathbb{R}^3$ , with components  $u_i(x, y, z)$ ,  $i \in \{1, 2, 3\}$ , which are assumed to be very small and continuously varying over the volume of the body. Therefore it is justified to apply a Taylor expansion up to first order to calculate the displacement of the body, i.e. an elastic approximation.

To implement this idea consider a small element,  $dx, dy, dz$ <sup>1</sup> (Fig. 3.1), of the body around a point  $\vec{\varrho}$ <sup>2</sup> undergoing such a displacement. We can use the Taylor expansion to approximate  $\phi(\vec{\alpha})$

---

<sup>1</sup>of course  $dx, dy, dz$  are parallel to the x-axis, y-axis and z-axis respectively.

<sup>2</sup>where the notation  $\vec{\varrho}_x$  is used to denote the x-component of  $\vec{\varrho}$

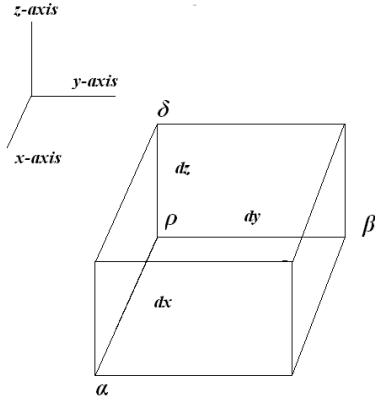


Figure 3.1: Small cubic element around a point  $\rho$  in the body.  $dx, dy$  and  $dz$  are parallel to the  $\hat{x}, \hat{y}$  and  $\hat{z}$  direction respectively. The points  $\alpha, \beta$  and  $\delta$  are approximated with a first order Taylor expansion, as the element is assumed to be very small.

$$\phi(\vec{\alpha}) \approx \begin{bmatrix} u_1(\vec{\rho}) \\ u_2(\vec{\rho}) \\ u_3(\vec{\rho}) \end{bmatrix} + \begin{bmatrix} \frac{\partial u_1(\vec{\rho})}{\partial x} & \frac{\partial u_1(\vec{\rho})}{\partial y} & \frac{\partial u_1(\vec{\rho})}{\partial z} \\ \frac{\partial u_2(\vec{\rho})}{\partial x} & \frac{\partial u_2(\vec{\rho})}{\partial y} & \frac{\partial u_2(\vec{\rho})}{\partial z} \\ \frac{\partial u_3(\vec{\rho})}{\partial x} & \frac{\partial u_3(\vec{\rho})}{\partial y} & \frac{\partial u_3(\vec{\rho})}{\partial z} \end{bmatrix} (\vec{\rho} - \vec{\alpha}) \quad (3.1)$$

Using the fact that  $dx$ , the line element that connects  $\vec{\rho}$  and  $\vec{\alpha}$ , is parallel to the x axis equation 1.1 reduces to

$$\phi(\vec{\alpha}) \approx \begin{bmatrix} u_1(\vec{\rho}) \\ u_2(\vec{\rho}) \\ u_3(\vec{\rho}) \end{bmatrix} + \begin{bmatrix} \frac{\partial u_1(\vec{\rho})}{\partial x} & \frac{\partial u_1(\vec{\rho})}{\partial y} & \frac{\partial u_1(\vec{\rho})}{\partial z} \\ \frac{\partial u_2(\vec{\rho})}{\partial x} & \frac{\partial u_2(\vec{\rho})}{\partial y} & \frac{\partial u_2(\vec{\rho})}{\partial z} \\ \frac{\partial u_3(\vec{\rho})}{\partial x} & \frac{\partial u_3(\vec{\rho})}{\partial y} & \frac{\partial u_3(\vec{\rho})}{\partial z} \end{bmatrix} \begin{bmatrix} dx \\ 0 \\ 0 \end{bmatrix} \quad (3.2)$$

In exactly the same manner one obtains the following equations for  $\phi(\vec{\beta})$  and  $\phi(\vec{\delta})$  respectively

$$\phi(\vec{\beta}) \approx \begin{bmatrix} u_1(\vec{\rho}) \\ u_2(\vec{\rho}) \\ u_3(\vec{\rho}) \end{bmatrix} + \begin{bmatrix} \frac{\partial u_1(\vec{\rho})}{\partial x} & \frac{\partial u_1(\vec{\rho})}{\partial y} & \frac{\partial u_1(\vec{\rho})}{\partial z} \\ \frac{\partial u_2(\vec{\rho})}{\partial x} & \frac{\partial u_2(\vec{\rho})}{\partial y} & \frac{\partial u_2(\vec{\rho})}{\partial z} \\ \frac{\partial u_3(\vec{\rho})}{\partial x} & \frac{\partial u_3(\vec{\rho})}{\partial y} & \frac{\partial u_3(\vec{\rho})}{\partial z} \end{bmatrix} \begin{bmatrix} dy \\ 0 \\ 0 \end{bmatrix} \quad (3.3)$$

$$\phi(\vec{\delta}) \approx \begin{bmatrix} u_1(\vec{\rho}) \\ u_2(\vec{\rho}) \\ u_3(\vec{\rho}) \end{bmatrix} + \begin{bmatrix} \frac{\partial u_1(\vec{\rho})}{\partial x} & \frac{\partial u_1(\vec{\rho})}{\partial y} & \frac{\partial u_1(\vec{\rho})}{\partial z} \\ \frac{\partial u_2(\vec{\rho})}{\partial x} & \frac{\partial u_2(\vec{\rho})}{\partial y} & \frac{\partial u_2(\vec{\rho})}{\partial z} \\ \frac{\partial u_3(\vec{\rho})}{\partial x} & \frac{\partial u_3(\vec{\rho})}{\partial y} & \frac{\partial u_3(\vec{\rho})}{\partial z} \end{bmatrix} \begin{bmatrix} 0 \\ 0 \\ dz \end{bmatrix} \quad (3.4)$$

The first terms in equations 3.2,3.3 and 3.4 are the translations. Using the assumed continuity of  $\psi$  and the obvious linearity of its first order Taylor expansion one can find  $\phi(dx) \equiv dx'$ ,  $\phi(dy) \equiv dy'$ ,  $\phi(dz) \equiv dz'$ , up to first order, by calculating  $\phi(\vec{\alpha}) - \phi(\vec{\rho})$ ,  $\phi(\vec{\beta}) - \phi(\vec{\rho})$ ,  $\phi(\vec{\delta}) - \phi(\vec{\rho})$  respectively. These are exactly the deformations we were looking for.

$$dx' \approx \phi(\vec{\alpha}) - \phi(\vec{\rho}) \approx \begin{bmatrix} u_1(\vec{\rho}) \\ u_2(\vec{\rho}) \\ u_3(\vec{\rho}) \end{bmatrix} + \begin{bmatrix} \frac{\partial u_1(\vec{\rho})}{\partial x} & \frac{\partial u_1(\vec{\rho})}{\partial y} & \frac{\partial u_1(\vec{\rho})}{\partial z} \\ \frac{\partial u_2(\vec{\rho})}{\partial x} & \frac{\partial u_2(\vec{\rho})}{\partial y} & \frac{\partial u_2(\vec{\rho})}{\partial z} \\ \frac{\partial u_3(\vec{\rho})}{\partial x} & \frac{\partial u_3(\vec{\rho})}{\partial y} & \frac{\partial u_3(\vec{\rho})}{\partial z} \end{bmatrix} \begin{bmatrix} 0 \\ 0 \\ dz \end{bmatrix} - \begin{bmatrix} u_1(\vec{\rho}) \\ u_2(\vec{\rho}) \\ u_3(\vec{\rho}) \end{bmatrix} \quad (3.5)$$

Resulting in the following equation;

$$dx' \approx \begin{bmatrix} \frac{\partial u_1(\vec{\rho})}{\partial x} & \frac{\partial u_1(\vec{\rho})}{\partial y} & \frac{\partial u_1(\vec{\rho})}{\partial z} \\ \frac{\partial u_2(\vec{\rho})}{\partial x} & \frac{\partial u_2(\vec{\rho})}{\partial y} & \frac{\partial u_2(\vec{\rho})}{\partial z} \\ \frac{\partial u_3(\vec{\rho})}{\partial x} & \frac{\partial u_3(\vec{\rho})}{\partial y} & \frac{\partial u_3(\vec{\rho})}{\partial z} \end{bmatrix} \begin{bmatrix} dx \\ 0 \\ 0 \end{bmatrix} \quad (3.6)$$

Analogously one finds  $dy'$ ,  $dz'$

$$dy' \approx \begin{bmatrix} \frac{\partial u_1(\vec{\rho})}{\partial x} & \frac{\partial u_1(\vec{\rho})}{\partial y} & \frac{\partial u_1(\vec{\rho})}{\partial z} \\ \frac{\partial u_2(\vec{\rho})}{\partial x} & \frac{\partial u_2(\vec{\rho})}{\partial y} & \frac{\partial u_2(\vec{\rho})}{\partial z} \\ \frac{\partial u_3(\vec{\rho})}{\partial x} & \frac{\partial u_3(\vec{\rho})}{\partial y} & \frac{\partial u_3(\vec{\rho})}{\partial z} \end{bmatrix} \begin{bmatrix} 0 \\ dy \\ 0 \end{bmatrix} \quad (3.7)$$

$$dz' \approx \begin{bmatrix} \frac{\partial u_1(\vec{\rho})}{\partial x} & \frac{\partial u_1(\vec{\rho})}{\partial y} & \frac{\partial u_1(\vec{\rho})}{\partial z} \\ \frac{\partial u_2(\vec{\rho})}{\partial x} & \frac{\partial u_2(\vec{\rho})}{\partial y} & \frac{\partial u_2(\vec{\rho})}{\partial z} \\ \frac{\partial u_3(\vec{\rho})}{\partial x} & \frac{\partial u_3(\vec{\rho})}{\partial y} & \frac{\partial u_3(\vec{\rho})}{\partial z} \end{bmatrix} \begin{bmatrix} 0 \\ 0 \\ dz \end{bmatrix} \quad (3.8)$$

The increase in length of  $dx$  in the  $\hat{x}$  direction due to deformation is obviously  $\psi(dx) - dx = \frac{\partial u_1(\vec{\rho})}{\partial x} dx - dx$ . Additionally its unit elongation in this direction,  $\gamma_{xx}$ , can easily be found upon dividing the found component by  $dx$

$$\gamma_{xx} = \frac{\partial u_1(\vec{\rho})}{\partial x} \frac{1}{dx} = \frac{\partial u_1(\vec{\rho})}{\partial x} \quad (3.9)$$

Likewise we obtain  $\gamma_{yy} = \frac{\partial u_2(\vec{\rho})}{\partial y}$  and  $\gamma_{zz} = \frac{\partial u_3(\vec{\rho})}{\partial z}$  to be the unit elongations of  $dy$  and  $dz$  in the  $\hat{y}$ -direction and  $\hat{z}$ -direction respectively.

Now the distortion of the angles between  $dx$ ,  $dy$  and  $dz$  has to be taken into account. For that purpose consider the angle between  $dx$  and  $dy$  after a displacement (Fig.3.2). Using equations 3.6 and 3.7 one finds that for  $dx$  the deformation in the  $y$ -direction equals  $\frac{\partial u_2(\vec{\rho})}{\partial x}(dx)$ . Likewise  $dy$  has a displacement in the  $x$ -direction given by;  $\frac{\partial u_1(\vec{\rho})}{\partial y}(dy)$ .

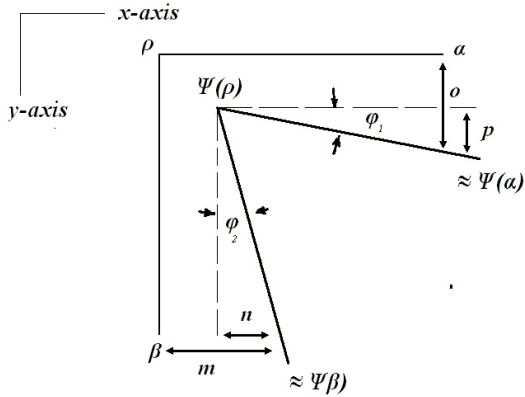


Figure 3.2: *Schematic illustration of the distortion in angle between  $dx$  and  $dy$ , resulting in the new angle between  $dx'$  and  $dy$ . This illustration looks the same for the angle between  $dx$  and  $dz$  and  $dy$  and  $dz$ . As can be seen from equations 3.2 and 3.3  $m = u_1(\vec{\rho}) + \frac{\partial u_1(\rho)}{\partial y}(dy)$  and  $o = u_2(\vec{\rho}) + \frac{\partial u_2(\rho)}{\partial x}(dx)$ . Accordingly, equations 3.6 3.7 determine  $n$  and  $p$ ;  $n = \frac{\partial u_1(\rho)}{\partial y}(dy)$ ,  $p = \frac{\partial u_2(\rho)}{\partial x}(dx)$ .*

As first order Taylor approximation is being used  $\varphi_1 = \tan \varphi_1 = \frac{\frac{\partial u_2(\rho)}{\partial x}(dx)}{dx} = \frac{\partial u_2(\rho)}{\partial x}$ . Similarly  $\varphi_2 = \frac{\partial u_1(\rho)}{\partial y}$ . Therefore the angle between  $dx$  and  $dy$  after the deformation is diminished by  $\frac{\partial u_2(\rho)}{\partial x} + \frac{\partial u_1(\rho)}{\partial y}$ . Applying the same method and equation 3.8 in combination with 3.6 and 3.7 to calculate the distortion of angle between  $dx$  and  $dz$ , and  $dy$  and  $dz$  respectively one obtains  $\gamma_{xz} = \frac{\partial u_1(\rho)}{\partial z} + \frac{\partial u_3(\rho)}{\partial x}$  and  $\gamma_{yz} = \frac{\partial u_2(\rho)}{\partial z} + \frac{\partial u_3(\rho)}{\partial y}$ .

Using the symmetry of the found components it is immediately clear that  $\gamma_{ab} = \gamma_{ba}$ , with  $a, b \in \{x, y, z\}$ . Thus we have found the components of strain in three dimensional coordinates, which can be represented in matrix-form.

$$\begin{bmatrix} \gamma_{xx} & \gamma_{xy} & \gamma_{xz} \\ \gamma_{yx} & \gamma_{yy} & \gamma_{yz} \\ \gamma_{zx} & \gamma_{zy} & \gamma_{zz} \end{bmatrix} = \begin{bmatrix} \frac{\partial u_1(\vec{\rho})}{\partial x} & \frac{\partial u_2(\vec{\rho})}{\partial x} + \frac{\partial u_1(\vec{\rho})}{\partial y} & \frac{\partial u_1(\vec{\rho})}{\partial z} + \frac{\partial u_3(\vec{\rho})}{\partial x} \\ \frac{\partial u_2(\vec{\rho})}{\partial x} + \frac{\partial u_1(\vec{\rho})}{\partial y} & \frac{\partial u_2(\vec{\rho})}{\partial y} & \frac{\partial u_2(\vec{\rho})}{\partial z} + \frac{\partial u_3(\vec{\rho})}{\partial y} \\ \frac{\partial u_1(\vec{\rho})}{\partial z} + \frac{\partial u_3(\vec{\rho})}{\partial x} & \frac{\partial u_2(\vec{\rho})}{\partial z} + \frac{\partial u_3(\vec{\rho})}{\partial y} & \frac{\partial u_3(\vec{\rho})}{\partial z} \end{bmatrix} \quad (3.10)$$

### 3.1.2 Components of stress in 3-dimensional cartesian coordinates

There are two kinds of forces that may act on the body. On one hand there are the forces distributed over the surface of the body, like pressure of one body on an other body or hydrostatic pressure. These forces are denoted by surface

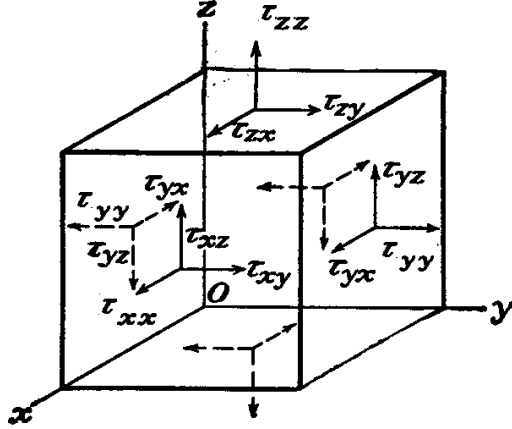


Figure 3.3: *Schematic illustration of the forces resolved in the direction of the basis-elements of the three dimensional cartesian coordinate system*

forces. On the other hand there are forces distributed over the volume of the body like gravity, magnetic forces inertia forces when the body is in motion. These forces are referred to as body forces.

Consider our small cubic element again(Fig.3.3), experiencing surface forces. One can resolve the surface forces per unit of area in the direction of the basis, i.e. in this case the x-direction, y-direction and z-direction. Each plane thus has one force per unit area perpendicular to that plane, a normal stress, and two forces per unit area with a direction parallel, the so-called shearing stresses. For example for the plane perpendicular to the x-axis one has the following forces per unit area;  $\tau_{xx}$ ,  $\tau_{yx}$  and  $\tau_{zx}$ . Here the first subscript indicates the direction of the force<sup>3</sup>, and the second subscript denotes the axis to which the plane is perpendicular to. This thus results in 9 components of stress which can be represented in matrix-form

$$\begin{bmatrix} \tau_{xx} & \tau_{xy} & \tau_{xz} \\ \tau_{yx} & \tau_{yy} & \tau_{yz} \\ \tau_{zx} & \tau_{zy} & \tau_{zz} \end{bmatrix} \quad (3.11)$$

However in equilibrium some simple considerations can reduce the number of shearing stresses from 6 to 3. When a body is in equilibrium there are no effective moments, by definition. So consider a small area perpendicular to the x-axis. As there is no effective moment we obtain the following identity;

$$\tau_{zy} dx dy dz = \tau_{yz} dx dy dz \implies \tau_{zy} = \tau_{yz} \quad (3.12)$$

---

<sup>3</sup>the stress or strain is considered positive in this discussion if the part of the force resolved in that direction points in the positive direction with respect to the basis.

Analogously using planes perpendicular to the y-axis and z-axis the following identities can be derived, which effectively ensure that the matrix in equation 3.11 is symmetric

$$\tau_{xy} = \tau_{yx} \quad (3.13)$$

$$\tau_{zx} = \tau_{xz} \quad (3.14)$$

### 3.1.3 Hooke's law

The relations between stresses and strain are described by the empirical verified law of Hooke. Imagine an elemental rectangular piece of isotropic material with sides parallel to the axes and submitted to normal stresses  $\tau_{xx}$  distributed uniformly. Experiments show that in this case there is no distortion of angles and that the ratio of the magnitude of unit elongation and the stress is constant, denoted by  $E$ . <sup>4</sup> This constant is referred to as the modulus of elasticity in tension.

$$\tau_{xx} = \gamma_{xx} E \quad (3.15)$$

However, as one can imagine, in the elastic regime extension of the element in the x-direction is accompanied by lateral contractions, in the  $\hat{y}$  and  $\hat{z}$  directions. These are also, verified empirically, related by a constant,  $\nu$ , called the Poisson ratio;

$$\gamma_{yy} = -\frac{\nu \tau_{xx}}{E}, \quad \gamma_{zz} = -\frac{\nu \tau_{xx}}{E} \quad (3.16)$$

If our element is submitted to the action of normal stresses, uniformly distributed over the sides, one can easily obtain the resultant strain components using the superposition principle and equations 1.14 and 1.15. This method of superposition is obviously only valid in this regime of very small deformations as the strain components are then linear and changes in dimension of the body and small displacements of the points of application due to external forces can safely be neglected. Thus we obtain the following set of equations relating normal stresses and unit elongations;

$$\gamma_{xx} = \frac{1}{E} (\tau_{xx} - \nu(\tau_{yy} + \tau_{zz})) \quad (3.17)$$

$$\gamma_{yy} = \frac{1}{E} (\tau_{yy} - \nu(\tau_{xx} + \tau_{zz})) \quad (3.18)$$

$$\gamma_{zz} = \frac{1}{E} (\tau_{zz} - \nu(\tau_{xx} + \tau_{yy})) \quad (3.19)$$

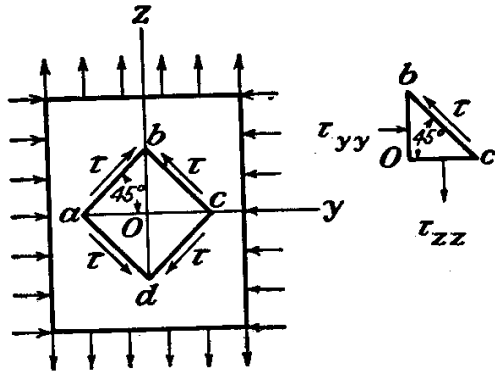


Figure 3.4: *Schematic illustration of the cross-section of the rectangular parallelepiped, experiencing pure shear, cut parallel to the x-axis. With the triangle  $Obc$  shown enlarged next to it.*

Additionally one can find a relation between the shearing strain and shear stress. This must depend on  $\nu$  and  $E$  of course, as these completely determine the response of the material by the preceding equations.

Consider a rectangular parallelepiped with  $\tau_{yy} = \tau_{zz}$  and  $\tau_{xx} = 0$ . Cutting out an element parallel to the x-axis and at 45 degrees to the z-axis and y-axis (Fig. 3.4), it is easy to see that the forces along and perpendicular to bc add to zero. Which means that the normal stresses are equal to zero. Moreover for the shearing stresses on the sides it holds that  $\tau = \frac{1}{2}(\tau_{zz} - \tau_{yy}) = \tau_{zz}$ . This is called pure shear.

Vertical elongation of  $Ob$  is equal to the shortening of  $Oa$  and  $Oc$ . Neglecting all quantities of at least second order, one must conclude that the lengths of  $ab$  and  $bc$  do not change as result of the deformation. The angle does change and the shearing strain  $\gamma$  me easily be found by examining triangle  $Obc$ .

As a result of the deformation one finds;

$$\frac{Oc}{Ob} = \tan\left(\frac{\pi}{4} - \frac{\gamma}{2}\right) = \frac{1 + \gamma_{yy}}{1 + \gamma_{zz}} \quad (3.20)$$

Inserting the elastic equations

$$\begin{aligned} \gamma_{zz} &= \frac{1}{E}(\tau_{zz} - \nu\tau_{yy}) = \frac{(1+\nu)\tau_{zz}}{E} \\ \gamma_{yy} &= -\frac{(1+\nu\tau_{zz})}{E} \end{aligned} \quad (3.21)$$

For small  $\gamma$  we can approximate as follows;

---

<sup>4</sup>It is still assumed that we are dealing with very small displacements, i.e. an elastic approximation. This will only be valid up to a certain yield stress, from which on the system stops to respond elastically.

$$\tan\left(\frac{\pi}{4} - \frac{\gamma}{2}\right) = \frac{\tan\left(\frac{\pi}{4}\right) - \tan\left(\frac{\gamma}{2}\right)}{1 + \tan\left(\frac{\pi}{4}\right)\tan\left(\frac{\gamma}{2}\right)} = \frac{1 - \frac{\gamma}{2}}{1 + \frac{\gamma}{2}} \quad (3.22)$$

And so

$$\gamma = \frac{2(1+\nu)\tau_{zz}}{E} = \frac{2(1+\nu)\tau}{E} \quad (3.23)$$

or

$$\gamma = \frac{\tau}{G} \quad (3.24)$$

Where  $G$  is the so-called modulus of elasticity in shear or the modulus of rigidity;

$$G = \frac{E}{2(1+\nu)} \quad (3.25)$$

If the shearing stresses only work on the sides, the distortion of the angle between any two axes only depends on shearing components parallel to these axes and we obtain in the same manner as above;

$$\gamma_{xy} = \frac{\tau_{xy}}{G} \quad \gamma_{xz} = \frac{\tau_{xz}}{G} \quad \gamma_{yz} = \frac{\tau_{yz}}{G} \quad (3.26)$$

### 3.1.4 Bulk modulus

The bulk modulus,  $B$ , is defined as

$$B = -v \frac{dp}{dv} \quad (3.27)$$

Here  $v$  is clearly the volume and  $p$  is the pressure. Or to put it otherwise<sup>5</sup>,

$$p = -B \frac{\Delta v}{v} \quad (3.28)$$

It is clear that we will use equation 3.28, as the  $\frac{\Delta v}{v}$  can easily be linked to the concept of strain. Consider for example the small rectangular of figure 3.1 again. The when a pressure  $p$  is applied to the three sides, in the elastic regime we had already derived that<sup>6</sup>

$$\begin{aligned} \gamma_{xx} &= \frac{-1}{E}(\tau_{xx} - \nu(\tau_{yy} + \tau_{zz})) \\ \gamma_{yy} &= \frac{-1}{E}(\tau_{yy} - \nu(\tau_{xx} + \tau_{zz})) \\ \gamma_{zz} &= \frac{-1}{E}(\tau_{zz} - \nu(\tau_{xx} + \tau_{yy})) \end{aligned} \quad (3.29)$$

So we obtain

---

<sup>5</sup>When the elastic approximation is valid off course

<sup>6</sup>It assumed that the volume is compressed, therefore the minus signs appear in the equations

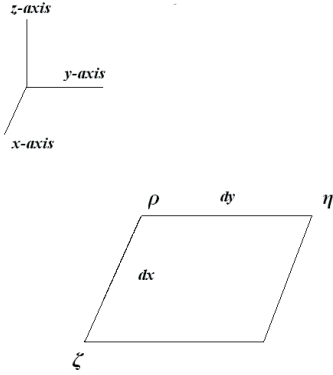


Figure 3.5: Small square element around the point  $\rho$  in the body. Once again  $dx$  and  $dy$  are parallel to the  $\hat{x}$  and  $\hat{y}$  direction respectively. The points  $\eta$  and  $\zeta$  are approximated with a first order Taylor expansion, as the element is assumed to be very small.

$$\begin{aligned}
 \frac{\Delta dx}{dx} = \gamma_{xx} &= \frac{-1}{E}(\tau_{xx} - \nu(\tau_{yy} + \tau_{zz})) = \frac{-p}{E}(1 - 2\nu) \\
 \frac{\Delta dy}{dy} = \gamma_{yy} &= \frac{-1}{E}(\tau_{yy} - \nu(\tau_{xx} + \tau_{zz})) = \frac{-p}{E}(1 - 2\nu) \\
 \frac{\Delta dz}{dz} = \gamma_{zz} &= \frac{-1}{E}(\tau_{zz} - \nu(\tau_{xx} + \tau_{yy})) = \frac{-p}{E}(1 - 2\nu) \\
 \frac{\Delta v}{v} &= \frac{\Delta dx}{dx} + \frac{\Delta dy}{dy} + \frac{\Delta dz}{dz} = -3\frac{p}{E}(1 - 2\nu) \\
 \therefore B &= \frac{E}{3(1-2\nu)}
 \end{aligned} \tag{3.30}$$

## 3.2 Elasticity in 2-dimensional cartesian coordinates

### 3.2.1 Strain in 2-dimensional cartesian coordinates

The components of strain in 2-dimensional cartesian coordinates can be found in exactly the same way as in the 3 dimensional case, therefore the end results will be stated briefly.

We now consider a very small square element (Fig.3.5). This element is basically the cubic element of figure 1, but now with  $\delta=\rho$ , i.e.  $dz=0$ , so again  $dx$  and  $dy$  are parallel to the basis vectors  $\hat{x}$  and  $\hat{y}$ . Calculating  $\zeta$  and  $\eta$  up to first order results into;

$$\phi(\vec{\zeta}) \approx \begin{bmatrix} u_1(\vec{\rho}) \\ u_2(\vec{\rho}) \end{bmatrix} + \begin{bmatrix} \frac{\partial u_1(\vec{\rho})}{\partial x} & \frac{\partial u_1(\vec{\rho})}{\partial y} \\ \frac{\partial u_2(\vec{\rho})}{\partial x} & \frac{\partial u_2(\vec{\rho})}{\partial y} \end{bmatrix} \begin{bmatrix} dx \\ 0 \end{bmatrix} \quad (3.31)$$

$$\phi(\vec{\eta}) \approx \begin{bmatrix} u_1(\vec{\rho}) \\ u_2(\vec{\rho}) \end{bmatrix} + \begin{bmatrix} \frac{\partial u_1(\vec{\rho})}{\partial x} & \frac{\partial u_1(\vec{\rho})}{\partial y} \\ \frac{\partial u_2(\vec{\rho})}{\partial x} & \frac{\partial u_2(\vec{\rho})}{\partial y} \end{bmatrix} \begin{bmatrix} 0 \\ dy \end{bmatrix} \quad (3.32)$$

Exploiting the linearity and continuity of the first order approximations one finds the deformations of  $dx$  and  $dy$

$$dx' \approx \begin{bmatrix} \frac{\partial u_1(\vec{\rho})}{\partial x} & \frac{\partial u_1(\vec{\rho})}{\partial y} \\ \frac{\partial u_2(\vec{\rho})}{\partial x} & \frac{\partial u_2(\vec{\rho})}{\partial y} \end{bmatrix} \begin{bmatrix} dx \\ 0 \end{bmatrix} \quad (3.33)$$

$$dy' \approx \begin{bmatrix} \frac{\partial u_1(\vec{\rho})}{\partial x} & \frac{\partial u_1(\vec{\rho})}{\partial y} \\ \frac{\partial u_2(\vec{\rho})}{\partial x} & \frac{\partial u_2(\vec{\rho})}{\partial y} \end{bmatrix} \begin{bmatrix} 0 \\ dy \end{bmatrix} \quad (3.34)$$

Evidently the unit elongations are;  $\gamma_{xx} = \frac{\partial u_1(\vec{\rho})}{\partial x}$  and  $\gamma_{yy} = \frac{\partial u_2(\vec{\rho})}{\partial y}$ . Additionally  $\gamma_{xy} = \gamma_{yx} = \frac{\partial u_2(\vec{\rho})}{\partial x} + \frac{\partial u_1(\vec{\rho})}{\partial y}$ , applying the same method as in 3 dimensions and the same argument based upon the symmetry of the derived equations. Again we can represent these identities in matrix-form.

$$\begin{bmatrix} \gamma_{xx} & \gamma_{xy} \\ \gamma_{yx} & \gamma_{yy} \end{bmatrix} = \begin{bmatrix} \frac{\partial u_1(\vec{\rho})}{\partial x} & \frac{\partial u_2(\vec{\rho})}{\partial x} + \frac{\partial u_1(\vec{\rho})}{\partial y} \\ \frac{\partial u_2(\vec{\rho})}{\partial x} + \frac{\partial u_1(\vec{\rho})}{\partial y} & \frac{\partial u_2(\vec{\rho})}{\partial y} \end{bmatrix} \quad (3.35)$$

### 3.2.2 Stress in 2-dimensional cartesian coordinates

Also determining the stresses is straight forward using the theory in 3 dimensions, the only difference is that one resolves the forces in 2 dimensions. Using the exact same notation as in 3 dimension one obtains 4 components

$$\begin{bmatrix} \tau_{xx} & \tau_{xy} \\ \tau_{yx} & \tau_{yy} \end{bmatrix} \quad (3.36)$$

Again in equilibrium there is no effective torque which is to say

$$\tau_{xy}dxdy = \tau_{yx}dxdy \implies \tau_{xy} = \tau_{yx} \quad (3.37)$$

So in that case we only have 3 components.

### 3.2.3 Elastic relations in 2-dimensional cartesian coordinates

The unit elongations are related to the normal stresses in exactly the same way as in 3 dimensions, with the z components set to zero. This is physically easy to comprehend. The unit elongations are the same only we have two components.

Additionally the same isotropic substance will also yield a constant ratio of stress and strain, in normal and lateral direction, in the elastic regime. Again superposition can be used in this regime providing the following identities;

$$\gamma_{xx} = \frac{1}{E}(\tau_{xx} - \nu\tau_{yy}) \quad (3.38)$$

$$\gamma_{yy} = \frac{1}{E}(\tau_{yy} - \nu\tau_{xx}) \quad (3.39)$$

$$\gamma_{xy} = \frac{1}{G}(\tau_{xy}) \quad (3.40)$$

### 3.2.4 Bulk in two dimensional cartesian coordinates

The bulk is also exact analogously to the three dimensional case,<sup>7</sup>

$$\begin{aligned} \frac{\Delta dx}{dx} &= \gamma_{xx} = \frac{-1}{E}(\tau_{xx} - \nu\tau_{yy}) = \frac{-p}{E}(1 - \nu) \\ \frac{\Delta dy}{dy} &= \gamma_{yy} = \frac{-1}{E}(\tau_{yy} - \nu\tau_{xx}) = \frac{-p}{E}(1 - \nu) \\ \frac{\Delta v}{v} &= \frac{\Delta dx}{dx} + \frac{\Delta dy}{dy} = -2\frac{p}{E}(1 - \nu) \\ \therefore B &= \frac{E}{2(1-\nu)} \end{aligned} \quad (3.41)$$

## 3.3 Elasticity in 2-dimensional polar coordinates

In our 2 dimensional experiment it is quite useful to use polar coordinates, due to the rotational symmetry about the axis of the rheometer. This means that instead of using  $\hat{x}, \hat{y}$  and  $\hat{z}$ , one uses the basis elements

$$\hat{r} = \cos(\theta)\hat{x} + \sin(\theta)\hat{y} \quad (3.42)$$

$$\hat{\theta} = -\sin(\theta)\hat{x} + \cos(\theta)\hat{y} \quad (3.43)$$

### 3.3.1 Strain in 2 dimensional polar coordinates

Once again we consider a small element but around  $\rho(r, \theta)$  now with sides parallel to the basis in polar coordinates (Fig.3.6) and a vector field  $\psi: \mathbb{R}^2 \mapsto \mathbb{R}^2$ , with components  $u_1(r, \theta), u_2(r, \theta)$ . It appears, using the formalism introduced in the preceding sections, to be easy to calculate the deformations  $dr$  and  $rd\theta$  using the Jacobian in polar coordinates

---

<sup>7</sup>still v is used to denote a two dimensional volume, i.e an area

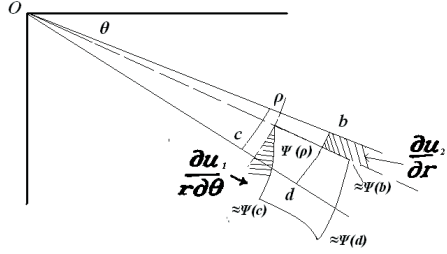


Figure 3.6: *Schematic illustration of a small element around  $\vec{\rho}$ . The lines that connect  $\vec{\rho}$  with  $b$  and  $c$  are parallel to the basis vectors,  $\hat{r}$  and  $\hat{\theta}$  at every point. Notice the rigid rotation, which is clearly  $\frac{u_2}{r}$  and the difference in arc length at the altered value of the radial component which is equal to  $\frac{u_1(\vec{\rho})}{r}$*

$$\phi(\vec{b}) \approx \begin{bmatrix} u_1(\vec{\rho}) \\ u_2(\vec{\rho}) \end{bmatrix} + \begin{bmatrix} \frac{\partial u_1(\vec{\rho})}{\partial r} & \frac{1}{r} \frac{\partial u_1(\vec{\rho})}{\partial \theta} \\ \frac{\partial u_2(\vec{\rho})}{\partial r} & \frac{1}{r} \frac{\partial u_2(\vec{\rho})}{\partial \theta} \end{bmatrix} \begin{bmatrix} dr \\ 0 \end{bmatrix} \quad (3.44)$$

$$\phi(\vec{c}) \approx \begin{bmatrix} u_1(\vec{\rho}) \\ u_2(\vec{\rho}) \end{bmatrix} + \begin{bmatrix} \frac{\partial u_1(\vec{\rho})}{\partial r} & \frac{1}{r} \frac{\partial u_1(\vec{\rho})}{\partial \theta} \\ \frac{\partial u_2(\vec{\rho})}{\partial r} & \frac{1}{r} \frac{\partial u_2(\vec{\rho})}{\partial \theta} \end{bmatrix} \begin{bmatrix} 0 \\ rd\theta \end{bmatrix} \quad (3.45)$$

Exploiting the linearity and continuity of the first order approximations one finds, presumably, the deformations of  $dr$  and  $rd\theta$ ;

$$dr' \approx \begin{bmatrix} \frac{\partial u_1(\vec{\rho})}{\partial r} & \frac{1}{r} \frac{\partial u_1(\vec{\rho})}{\partial \theta} \\ \frac{\partial u_2(\vec{\rho})}{\partial r} & \frac{1}{r} \frac{\partial u_2(\vec{\rho})}{\partial \theta} \end{bmatrix} \begin{bmatrix} dr \\ 0 \end{bmatrix} \quad (3.46)$$

$$rd\theta' \approx \begin{bmatrix} \frac{\partial u_1(\vec{\rho})}{\partial r} & \frac{1}{r} \frac{\partial u_1(\vec{\rho})}{\partial \theta} \\ \frac{\partial u_2(\vec{\rho})}{\partial r} & \frac{1}{r} \frac{\partial u_2(\vec{\rho})}{\partial \theta} \end{bmatrix} \begin{bmatrix} 0 \\ rd\theta \end{bmatrix} \quad (3.47)$$

Analogously to the theory discussed in the preceding chapters, this evidently yields the following strain components

$$\begin{bmatrix} \gamma_{rr} & \gamma_{r\theta} \\ \gamma_{\theta r} & \gamma_{\theta\theta} \end{bmatrix} = \begin{bmatrix} \frac{\partial u_1(\vec{\rho})}{\partial r} & \frac{1}{r} \frac{\partial u_1(\vec{\rho})}{\partial \theta} + \frac{\partial u_2(\vec{\rho})}{\partial r} \\ \frac{1}{r} \frac{\partial u_1(\vec{\rho})}{\partial \theta} + \frac{\partial u_2(\vec{\rho})}{\partial r} & \frac{1}{r} \frac{\partial u_2(\vec{\rho})}{\partial \theta} \end{bmatrix} \quad (3.48)$$

However one has to be careful. First of all the tangential displacement depends on the position in the  $\mathbb{R}^2$ , as  $r$  determines the factor with which this displacement increases per unit of  $\theta$ . So the translational constant,  $u_1(\vec{\rho})$  in the  $\hat{r}$  direction alters the arc-length,  $rd\theta$ , providing a unit elongation

$$\frac{r'd\theta - rd\theta}{rd\theta} = \frac{(r + u_1(\vec{\rho}))d\theta - rd\theta}{rd\theta} = \frac{u_1(\vec{\rho})}{r} \quad (3.49)$$

Additionally, the translational part in the  $\hat{\theta}$  direction adds a small angle to  $\vec{\rho}_\theta$ , i.e. an angular displacement, which is equal to<sup>8</sup>;  $\frac{u_2}{r}$ . This term is not part of the angle distortion, but of a rigid rotation, and so has to be subtracted from the initial shear components in equation 3.48. This results in the following strain components in 2 dimensional polar coordinates;

$$\begin{bmatrix} \gamma_{rr} & \gamma_{r\theta} \\ \gamma_{\theta r} & \gamma_{\theta\theta} \end{bmatrix} = \begin{bmatrix} \frac{\partial u_1(\vec{\rho})}{\partial r} & \frac{1}{r} \frac{\partial u_1(\vec{\rho})}{\partial \theta} + \frac{\partial u_2(\vec{\rho})}{\partial r} - \frac{u_2(\vec{\rho})}{r} \\ \frac{1}{r} \frac{\partial u_1(\vec{\rho})}{\partial \theta} + \frac{\partial u_2(\vec{\rho})}{\partial r} - \frac{u_2(\vec{\rho})}{r} & \frac{1}{r} \frac{\partial u_2(\vec{\rho})}{\partial \theta} + \frac{u_1(\vec{\rho})}{r} \end{bmatrix} \quad (3.50)$$

### 3.3.2 Stress in 2-dimensional polar coordinates

To find the stresses in 2 dimensional polar components we examine a small element, again with sides parallel to the basis vectors (Fig.3.7, next subsection). One can now, analogously to the formulation of stresses in the cartesian coordinate system, resolve the forces per unit of area in the direction of the basis vectors. Using the same notation as above, the result is once again rather a definition than a calculation.

$$\begin{bmatrix} \tau_{rr} & \tau_{r\theta} \\ \tau_{\theta r} & \tau_{\theta\theta} \end{bmatrix} \quad (3.51)$$

### 3.3.3 Stress-balance in 2-dimensional polar coordinates

When the material is in equilibrium, one can find explicit relations for the stresses. This subsection will derive these relations, as they are important in our quasi-static measurements. Per definition of a quasi-static measurement the material is examined in attained equilibrium positions under various circumstances.

Consider figure 3.7. The stresses on sides 1,2,3 and 4 are not equal, due to the variation of the stresses through the material. In order to keep track of different stresses, extra subscripts denoting the sides are added, e.g.  $(\tau_{rr})_1$  is the normal stress on side 1.

Now, the forces parallel to  $\hat{r}$  on sides one and three are evidently<sup>9</sup>;  $(\tau_{rr})_1(r+dr)d\theta$ ,  $-(\tau_{rrr})_3d\theta$ . The normal force on side 2 has a component along the radius of  $-(\tau_{\theta\theta})_2(r_1-r_3)\sin(\frac{d\theta}{2}) \approx -(\tau_{\theta\theta})_2(dr)\frac{d\theta}{2}$ . Likewise one verifies the corresponding component from side 4 to be approximately  $-(\tau_{\theta\theta})_4(dr)\frac{d\theta}{2}$ . The shearing forces of these sides are found in the same manner with as result  $((\tau_{r\theta})_2 - (\tau_{r\theta})_4)dr$

Summing up all the forces including a body force  $\chi$  one obtains the equation

---

<sup>8</sup>in first order as usual

<sup>9</sup>notation;  $(\tau_{rr})_1r_1 = (\tau_{rrr})_1$

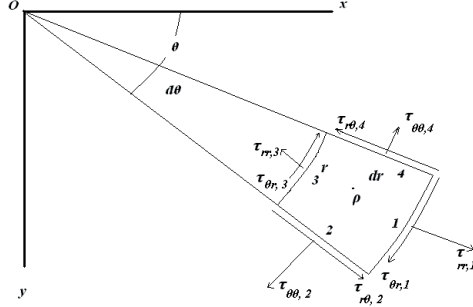


Figure 3.7: *Schematic illustration the stresses acting on an infinitesimal element around a point,  $\vec{p}$ , in polar coordinates. Again the forces per unit of length (as it is a two dimensional geometry) are resolved with respect to the basis element, i.e.  $\hat{r}$  and  $\hat{\theta}$*

of equilibrium

$$(\tau_{rr})_1(r+dr)d\theta - (\tau_{rr}r)_3d\theta - (\tau_{\theta\theta})_2(dr)\frac{d\theta}{2} - (\tau_{\theta\theta})_4(dr)\frac{d\theta}{2} + ((\tau_{r\theta})_2 - (\tau_{r\theta})_4)dr + \chi r d\theta dr \quad (3.52)$$

Dividing this term by  $dr d\theta$  yields

$$\frac{(\tau_{rr})_1(r+dr) - (\tau_{rr}r)_3}{dr} - \frac{((\tau_{\theta\theta})_2 - (\tau_{\theta\theta})_4)}{2} + \frac{((\tau_{r\theta})_2 - (\tau_{r\theta})_4)}{d\theta} + \chi r = 0 \quad (3.53)$$

Now if one takes the limit  $dr, d\theta \downarrow 0$  one gets the following expression;

$$\frac{\partial(r\tau_{rr})}{\partial r} + \tau_{\theta\theta} + \frac{\partial(\tau_{r\theta})}{\partial\theta} + r\chi = 0 \quad (3.54)$$

dividing by  $r^{10}$  yields;

$$\frac{\partial(\tau_{rr})}{\partial r} + \frac{1}{r} \frac{\partial(\tau_{r\theta})}{\partial\theta} + \frac{(\tau_{rr} - \tau_{\theta\theta})}{r} + \chi = 0 \quad (3.55)$$

A same method gives an additional equation for the equilibrium in the tangential direction

$$\frac{1}{r} \frac{\partial(\tau_{\theta\theta})}{d\theta} + \frac{\partial(\tau_{r\theta})}{\partial r} + \frac{2\tau_{r\theta}}{r} = 0 \quad (3.56)$$

---

<sup>10</sup>We assume  $r \neq 0$ , as  $r \in [r_i, r_o]$  this means the inner radius of the Taylor-Couette  $\neq 0$

### 3.3.4 Elastic relations in 2 dimensional polar coordinates

The stress strain relation stay the same under the assumption of isotropy, yielding the same equations in the  $\hat{r}, \hat{\theta}$  basis.<sup>11</sup>;

$$\gamma_{rr} = \frac{1}{E}(\tau_{rr} - \nu\tau_{\theta\theta}) \quad (3.57)$$

$$\gamma_{\theta\theta} = \frac{1}{E}(\tau_{\theta\theta} - \nu\tau_{rr}) \quad (3.58)$$

$$\gamma_{r\theta} = \frac{\tau_{r\theta}}{G} \quad (3.59)$$

### 3.3.5 Bulk modulus in two dimensional cartesian coordinates

Again it is straight forward and analogous to the three dimensional case,

$$\begin{aligned} \frac{\Delta dr}{dr} &= \gamma_{rr} = \frac{-1}{E}(\tau_{rr} - \nu\tau_{\theta\theta}) = \frac{-p}{E}(1 - \nu) \\ \frac{\Delta rd\theta}{rd\theta} &= \gamma_{\theta\theta} = \frac{-1}{E}(\tau_{\theta\theta} - \nu\tau_{rr}) = \frac{-p}{E}(1 - \nu) \\ \frac{\Delta v}{v} &= -2\frac{p}{E}(1 - \nu) \\ \therefore B &= \frac{E}{2(1-\nu)} \end{aligned} \quad (3.60)$$

## 3.4 Theory applied to our experiment

*To interpret the data, the theory described has to be applied to obtain equations. This section will derive the general equations used in analyzing the data. We will treat the material as an elastic material described in the general setting above. We assume that various little details, such as the drag force of the top plate, can be neglected due to the fact that the measurements are performed quasistatically. This allows the system to relax to its equilibrium values.*

### 3.4.1 Shear modulus

In the Taylor-Couette geometry, with inner radius  $r_i$  and outer radius  $r_o$  used in the shear experiments, equation 3.56 describes the balance of stresses in the tangential direction. Moreover in the tangential stress balance  $\frac{1}{r}\frac{(\tau_{\theta\theta})}{d\theta}$  is equal to zero and therefore equation 3.56 reduces to a simple differential equation

$$\frac{(\tau_{r\theta})}{dr} + \frac{2\tau_{r\theta}}{r} = 0 \quad (3.61)$$

---

<sup>11</sup>still in the elastic regime so that we have linear superpositions and a constant ratio between stress and strain

With solution <sup>1213</sup>

$$\tau(r, \theta) = \frac{\tau(r_i, \theta) r_i^2}{r^2} \quad r \in [r_i, r_o] \quad (3.62)$$

We use polar coordinates, consequently we know the strain components;

$$\begin{bmatrix} \gamma_{rr} & \gamma_{r\theta} \\ \gamma_{\theta r} & \gamma_{\theta\theta} \end{bmatrix} = \begin{bmatrix} \frac{\partial u_1(\vec{\rho})}{\partial r} & \frac{1}{r} \frac{\partial u_1(\vec{\rho})}{\partial \theta} + \frac{\partial u_2(\vec{\rho})}{\partial r} - \frac{u_2(\vec{\rho})}{r} \\ \frac{1}{r} \frac{\partial u_1(\vec{\rho})}{\partial \theta} + \frac{\partial u_2(\vec{\rho})}{\partial r} - \frac{u_2(\vec{\rho})}{r} & \frac{1}{r} \frac{\partial u_2(\vec{\rho})}{\partial \theta} + \frac{u_1(\vec{\rho})}{r} \end{bmatrix} \quad (3.63)$$

Due to the rotational symmetry it is obvious that equation 3.58 and  $\frac{1}{r} \frac{\partial u_2(\vec{\rho})}{\partial \theta}$  equal zero;

$$\gamma_{\theta\theta} = \frac{1}{E} (\tau_{\theta\theta} - \nu \tau_{rr}) = 0 \quad (3.64)$$

Accordingly, equation 3.50 then implies that  $u_1 = 0$ . Invoking equations 3.59 and 3.62 we get;

$$\gamma_{r\theta} = \frac{1}{G} \frac{\tau(r_i, \theta) r_i^2}{r^2} \quad r \in [r_i, r_o] \quad (3.65)$$

So we can determine  $\gamma_{r\theta}$ ,

$$\gamma_{r\theta} = \frac{\gamma_{r\theta}(r_i, \theta) r_i^2}{r^2} \quad r \in [r_i, r_o] \quad (3.66)$$

Using the rotational symmetry to conclude  $\frac{1}{r} \frac{\partial u_1(\vec{\rho})}{\partial \theta} = 0$ , equation 3.50 reduces to

$$\gamma_{r\theta} = \frac{\partial u_2(\vec{\rho})}{\partial r} - \frac{u_2(\vec{\rho})}{r} \quad (3.67)$$

But equations 3.66 and 3.67 then imply that  $u_2(r, \theta)$  is a combination of  $\frac{\alpha}{r}$  and the trivial solution, a rotation  $\beta r$ <sup>14</sup>.

Our experiment allows only no-slip solutions. Therefore the boundary conditions are fixed,;  $u_2(r_i, \theta) = r_i \theta$  and  $u_2(r_o, \theta) = 0$ . This allows us to determine  $\alpha$  and  $\beta$  and consequently solve  $u_2(r, \theta)$ <sup>15</sup> explicitly,

$$u_2(r, \theta) = \frac{-(r_0 r_i)^2 \theta}{r(r_i^2 - r_0^2)} + \frac{r(r_i^2 \theta)}{r_i^2 - r_0^2} \quad (3.68)$$

Using equation 3.67 we obtain  $\gamma_{r\theta}(r, \theta)$ ,

---

<sup>12</sup>Here the boundary condition  $\tau(r_i)$  is assumed implicitly determining the constant of integration. Moreover the subscript of the stress is dropped, as we know which stress is meant

<sup>13</sup>the torque and strain can have no  $\theta$  dependence due to the rotational symmetry

<sup>14</sup>with  $r$  in the specified domain and  $\alpha$  and  $\beta$  constants

<sup>15</sup>As usual , due to the symmetry  $u_2(r, \theta)$  can have no  $\theta$  dependence

$$\begin{aligned}\gamma_{r\theta}(r, \theta) &= \frac{\partial}{\partial r} \left( \frac{-(r_0 r_i)^2 \theta}{r(r_i^2 - r_0^2)} + \frac{r(r_i^2 \theta)}{r_i^2 - r_0^2} \right) - \frac{1}{r} \left( \frac{-(r_0 r_i)^2 \theta}{r(r_i^2 - r_0^2)} + \frac{r(r_i^2 \theta)}{r_i^2 - r_0^2} \right) \\ \gamma_{r\theta}(r, \theta) &= \frac{(r_0 r_i)^2 \theta}{r^2(r_i^2 - r_0^2)} + \frac{(r_0 r_i)^2 \theta}{r^2(r_i^2 - r_0^2)} = \frac{-2(r_0 r_i)^2 \theta}{r^2(r_o^2 - r_i^2)}\end{aligned}\tag{3.69}$$

This result is plugged into equation 3.65 to obtain

$$\frac{-2(r_0 r_i)^2 \theta}{r^2(r_o^2 - r_i^2)} = \frac{1}{G} \frac{\tau(r_i, \theta) r_i^2}{r^2} \quad r \in [r_i, r_o] \tag{3.70}$$

For  $r = r_i$  this reduces to,

$$G = \frac{r_i^2(r_o^2 - r_i^2)\tau(r_i, \theta)}{-2(r_0 r_i)^2 \theta} \quad r \in [r_i, r_o] \tag{3.71}$$

As described, we measure  $\theta$  and the torque,  $T(r, \theta)$ . This constant torque can easily be related to the stress, as the torque imposed on the wheel is equal to the torque of the sample in opposite direction(quasi-static measurement).

$$\frac{\tau(r_i, \theta) r_i^2 (2\pi r^2)}{r^2} = 2\tau(r_i, \theta) \pi r_i^2 = -T(r, \theta) \tag{3.72}$$

Exploiting the identities derived above, we can express G in the quantities obtained from the shear-experiments.

$$G = \frac{(r_o^2 - r_i^2)T(r_i, \theta)}{4\pi(r_0 r_i)^2 \theta} \quad r \in [r_i, r_o] \tag{3.73}$$

### 3.4.2 Bulk modulus

In the setup used in the bulk-measurements, a constant torque is applied on the wiper in order to compress the elastic sample and the resultant deflection angle and the initial angle of the wiper are measured. Due to the symmetry round the axis to which the wiper is attached, we will use 2 dimensional polar coordinates once again.

Examining the setup and recalling the very definition of torque ( $\vec{r} \times \vec{F}$ ), we conclude that the wiper only exerts a force in the  $\theta$ -direction. This force acts upon the plane crossing through the axis and parallel to the wiper, i.e. the plane perpendicular to the  $\theta$ -direction. Consequently, we have a normal stress in the  $\hat{r}$ -direction. The normal force of the wiper induces proportional strains,  $\gamma_{\theta\theta}$  and  $\gamma_{rr}$ , due to Hooke's law.<sup>16</sup> However the  $\gamma_{rr}$ -component in strain matrix has to be 0 as the rigid inner and outer radius prevent the material from expanding, so there must be a compressional normal stress in the  $\hat{r}$ -direction.

$$\begin{bmatrix} \tau_{rr} & \tau_{r\theta} \\ \tau_{\theta r} & \tau_{\theta\theta} \end{bmatrix} = \begin{bmatrix} \tau_{rr} & 0 \\ 0 & \tau_{\theta\theta} \end{bmatrix} \tag{3.74}$$

---

<sup>16</sup>of course we assume elastic response

Using the argument above we conclude  $u_1(r, \theta)$  is equal to zero, as there is no displacement in the  $\hat{r}$ -direction. And so  $\gamma_{rr} = 0$ , according to equation 3.58. Additionally equation 3.74 in combination with equation 3.59 assure that  $\gamma_{r\theta} = 0$ .<sup>17</sup>

We plug these results in the elastic equations and obtain <sup>18</sup>

$$\begin{aligned}\gamma_{rr} = 0 &= \frac{1}{E}(\tau_{rr} - \nu\tau_{\theta\theta}) \\ \therefore \tau_{rr} &= \nu\tau_{\theta\theta} \\ \gamma_{\theta\theta} &= \frac{1}{E}(\tau_{\theta\theta} - \nu\tau_{rr}) \\ \therefore \gamma_{\theta\theta} &= \frac{1-\nu^2}{E}(\tau_{\theta\theta})\end{aligned}\tag{3.75}$$

So we have found the following identity;

$$\frac{\tau_{\theta\theta}}{\gamma_{\theta\theta}} = \frac{E}{1-\nu^2}\tag{3.76}$$

We had already found direct expressions for the bulk modulus and shear modulus<sup>19</sup>;

$$\begin{aligned}G &= \frac{E}{2(1+\nu)} \\ B &= \frac{E}{2(1-\nu)}\end{aligned}\tag{3.77}$$

We now notice that

$$\frac{\tau_{\theta\theta}}{\gamma_{\theta\theta}} = \frac{E}{1-\nu^2} = \frac{E}{2(1+\nu)} + \frac{E}{2(1-\nu)} = G + B\tag{3.78}$$

We want to link the measured parameters,  $\theta$  and  $T(r, \theta)$  to  $\tau_{\theta\theta}$  and  $\gamma_{\theta\theta}$ . For that purpose, let us calculate the last unknown component of the strain matrix explicitly.

---

<sup>17</sup>Obviously  $G \neq 0$

<sup>18</sup>The stress  $\tau_{\theta\theta}$  is negative, i.e. compressional state. The minus sign is absorbed in value of  $\tau_{\theta\theta}$

<sup>19</sup>This is always two dimensional as the surface perpendicular does participate in creating shear

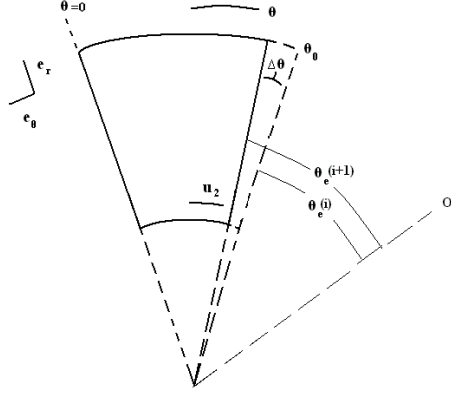


Figure 3.8: *Schematic compression of infinitesimal element of the material.*

Consider fig. 3.8, with help of this schematic illustration we conclude that

$$u_2(r, \theta) = -r\Delta\theta \frac{\theta}{\theta_0} \quad (3.79)$$

Here the factor  $\frac{\theta}{\theta_0}$  arises from the fact that the left side is fixed<sup>20</sup>. Remember that  $u_1(r, \theta) = 0$ . Using equation 3.50 we obtain

$$\gamma_{\theta\theta}(r, \theta) = \frac{1}{r} \frac{\partial -r\Delta\theta \frac{\theta}{\theta_0}}{\partial\theta} = \frac{-\Delta\theta}{\theta_0} \quad (3.80)$$

It seems that we have to be careful; the rheometer provides data in the  $O'$ -system (fig. 3.8), that is with respect to the angle the wiper was situated at the beginning of the experiment. The angles in the system of the rheometer are denoted by a prime. However we can easily express the data in our system with  $\theta = 0$  at the fixed wall;

$$\theta = O' - \theta' \quad (3.81)$$

Notice that

$$|\theta_e(i)| + |\theta_v(i)| = O'. \quad (3.82)$$

Notice that the starting angle for interval  $i$  is exactly  $\theta_e(i-1)$ . We obtain for  $\theta_0(i)$ , the starting angle during interval  $i$ ;

$$\theta_0(i) = O' - \theta_e(i-1)' = \theta_v(i-1) \quad (3.83)$$

Moreover  $\Delta\theta = \theta_e(i+1) - \theta_e(i)$  is a difference between two angles, so this quantity is the same in every system. Therefore we can determine  $\theta_0$  and  $\Delta\theta$

---

<sup>20</sup>We have a freedom of reference, i.e. angle where we choose  $\theta = 0$ , we use this freedom to chose  $\theta = 0$  at the fixed edge

directly from the data, we do not need to express angles first in our reference system. Therefore the prime of  $\theta'$  will be dropped.

The normal stress  $\tau_{\theta\theta}$  due to the action of the wiper can easily be related to the Torque,<sup>21</sup>

$$T = \int_{r_i}^{r_o} -\tau_{\theta\theta} r dr = \frac{-1}{2} \tau_{\theta\theta} (r_o^2 - r_i^2) \quad (3.84)$$

Notice the physical interpretation  $\frac{1}{2} \tau_{\theta\theta} (r_o^2 - r_i^2) = \tau_{\theta\theta} (r_o - r_i) \frac{1}{2} (r_o + r_i) = F \times \bar{r}$

Now we can relate the bulk modulus and shear modulus to the measured parameters. Suppose that the sample has attained its equilibrium value during interval  $i$ , characterized by  $\theta_v(i)$  and packing fraction  $\phi$ . Then using the identities above we can express  $\Delta T = T(i+1) - T(i)$ ,  $\theta_v(i)$  and  $\Delta\theta$  in  $B + G$ ;

$$\frac{\tau_{\theta\theta}}{\gamma_{\theta\theta}} = \frac{2\Delta T \theta_v}{\Delta\theta (r_o^2 - r_i^2)} = G + B \quad (3.85)$$

---

<sup>21</sup>of course  $T = T(r, \theta)$ , but due to the symmetry the Torque can have no  $\theta$  dependence. Additionally in this experiment the Torque is constant and is therefore denoted by  $T$

# Chapter 4

# Results

*This chapter deals with the results of the measurements. In the first section the results of the experiments concerning the shear modulus will be presented. We find that the data seems to agree reasonably well with the predictions. Subsequently the data of the bulk modulus experiment is discussed in the second section. This data is not convincing enough to make a legitimate statement about the prediction for the bulk modulus.*

## 4.1 Shear modulus

Our goal is to find the dependence of  $G$  on  $\phi$ . We determine the ratio of  $\Delta\theta$  and  $T$  from the data. This ratio can directly be related to  $B$ . The  $\phi$  of each packing fraction can subsequently be established using data analysis. The best eleven measurements are presented, these are indicated with their measurement number.

First of all, consider the measured torque  $T$  versus time  $t$  diagrams (Figure 4.1), i.e. the raw data. The graphs display exactly what we anticipated. In each one-minute interval the imposed constant deflection angle makes the system relax to a new equilibrium. Moreover the line connecting the equilibria seems to have a constant slope. In linear response the line should have a constant slope (in absolute value of course) during the whole measurement. This seems to be the case, however we shall make this more precise with help of figures 4.2 and 4.3.

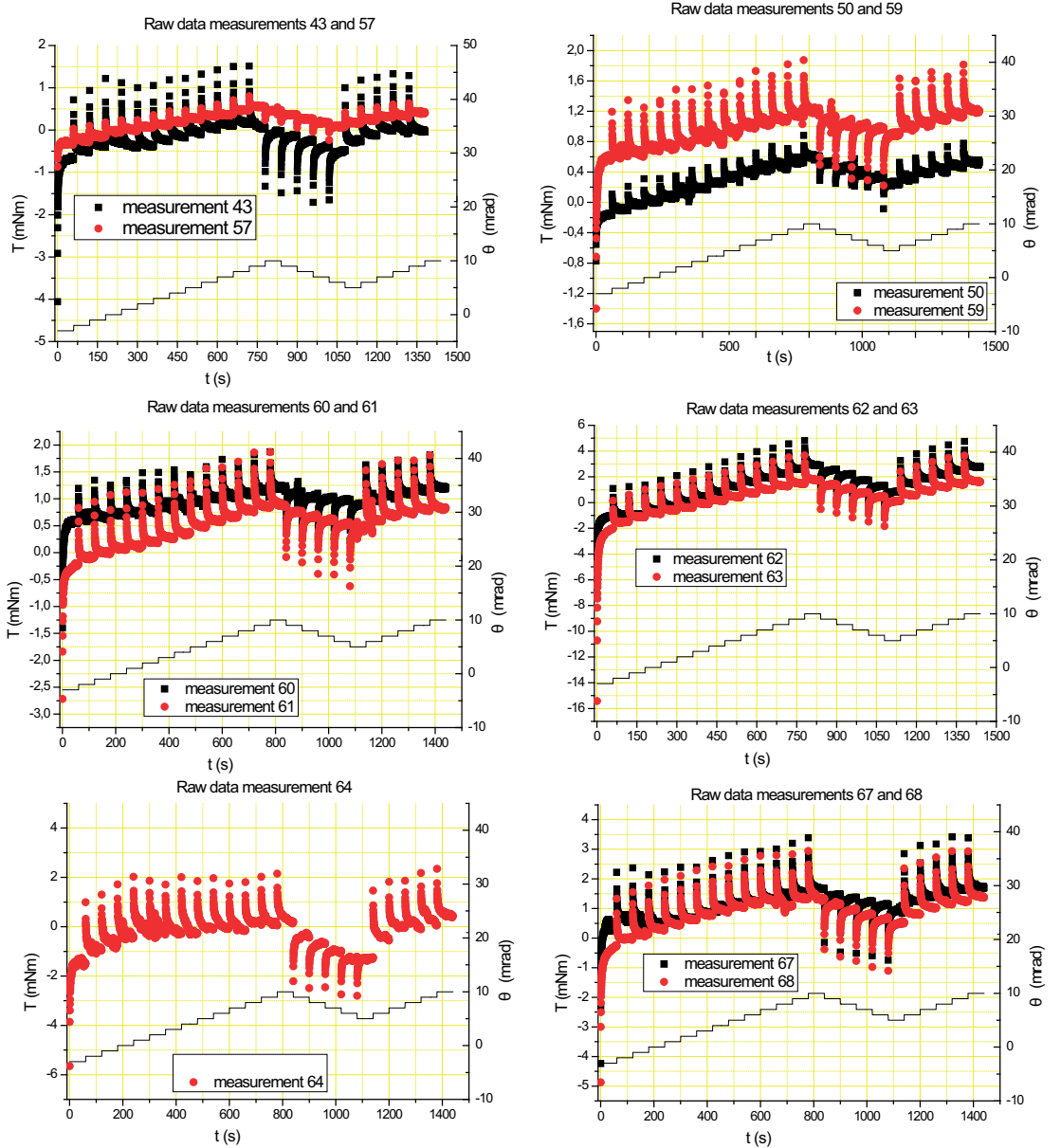


Figure 4.1: Plots of the raw data of the Torque  $T$  of the eleven best measurements. This means that the torque is plotted versus the time. We see that every interval the system relaxes to a equilibrium value. Every interval is fitted with a exponential function, motivated by the empirical results. The controlled parameter  $\Delta\theta$  is also shown. The measurements should be interpreted with respect to the axis on the left. The axis on the right represents the deflection angle.

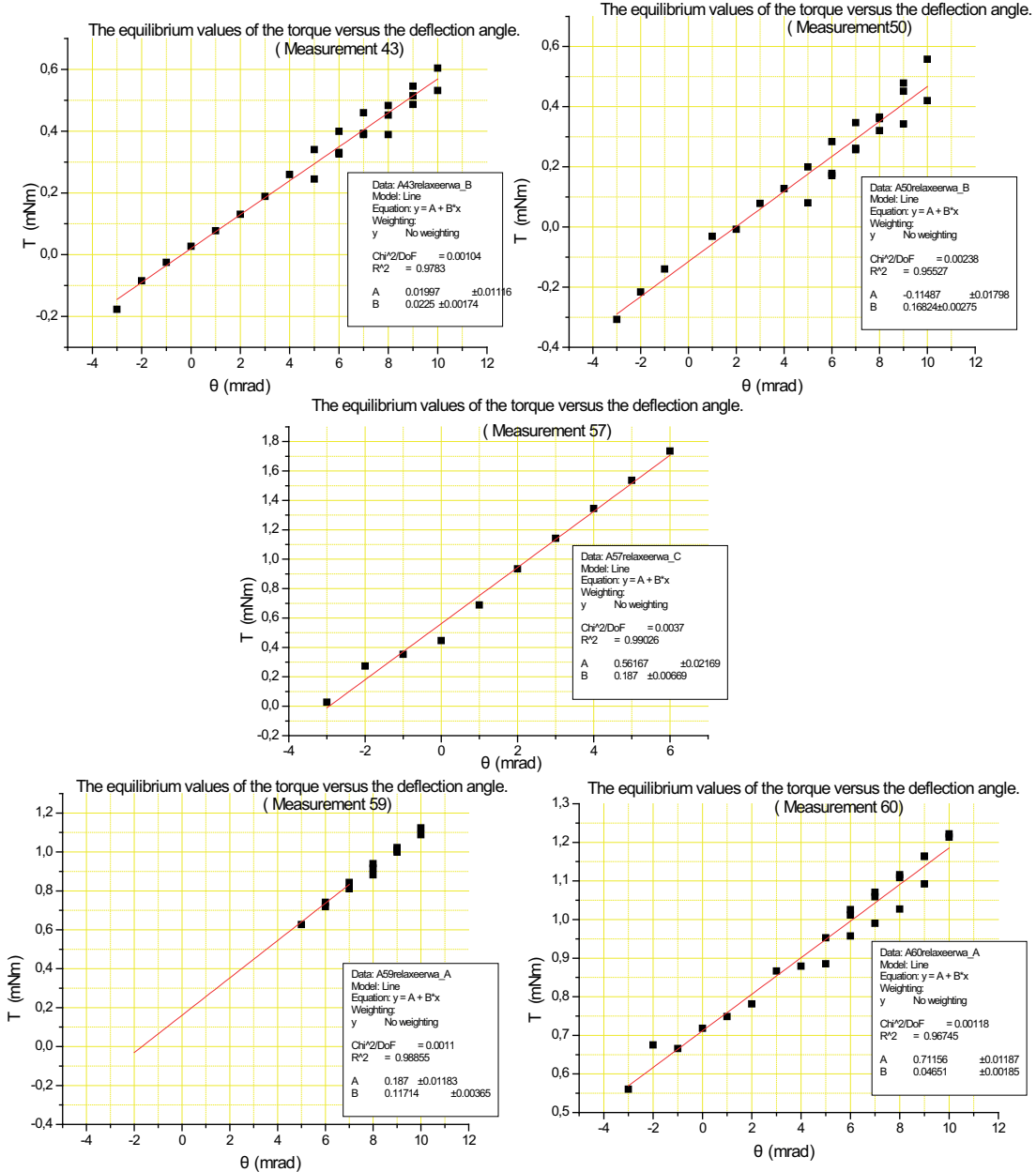


Figure 4.2: Examples of plots of the equilibrium values of the torque versus the deflection angle of each interval. In the graphs the fits and their parameters are shown. The parameters are also listed in the table below. Notice that in general the lines really represent straight lines, meaning that the ratio of torque and deflection angle is constant. This is absolutely crucial as this confirms the linear response of the system, validating our elastic model of the system. Also notice that due to the fixed parameter which ascends one millirad per interval in some regions and descends a millirad in other, we get an extra confirmation of the linearity of the system. In a linear system the absolute value of the slope should be the same in all regions of the measurement (provided that measurement stays within the elastic response region). This is obviously the case as all point lie on a straight line. This also ensures the reproducibility of the obtained equilibrium values, as we obtain the same  $T$  if  $\Delta\theta$  is the same (within experimental error).

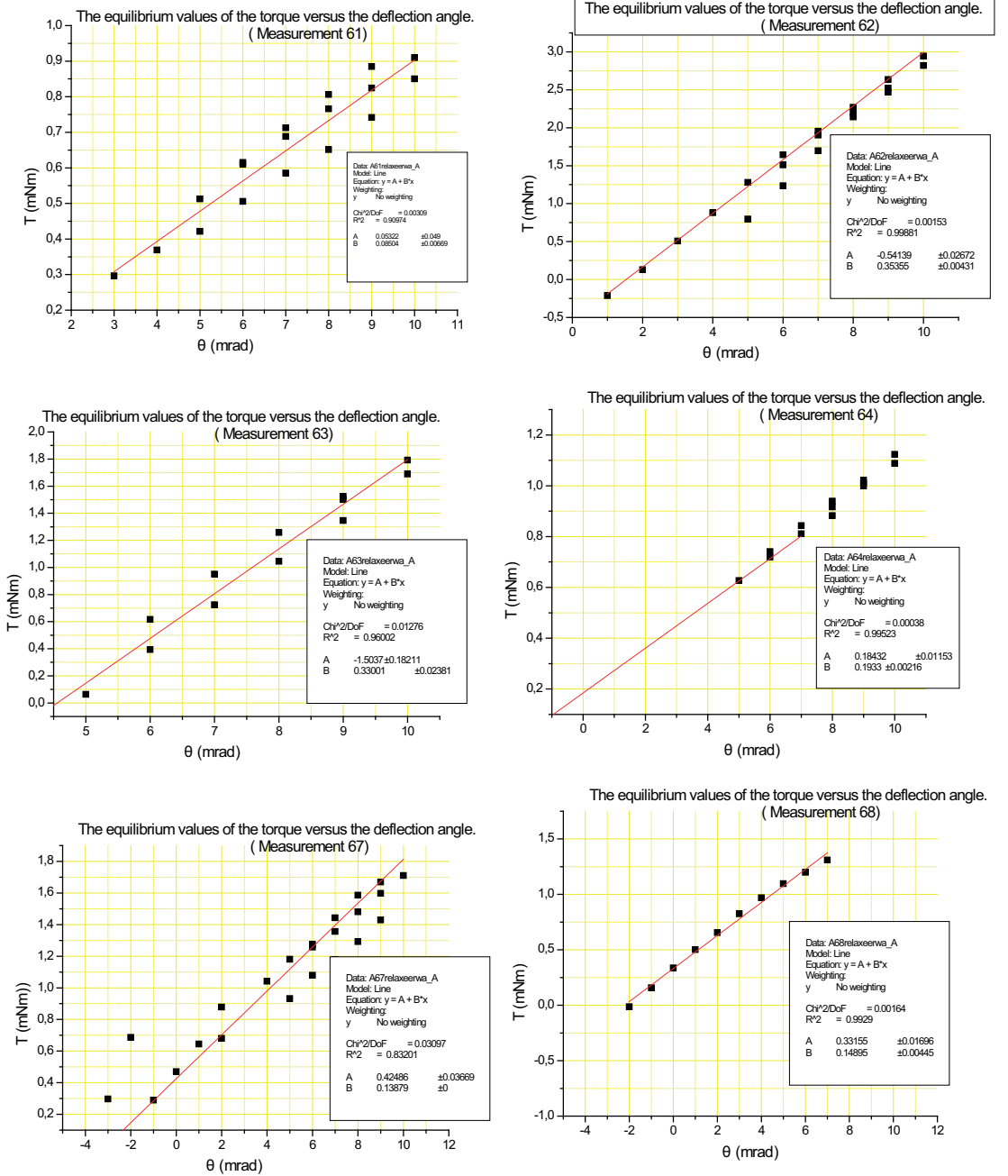


Figure 4.3: More examples of plots of the equilibrium values of the torque versus the deflection angle of each interval. In the graphs the fits and their parameters are shown. These parameters are also included in the table below. The results are similar to the graphs in the previous figure, confirming linear response at those values of  $\phi$ .

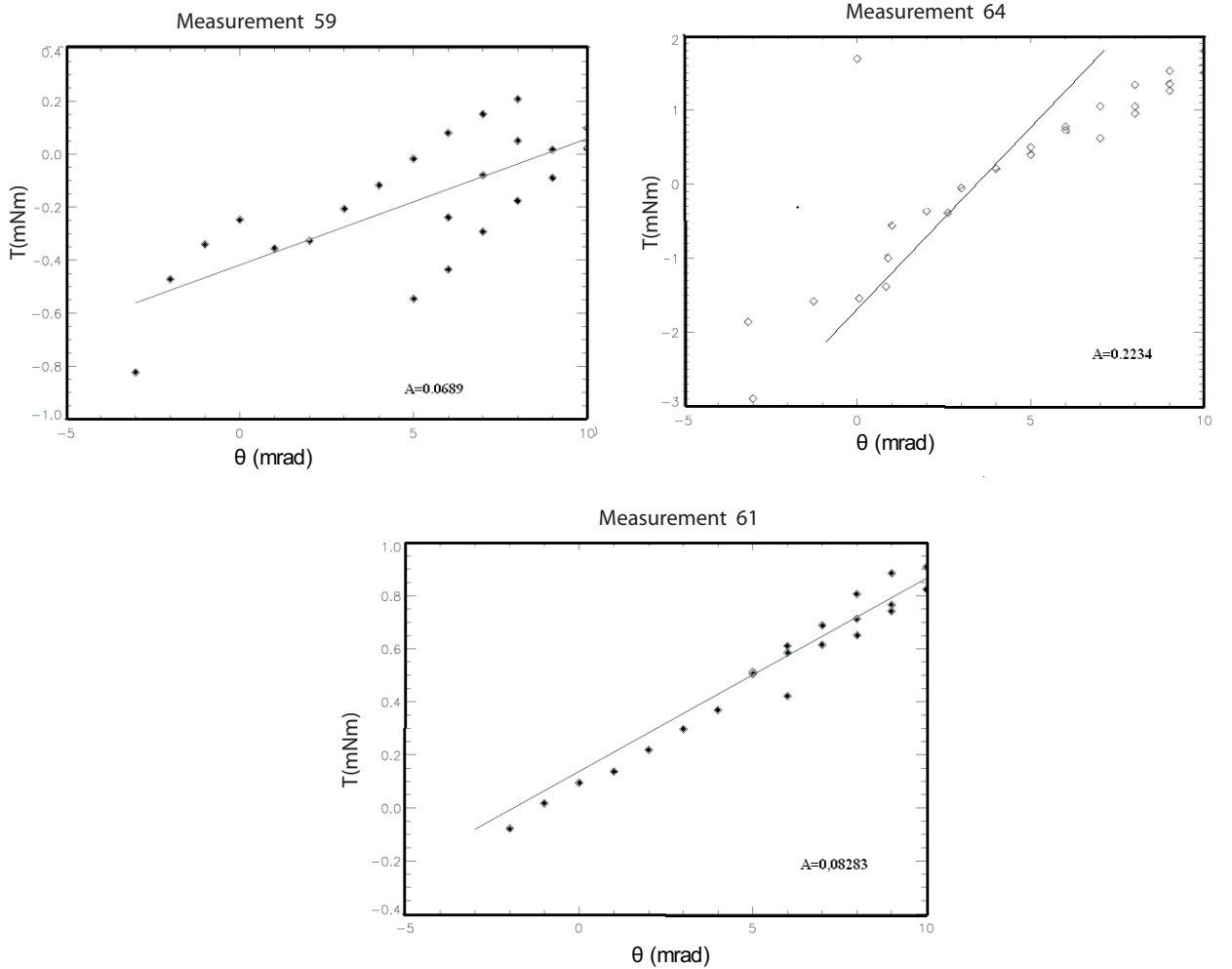


Figure 4.4: *Measurement 59 and 64 along with their idl-fit. The slope of the fitted line is denoted by the parameter  $A$ . In this program no points are omitted, thus a rearrangement has a big influence on the calculated slope of the line. Consider the graph belonging to measurement 59, clearly there is a rearrangement at the beginning of the measurement. The line fitted by the programme does not even approximate the slope. The slope can therefore only be found correctly when using the last 10 points only. For measurement 64 holds the same. Also a representative example of one of the other fits is shown. Clearly this fit is much better and gives a good impression of the slope. This is also confirmed by the fact that the fit parameters, for these measurements, obtained by the idl-program deviate only slightly from the ones obtained from origin.*

Figures 4.2 and 4.3 show the graphs of the obtained equilibrium values of each interval versus the deflection angle during that interval. Also their accompanying fits, made with help of the program *origin*, are included. Notice that these graphs indicate linear correspondence<sup>1</sup> between these parameters, confirming the linear response of the system. This is absolutely vital as this validates the elastic theory applied to the experiment. The elastic model assumes stresses and strains are proportional, yielding a constant ratio which is by definition the shear modulus. Therefore the ratio of  $T$  and  $\Delta\theta$ , which is directly proportional to the stress-strain ratio, can easily and legitimately be linked to the shear modulus with help of formula 3.73. The results are listed in table 4.1.

We also obtain these graphs with corresponding fits, directly from the *idl*-programme. The only difference is that some points showing rearrangement are deleted in the *origin* analysis. For completeness, the *idl*-plots and fits of the two measurements for which points were omitted, measurement 57 and 64, are shown in Figure 4.4. One can clearly see that the *idl*-fits can not be trusted a priori and have to be checked. The measurement points representing a rearrangement of bubbles in the system show big deviations. Consequently the fit is not accurate for the other points, which do show a linear correspondence. Therefore the points showing rearrangements should be omitted, in order to find the correct ratio of  $T$  and  $\Delta\theta$ .

For the other measurements presented the parameters obtained from the fits in *idl* and in *origin* agree within 7 percent. These are included in the table (figure 4.1), along with the packing fraction of each measurement.

---

<sup>1</sup>i.e. straight lines with a constant absolute value of the slope in all regions(ascending and descending deflection angle)

Table 4.1: *The table with the most important data. The first column denotes the number of the measurement. In the second column the radii of the inner wheels used for that measurement are listed, followed by the the column showing the packing fractions. The fourth and last column display the slope obtained with origin and idl respectively. Notice that, except for measurements 59 and 64, the slopes obtained from origin and idl seem to agree reasonably well(within 7 percent). The fifth column is obviously the most important one; it shows the calculated shear modulus. In the next column the corresponding errors of  $G$  are shown*

Measurement number	$r_i$ (meter)	$\phi$	Slope (Nm/rad)	$G$ (N/m)	Error (absolute)	Slope (Nm/rad)
43	0,025	0.954	0.225	5.8081	0.36707	0.243
50	0,025	0.931	0.16824	4.34291	0.33006	0.16653
57	0,05	0.939	0.187	4.82718	0.3379	0.1901
59	0,05	0.88	0.11714	3.02383	0.24191	0.0689
60	0,05	0.855	0.04651	1.2006	0.09605	0.04849
61	0,05	0.864	0.08504	2.1952	0.20635	0.08283
62	0,05	0.966	0.35355	9.12646	0.41982	0.35491
63	0,05	0.96	0.33001	8.51881	0.6815	0.32413
64	0,05	0.95	0.1933	4.98983	0.39919	0.223
67	0,05	0.894	0.13879	3.5827	0.28662	0.14879
68	0,05	0.9	0.14895	3.84496	0.3076	0.14893

Our main purpose finding the relation between the  $G$  and the  $\phi$  is now within our grasp<sup>2</sup>. We have to remember that we used different inner wheels (Table 4.1). Referring to equation 3.73 we see that the conversion factor used to express the ratio of  $T$  and  $\theta$  in  $G$  depends on  $r_i$ . Recalling the radius of the inner wheel we are able to calculate  $G$  for each measurement using equation 3.73. The results are included in Table 4.1. Additionally  $G$  is plotted versus  $\phi$  (Fig. 4.5).

The plot seems to suggest a well defined relation between  $G$  and  $\phi$ , except for the last three points. The points with the three highest packing fraction are clearly distinct from the rest of the set. These points are still well within the elastic response limit<sup>3</sup>, as shown in figures 4.2 and 4.3. The reason why  $G$  makes a jump at higher values of  $\phi$  is not entirely clear to us.

---

<sup>2</sup>Notice that analyzing the equilibrium values of each interval as a function of  $T$ , actually means that you interpret the quasi-static measurement as a continuous measurement. In O'hern et al it is argued that this is legitimate.

<sup>3</sup>in fact the shear modulus would make no sense outside this regime

### Dependence of the shear modulus on the packing fraction

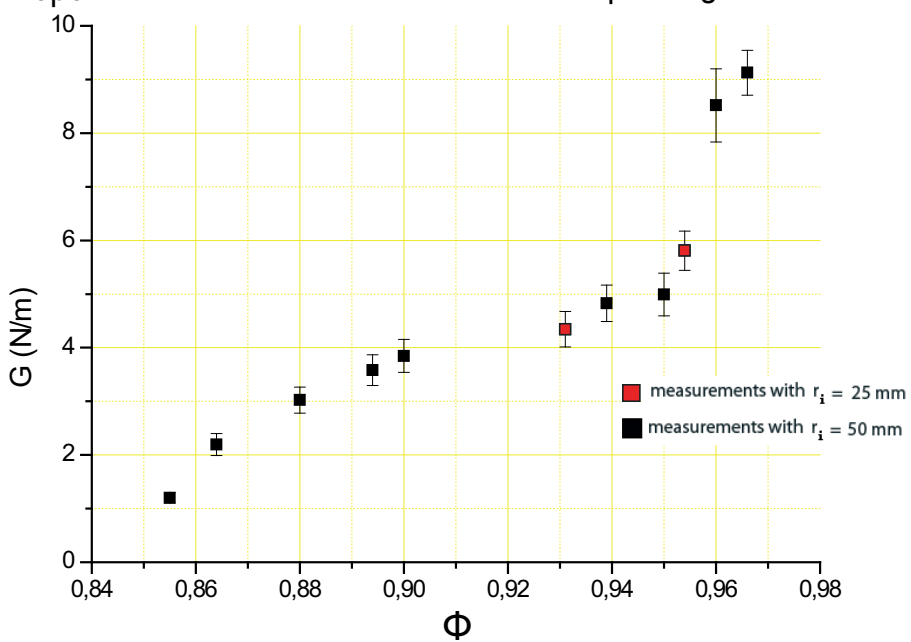


Figure 4.5: The most important graph of this section; the plot of the shear modulus versus the packing fraction. Notice that the last three points seem to make a jump. The rest of the points seem to lie on a well defined curve. This is made more precise in the following plots, where we fit those data points with a square root function, to check the predictions.

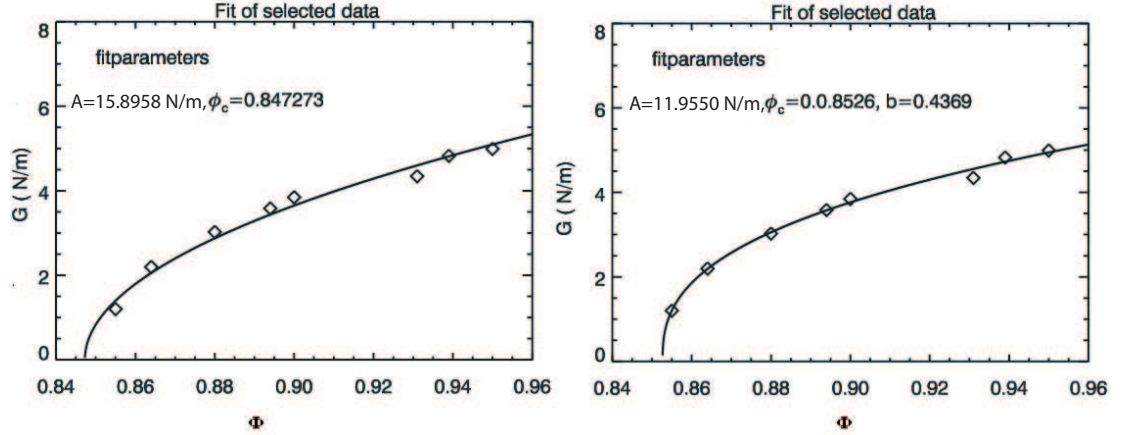


Figure 4.6: *Fits made in idl to determine the relation between the shear modulus and packing fraction( $\phi$ ) quantitatively. In the left picture the function  $A\sqrt{(\phi - \phi_c)}$  is used to fit the data. The resulting fitting parameters are shown as well. On the right the result of the fit with a general power law, i.e  $A|\phi - \phi_c|^b$ , is shown. The last three points are omitted.*

More importantly, we want to see whether the prediction agrees with our measurement. Recall that the simulations predict that the relation between the shear modulus,  $G$ , and the packing fraction looks like

$$G \sim \sqrt{\phi - \phi_c} \quad (4.1)$$

Therefore we fitted the plot of the shear modulus versus the packing fraction ( $\phi$ ) in *idl* with a simple square root function. In order to avoid a biased view, we also fitted the graph with a general power function. The results are displayed in Figures 4.6 and 4.7. The only difference between figures 4.6 and 4.7 is that in figure 4.6 the three points with the highest packing fraction are omitted, for clarity.

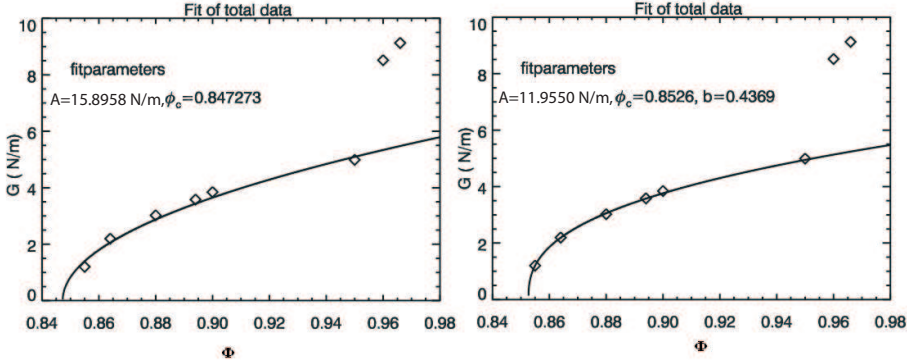


Figure 4.7: This is exactly the same illustration as the previous one, but now the last points are not omitted.

The fits shown in Figures 4.6 and 4.7 both seem to be legitimate. The best general power law, obtained with the least square estimator of the programme *idl*, has a exponent equal to 0.44. This is 14 percent off the predicted 0.5. However the fit with the square root function seems to be legitimate. Notice that the exponent of the fitted curve depends to a great extend on the values of  $G$  at packing fractions close to  $\phi_c$ . More measurements at those packing fraction, should give more convincing evidence.

The fit parameters  $\phi_c$  also seem to make sense for both fits. This parameter denotes the critical packing fraction(Jamming point). We know from standard results that this critical point occurs at a packing fraction of about 0,84. We find values of 0.847 and 0.853 for the square root fit and general power law fit,respectively.

Based on this data we may conclude that the prediction for  $G$  holds to a great extend, the fit seems very legitimate and its parameters make sense. Nevertheless more measurements at packing fractions near  $\phi_c$  are needed to definitely exclude other power laws, with exponents close to 0.5.

## 4.2 Bulk modulus

From the data of the bulk modulus experiment we want to obtain the dependence of  $B$  on  $\phi$ , by determining the ratio of  $\Delta\theta$  and  $\Delta T$  and using the results from the shear experiments. Remember that all measurements are basically identical; the packing fraction is now automatically varied every interval. We present our best 3 measurements, that are denoted by their measurement number<sup>4</sup>.

Let us first look at the raw data(Fig. 4.8), which are the plots of the measured deflection angles  $\theta$  versus time  $t$ .

The interpretation of the results is straightforward. Due to the constant torque put on the wiper the wiper compresses the material, until a new equilibrium is reached. The deflection angle of the wiper is measured. In the beginning the wiper does not touch the sample of bubbles yet. Due to the air-bearings of the rheometer the wiper can move practically frictionless until it reaches the bubbles. We can see this in the graphs. During the first interval the deflection angle of the wiper shoots up to the value, where it first touches the bubbles, so fast that we see discrete points rather than a continuous line. From that point on, the system relaxes to the new equilibrium in an exponential way, just as is the case during the other intervals.

We can also see that after a certain point the torque  $T$  is so small that the material is decompressed completely. The slope of the plot then drastically changes and goes down rapidly. Subsequently the wiper rotates until it comes to rest at a certain point, i.e. the constant line at the end of the graph.

---

<sup>4</sup>2 of the measurements presented, 71 and 72, consists of 8 intervals. The other measurement, 73, consists of 16 intervals.

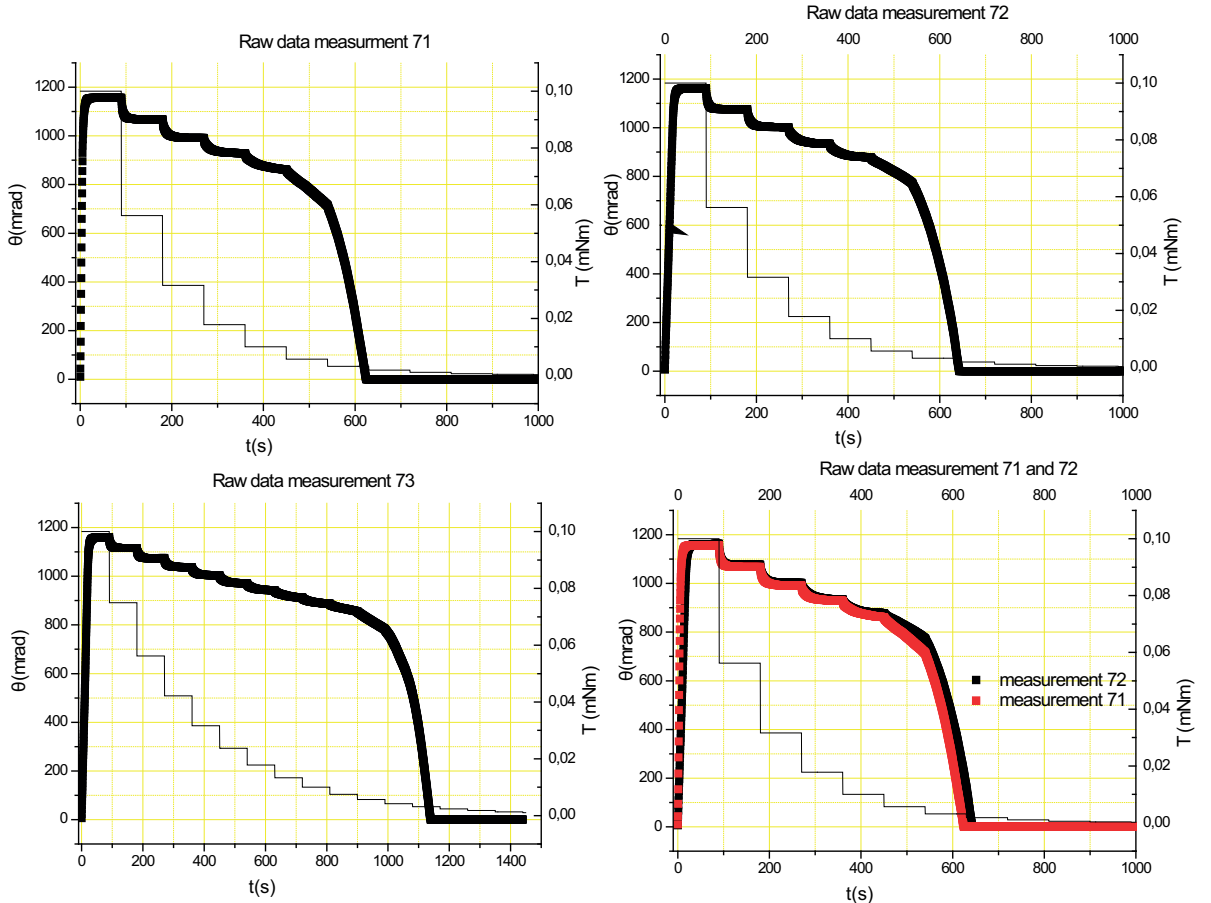


Figure 4.8: Plot of the raw data of measurements 71, 72 and 73. This means that the deflection angle  $\theta$  is plotted versus the time. We see that the measurements reproduce quite well. Notice that in the first interval we can see that the wiper first has to rotate slightly until it touches the sample of bubbles. At the end of measurement the torque is so small that the sample is completely decompressed, we see that the wiper keeps rotating until a certain value of  $\theta$  where it comes to rest. In this region the graphs suddenly goes down rapidly(at  $\approx 580$  seconds in measurements 71 and 72 and at  $\approx 900$  seconds in measurement 73). The controlled parameter  $T$  is also shown.

Table 4.2: *The table with the main results from the bulk experiment. Only the intervals for which the packing fraction can be determined are included. During the other intervals  $T$  is so small that the wiper comes completely lose. Consequently holes form in the sample making it impossible to determine  $\phi$ . Each interval is included separately in chronological order. In the first column the number of the measurement to which the interval belongs is presented, the second shows the controlled parameter. The third column displays the packing fraction. the two last column display the quantities obtained from the data, i.e the equilibrium values of the deflection angle and the angle of the compartment in equilibrium, respectively.*

Measurement number	$T$ (mNm)	$\phi$	$\theta_e(i)$ (mrad)	$\theta_v$ (mrad)
71	0.1	0.945	1157.89	973.37012
71	0.05625	0.93	1068.21	1007.92764
71	0.03162	0.91	991.559	1077.91535
71	0.01778	0.89	929.614	1157.32783
71	0.01	0.87	859.5	1211.43303
72	0.1	0.95	1181.69	925.89717
72	0.05625	0.935	1076.48	1000.24819
72	0.03162	0.92	1003.08	1073.20296
72	0.01778	0.89	933.673	1149.29931
72	0.01	0.868	877.653	1200.43746
73	0.1	0.954	1186.17	915.07613
73	0.07498	0.948	1115.99	955.91683
73	0.05625	0.94	1073.71	992.56875
73	0.04216	0.925	1037.35	1028.52253
73	0.03162	0.911	1004.03	1083.84947
73	0.02371	0.905	970.897	1091.52891
73	0.01778	0.897	942.124	1135.16215
73	0.01334	0.883	909.355	1170.4178
73	0.01	0.873	885.699	1202.70639

Using the *idl* script(**A3**) we obtain  $\theta_e(i)$ <sup>5</sup>. From the pictures we can determine  $\theta_v$  with *ImageJ*). Each interval is also characterized by a certain packing fraction reached at equilibrium. These are once again determined from the pictures of the equilibrium states, using the data analysis(**A1**). The results are presented in table 4.2

The data in table gives rise to several plots, which help to interpret the data from this table more easily. The results are given in figure 4.9.

---

<sup>5</sup>Again this means that we interpret the quasi-statical measurement as a direct measurement consisting of the equilibria points

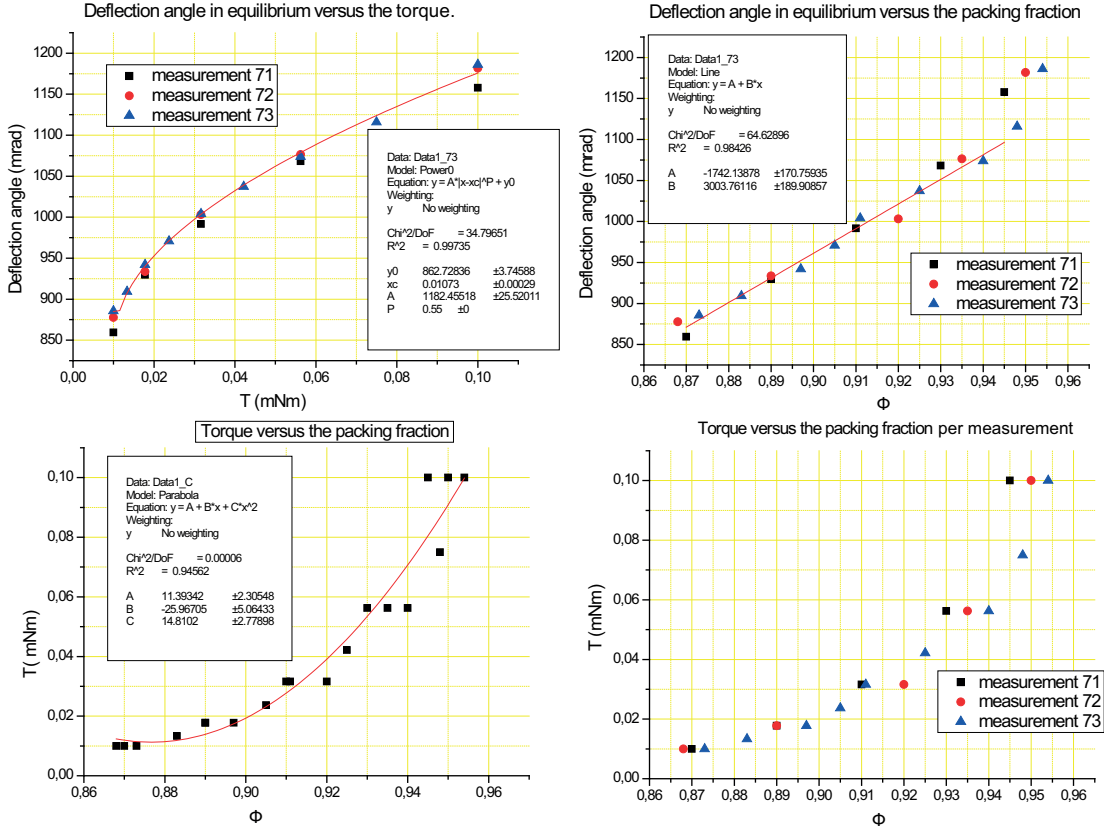


Figure 4.9: Plots of the obtained data displayed in the previous table. In the top left corner the equilibrium values of the deflection angles are plotted versus the torque  $T$ . Notice the reproducibility of the measurements. The function is fitted with the function  $y = y_0 + a|x - x_0|^p$ . On the top right hand side, the deflection angles in equilibrium, i.e.  $\theta_e(i)$ , are plotted versus the packing fraction. Notice that at low packing fractions the tail seems to be a linear. To make this precise a line is fitted through these points. The graphs on the bottoms shows the torque as function of the packing fraction, where the one on the right also shows the to which measurement the data points belong. We see a quadratic dependence. This would indicate a linear bulk modulus as the bulk modulus is the slope of this curve.

The plots in Figure 4.9 show some interesting features.

The first graph, in the top left corner, shows the plots of the equilibrium values  $\theta_e(i)$ , versus the torque of that interval . The graphs shows that our measurement reproduce. Moreover the points seem to form a power law. Therefore the function is fitted with the function  $y = y_0 + a|x - x_0|^p$ . The fitting parameters are shown in Figure 4.9. Notice that the optimal parameter for  $p$  equals 0,55.

The plot on the right shows ( $\theta_e(i)$ ) versus the packing fraction of the three measurements. We see that for the lower packing fractions the measurements reproduce reasonably well. Moreover we see a linear behavior in this region, that is why we fitted a linear function to this data. Notice the points at high packing fractions make a jump. This jump also came forward in the results in the shear experiment.

The remaining plot of Figure 4.9 shows the torque  $T$  versus the packing fraction. This plot is essential, as we already get a impression of the bulk modulus, because  $B$  is the slope of this curve. The plot seems to show a quadratic dependence, therefore we fitted these results with a quadratic polynomial. This indicates that the bulk modulus has a linear dependence on the packing fraction, while predictions from simulation suggest that  $B$  should be independent of  $\phi$ .

Table 4.3: Table with  $\theta_v$ ,  $\Delta T$ ,  $\Delta\theta$  and more importantly the obtained value of  $G + B$ , i.e. the sum of the shear and bulk modulus.

Measurement number	$\Delta T$ (mNm)	Packing fraction	$\Delta\theta$ (mrad)	$\theta_v$ mrad	Bulk+Shear modulus (N/m)
73	0.02502	0.954	70.18	915.07613	60.59914
73	0.01873	0.948	42.28	955.91683	78.66077
73	0.01409	0.94	36.36	992.56875	71.44684
73	0.01054	0.925	33.32	1028.52253	60.43447
73	0.00791	0.911	33.133	1083.84947	48.06401
73	0.00593	0.905	28.773	1091.52891	41.78689
73	0.00444	0.897	32.769	1135.16215	28.57018
73	0.00334	0.883	23.656	1170.4178	30.69597
73		0.873		1202.70639	
71	0.04375	0.945	89.68	973.37012	88.20552
71	0.02463	0.93	76.651	1007.92764	60.16047
71	0.01384	0.91	61.945	1077.91535	44.7352
71	0.00778	0.89	70.114	1157.32783	23.85429
71		0.87		1211.43303	
72	0.04375	0.95	105.21	925.89717	71.51861
72	0.02463	0.935	73.4	1000.24819	62.3464
72	0.01384	0.92	69.407	1073.20296	39.75117
72	0.00778	0.89	56.02	1149.29931	29.64865
72		0.868		1200.43746	

Using Table 4.2 we can calculate  $\Delta T = T(i+1) - T(i)$  and  $\Delta\theta$ . Additionally we can determine  $\phi$  and  $\theta_v(i)$  with image analysis. Therefore we can obtain the value of  $G + B$  for each interval using equation 3.85. The results are presented in Table 4.3.

The bulk and shear modulus as function of the packing fraction

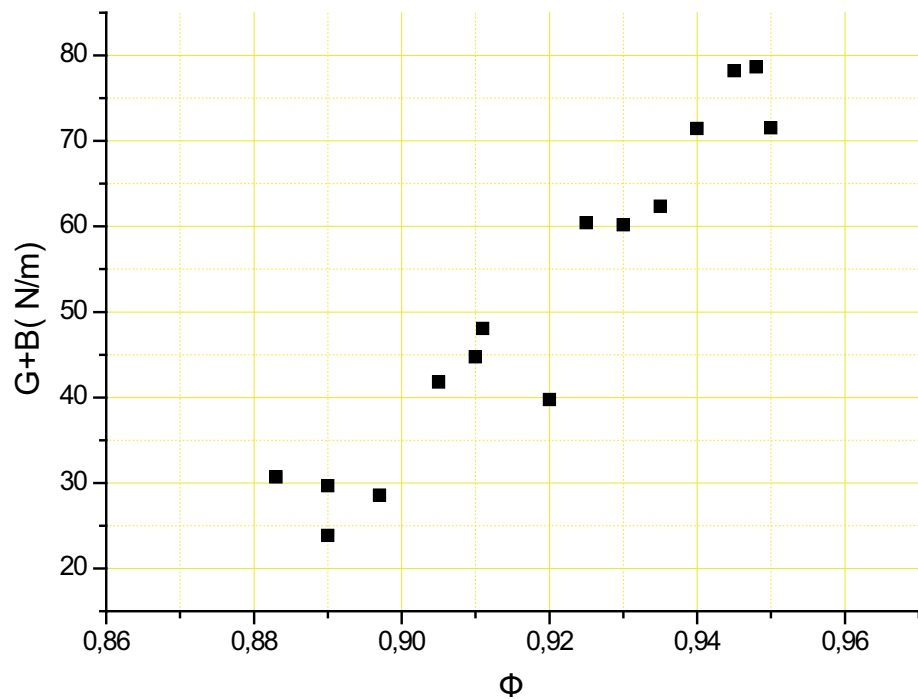


Figure 4.10: Plot of  $G+B$  as function of the packing fraction  $\phi$ . Referring to the previous section, we see that the shear modulus is much smaller ( $\approx$  factor 10). Consequently, this graph is already a strong indication of how the plot of the bulk modulus as function of the packing fraction fraction, will look like. This plot seems to show a linear curve.

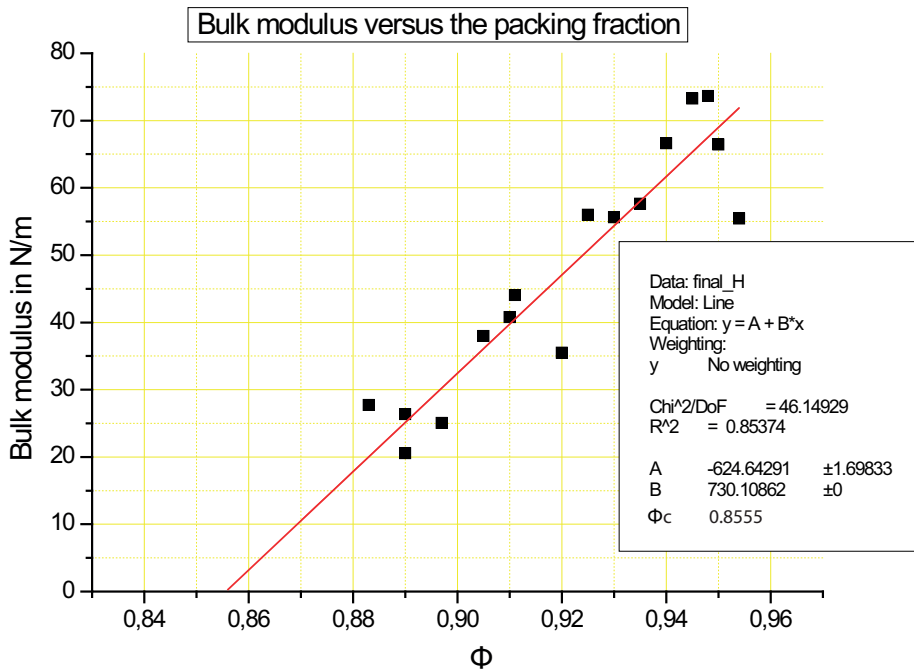


Figure 4.11: Plot of the bulk modulus  $B$  versus the packing fraction  $\phi$ . The graph seems to show a linear dependence. This is confirmed by the linear fit, which is included. The critical packing fraction  $\phi_c$ , i.e. the packing fraction for which  $B = 0$  (according to the fit), is also shown.

In order to interpret the data, we plot the sum of the bulk modulus and shear modulus as a function of  $\phi$ . the result is shown in Figure 4.10. Notice that Figure this plot already gives a strong indication of what the plot of the bulk modulus versus the packing fraction will look like; The values of  $G + B$  lie between 20 N/m and 80 N/m, referring to the previous section we find the shear modulus to be approximately a factor 10 smaller.

The plot seems to show a linear relation between the sum of the shear and bulk modulus and the packing fraction. So again the bulk modulus seems to have a linear dependence on the packing fraction.

We also can obtain the plot of the bulk modulus versus the packing fraction. We simple subtract from the results in table 4.3  $G(\phi)$ , using the fit found in the previous section. The result is shown in figure above.

Figure 4.11 shows that  $B$  has a linear dependence on  $\phi$ , exactly as we anticipated. This is made precise by the linear fit. The parameters are displayed in the plot. Extrapolating the fit we obtain the value of  $\phi$  for which  $B$  equals zero, i.e.  $\phi_c^6$ . The value (0.8555) is higher than the values of  $\phi_c$  from the fits of the previous section.

Referring to the data we see that our data does not cover the region below a packing fraction of 0.88. Below this packing fraction we are not able to measure. The main problem is due to the fact that the walls of the reservoir are made of plexiglass, which do not stay flat. Therefore the top plate cannot be leveled properly, creating a drift in the sample. This has as result that at low packing fractions we do not get a uniform sample of a low packing fraction but rather a foam with holes and regions where the packing fraction is still high. The setup will be altered in the future, i.e. made from other materials (black aluminium rather than plexiglass) to overcome this problem.

Data obtained by simulations predicts that the plot of the bulk modulus versus the packing fraction is essentially constant. From the data of the measurements above we have to conclude that  $B$  has a linear dependence on the packing fraction. However, the predictions are actually based on low packing fractions, i.e. near the Jamming point ( $\approx 0.84$ ). It could well be that around the Jamming point the bulk modulus is essentially constant and becomes linear for higher values of  $\phi$ , i.e. the region we analyzed. This could also explain the high value of  $\phi_c$  as compared to value obtained in the square root fit in the previous section. This cannot be made more quantitative using this data. Consequently we are not able to make any legitimate statement about the predictions for  $B$ .

To conclude with, consider figure 4.12. The plot shows the torque versus the packing fraction. Notice that this is the raw data, we encountered already in Figure 4.9. Measurement 72 and 73 are given an offset, equal to 0.03 and 0.06 respectively, for clarity. Remember that the slope of this graph is equal to the bulk modulus. Therefore according to the predictions the plot should show a linear correspondence at low packing fractions<sup>7</sup>. As noted above, we essentially see a quadratic dependence of  $T$  on  $\phi$  resulting in a linear correspondence between  $B$  and  $\phi$ , at higher packing fractions<sup>8</sup>. Nevertheless if the tail of the  $T$  versus  $\phi$  plot becomes linear this would indicate that the bulk modulus becomes independent of  $\phi$  at low packing fractions<sup>7</sup>. Consequently the tails of the plots are fitted with linear fits. We see that, although our data is not convincing enough to make real statements, the linear fits are qualitatively not too bad. The slopes of the fitted lines (0.389, 0.354 and 0.324 for measurements 71, 72 and 73 respectively) seems to reproduce quite well. We have to keep in mind that every quadratic function becomes approximately linear at low values. Clearly, more measurement at lower packing fractions should be done to obtain a decisive answer.

---

<sup>6</sup>If the fit also applies to the lower packing fractions

<sup>7</sup>i.e. values of  $\phi$  just above  $\phi_c$

<sup>8</sup>i.e. above  $\approx 0.89$

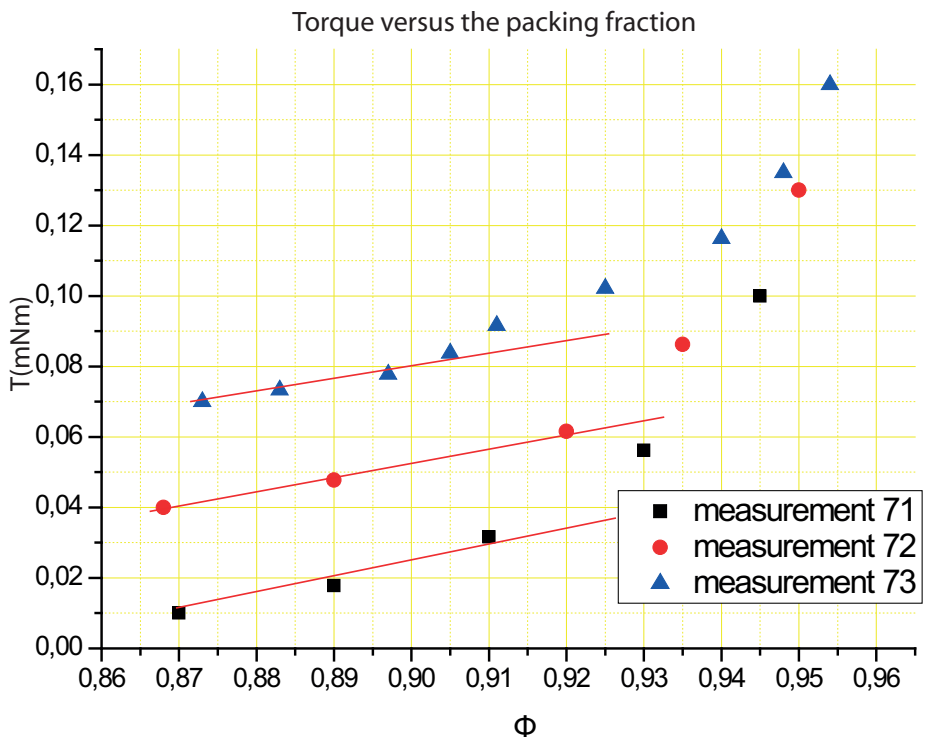


Figure 4.12: Plot of the torque versus the packing fraction per measurement. The data of measurement 72 and 73 are given an offset, equal to 0.03 N/m and 0.06 N/m respectively, for clarity. The graphs look flatter than the ones encountered previously as the axis is rescaled by a factor 1.6. The curves are fitted with linear functions. The slopes of the fitted lines equal 0.389, 0.354 and 0.32372 for measurements 71, 72 and 73 respectively.



## Chapter 5

# Frenkel-Kontorova model and sine-Gordon equation

*This chapter will deal with the physics and mathematics of systems consisting of two layers of bubbles in a Taylor-Couette geometry (fig. 5.1).*

*We will again treat these systems in the elastic limit, i.e. approximate the inter-bubble potential by a quadratic estimate. This leads to the well-known Frenkel-Kontorova model, also called the discrete sine-Gordon model. This model was first introduced by Frenkel and Kontorova in 1938, in order to describe dislocations in crystals and has become popular in many fields of physics.*

*Eventually we take the continuum limit of this discrete model to obtain the sine-Gordon equation. This equation will then be studied, in some more detail.*

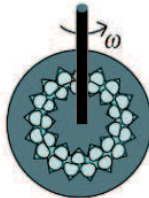


Figure 5.1: *Schematic representation of the real systems considered in this (and the subsequent) chapter. It consists of two layers of bubbles in a Taylor-Couette symmetry, providing for perfect periodic boundary conditions. The bubbles are contained between the teeth of the gear wheel, in order to be able to move the rings of bubbles past each other by rotating the inner tooth-wheel.*

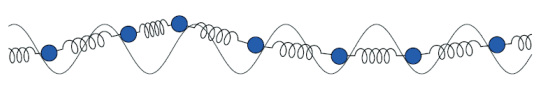


Figure 5.2: Schematic representation of the Frenkel-Kontorova model in one dimension

## 5.1 Formulation of the Frenkel-Kontorova model

We treat the rings of bubbles as chains of particles subordinated to a periodic potential (the other rings of bubbles) denoted by  $V_{sub}$ . In the Frenkel-Kontorova model the interaction potential of the particles is approximated with a harmonic potential <sup>1</sup>acting between nearest neighbors only. Consequently in our one-dimensional situation the Frenkel-Kontorova model can be visualized by a chain of particles connected by springs in a periodic potential (Fig. 5.2).

The periodic potential can be any periodic function, e.g.  $V(\vec{r}) = \cos(\vec{k} \cdot \vec{r})$ . In any case the function representing the potential is assumed to be differentiable in its arguments.

The potential energy of such a chain, consisting of  $N$  particles, can easily be calculated. Recall that the system has periodic boundary conditions;  $X_i = x_{i+jN}$ , with  $x_i$  the position of the particle,  $i \in \{0, 1, 2, \dots, N\}$  and  $j \in \mathbb{Z}$ . Using the periodic boundary conditions and the inter-bubble potential defined above we arrive at the expression for the potential energy;

$$V_{total} = \sum_{i=0}^{N-1} \frac{1}{2} k(x_{i+1} - x_i - a)^2 + \sum_{i=0}^{N-1} V_{sub}(x_i) \quad (5.1)$$

Here  $a$  is the average distance between the particles (the unstressed length of the springs) and  $k$  is the spring constant<sup>2</sup>, which is assumed to be the same between every set of neighbors.

### 5.1.1 Hamiltonian systems

When one examines the one dimensional periodic Frenkel-Kontorova model it is already clear that there is no energy dissipation. This means that that this an example of a Hamiltonian system. In this section this is examined a bit more thoroughly.

**Definition 1** A Hamiltonian system on  $\mathbb{R}^{2N}$  is system that is represented by a Hamiltonian function<sup>3</sup>. A Hamiltonian function is a function  $H(\vec{x}, \vec{p}) : \mathbb{R}^{2N} \rightarrow \mathbb{R}$ , that obeys the Hamiltonian equations;

---

<sup>1</sup>Note that is effectively a second order Taylor expansion of the interacting potential

<sup>2</sup>Which is exactly 2 times the coefficient of the second term in the Taylor expansion of the inter bubble potential.

<sup>3</sup> $x_i$  and  $p_i$  are considered as components of a vector

$$\begin{aligned}\frac{\partial}{\partial q_i} H(\vec{x}, \vec{p}) &= -\dot{p}_i \\ \frac{\partial}{\partial p_i} H(\vec{x}, \vec{p}) &= \dot{q}_i\end{aligned}\quad (5.2)$$

The classical Hamiltonian<sup>4</sup> representing the energy  $E$  is the sum of the kinetic energy  $T$  and the potential energy  $V$ ,

$$E = T + V \quad (5.3)$$

We claim that the Frenkel-Kontorova, without friction, as described in the preceding section is Hamiltonian and is represented by

$$H(\vec{x}, \vec{p}) = \sum_{i=0}^{N-1} \frac{1}{2m} p_i^2 + \sum_{i=0}^{N-1} \frac{1}{2} k(x_{i+1} - x_i - a)^2 + \sum_{i=0}^{N-1} V_{sub}(x_i) \quad (5.4)$$

Where  $p_i = m\dot{x}_i$ .

**Confirmation 1** Observe that, using the chain rule, for  $m \in \{0, 1, 2, \dots, N\}$

$$\frac{\partial \sum_{i=0}^{N-1} V_{sub}(x_i)}{\partial x_m} = \left[ \frac{\partial V_{sub}(x_1)}{\partial x_1} \quad \frac{\partial V_{sub}(x_2)}{\partial x_2} \quad \dots \quad \frac{\partial V_{sub}(x_N)}{\partial x_N} \right] \cdot \begin{bmatrix} \frac{\partial x_1}{\partial x_m} \\ \frac{\partial x_2}{\partial x_m} \\ \vdots \\ \frac{\partial x_N}{\partial x_m} \end{bmatrix} = \frac{\partial V_{sub}(x_m)}{\partial x_m} \quad (5.5)$$

We obtain using the very definition of potential energy and Newton's second law;

$$m\ddot{x}_i = F = -\frac{\partial}{\partial x_i} V_{total} = k(x_{i+1} + x_{i-1} - 2x_i) - \frac{\partial}{\partial x_i} V_{sub}(x_i) \quad (5.6)$$

Applying these identities to equation 5.4, we get

$$\begin{aligned}\frac{\partial}{\partial x_i} H(\vec{x}, \vec{p}) &= \frac{\partial}{\partial x_i} (\sum_{i=0}^{N-1} \frac{1}{2m} p_i^2 + \sum_{i=0}^{N-1} \frac{1}{2} k(x_{i+1} - x_i - a)^2 + \sum_{i=0}^{N-1} V_{sub}(x_i)) \\ So, \frac{\partial}{\partial x_i} (H(x_i, \dot{x}_i)) &= -(k(x_{i+1} + x_{i-1} - 2x_i)) - \frac{\partial}{\partial x_i} V_{sub}(x_i) = \\ -m\ddot{x}_i &= -\frac{d}{dt}(m\dot{x}_i) = -\dot{p}_i\end{aligned}\quad (5.7)$$

Confirming the second equation is as simple as the first one,

$$F = m\dot{x}_i = \frac{d}{dt}(m\dot{x}_i) = \dot{p}_i$$

$$\therefore \frac{\partial}{\partial p_i} H(\vec{x}, \vec{p}) = \frac{\partial}{\partial p_i} (\sum_{i=0}^{N-1} \frac{1}{2m} p_i^2 + \sum_{i=0}^{N-1} \frac{1}{2} k(x_{i+1} - x_i - a)^2 + \sum_{i=0}^{N-1} V_{sub}(x_i)) =$$

$$\frac{p_i}{m} = \dot{x}_i \quad (5.8)$$

---

<sup>4</sup>if it exists

What makes Hamiltonian systems so important is the fact that the Hamiltonian function is a first integral or constant of motion. That is,  $H(\vec{x}, \vec{p})$  is constant along every solution of the system. This means  $\dot{H}(\vec{x}, \vec{p}) = \frac{d}{dt}(H(\vec{x}, \vec{p})) = 0$ . Again the verification is rather a confirmation than a proof, when one uses the chain rule.

### Confirmation 2

$$\begin{aligned} \frac{d}{dt}(H(\vec{x}, \vec{p})) &= \sum_{i=0}^{N-1} \frac{\partial H(\vec{x}, \vec{p})}{\partial x_i} \dot{x}_i + \frac{\partial H(\vec{x}, \vec{p})}{\partial p_i} \dot{p}_i = \\ &\sum_{i=0}^{N-1} \frac{\partial H(\vec{x}, \vec{p})}{\partial x_i} \frac{\partial H(\vec{x}, \vec{p})}{\partial p_i} + \frac{\partial H(\vec{x}, \vec{p})}{\partial p_i} \left( -\frac{\partial H(\vec{x}, \vec{p})}{\partial x_i} \right) = 0 \end{aligned} \quad (5.9)$$

#### 5.1.2 Equation of motion

The equation of motion of the particles in the Frenkel-Kontorova model is straight forward using Newton's second law of motion<sup>5</sup>.

$$F = m\ddot{x}_i \quad (5.10)$$

$$m\ddot{x}_i = (x_{i+1} + x_{i-1} - 2x_i) - V_{sub}(x_i)'$$

When we assume the periodic potential is given by  $V(x) = 1 - V_0 \cos(yx)$ , equation 5.10 reduces to

$$m\ddot{x}_i = k(x_{i+1} + x_{i-1} - 2x_i) - yV_0 \sin(yx_i) \quad (5.11)$$

This is a Hamiltonian system. However one can include a frictional term which is, due to empirical, assumed to be proportional to time derivative of the position. Obviously such a system is not Hamiltonian anymore. Additionally one can add a constant force,  $F$  to equation 5.11. Resulting in the following expression;

$$m\ddot{x}_i + \gamma\dot{x}_i = k(x_{i+1} + x_{i-1} - 2x_i) - yV_0 \sin(yx_i) + F \quad (5.12)$$

If we now define  $\zeta_i = yx_i$  and  $\tau = \sqrt{\frac{k}{m}}t$ , then we obtain with help of the chain-rule

$$\begin{aligned} x_i &= \frac{1}{y}\zeta_i, \\ \therefore \frac{dV(x_i)}{dx} &= \frac{d}{d\zeta}(1 - V_0 \cos(\zeta_i)) \frac{d\zeta}{dx} = V_0 y \sin(\zeta_i) \end{aligned} \quad (5.13)$$

and

$$\begin{aligned} \frac{d}{dt}(x_i) &= \frac{1}{y} \frac{d\zeta_i}{d\tau} \frac{d\tau}{dt} = \sqrt{\frac{k}{my^2}} \frac{d\zeta_i}{d\tau} \equiv \sqrt{\frac{k}{my^2}} \dot{\zeta}_i, \\ \therefore \frac{d^2}{dt^2}(x_i) &= \sqrt{\frac{k}{my^2}} \frac{d\dot{\zeta}_i}{d\tau} = \sqrt{\frac{k}{my^2}} \frac{d\zeta_i}{d\tau} \frac{d\tau}{dt} \equiv \frac{k}{my} \frac{d\dot{\zeta}_i}{d\tau} = \frac{k}{my} \ddot{\zeta}_i \end{aligned} \quad (5.14)$$

---

<sup>5</sup>The dot refers to the derivative with respect to time and ' refers to the derivative with respect to position

Equation 5.12 can be simplified by rescaling the space and time coordinates as suggested above. This results in

$$\frac{k}{y} \ddot{\zeta}_i + \gamma \sqrt{\frac{k}{my^2}} \dot{\zeta}_i = \frac{k}{y} (\zeta_{i+1} + \zeta_{i-1} - 2\zeta_i) - V_0 y \sin(\zeta_i) + F \quad (5.15)$$

Multiplying this with the constant  $\frac{y}{k}$  and replacing the dummy variable  $\zeta$  with  $x$  again yields

$$\ddot{x}_i + \frac{\gamma}{\sqrt{km}} \dot{x}_i = (x_{i+1} + x_{i-1} - 2x_i) - \frac{V_0 y^2}{k} \sin(x_i) + \frac{yF}{k} \quad (5.16)$$

The periodic boundary conditions of the chain are also imposed on the periodicity of  $V_{sub}$ . If  $\chi$  is the number of periodic potentials and  $P$  the period of the potential,  $\chi \in \mathbb{N}_{<\infty}$ , then

$$x_i = x_i + p\chi \quad (5.17)$$

Here we are confronted to two cases;  $\chi = N$  and  $\chi \neq N$  the first case the system is to be known as commensurate and in the latter incommensurate. We conclude from the above discussion that, due to the periodic boundary conditions  $x_i$  is invariant under the following operations;

$$\begin{aligned} x_i &\longrightarrow x_{i+N} \\ x_i &\longrightarrow x_i + p\chi \end{aligned} \quad (5.18)$$

## 5.2 Modes in the Frenkel-Kontorova system

Stable solutions to the equation of motion, i.e.<sup>6</sup>

$$\ddot{x}_i = \eta \dot{x}_i = x_{i-1} + x_{i+1} - 2x_i + b \sin(x_i) + F \quad (5.19)$$

can be divided in two two classes;

1. Pinned modes, which are modes in which the particles have an average velocity equal to zero.
2. Sliding modes, i.e. modes in which particles have nonzero average velocity.

### 5.2.1 Pinned modes

The pinned modes, i.e. the configurations of least energy, are obvious when we examine the asymptotes of  $\kappa = \frac{V_0}{k}$ . Here  $V_0$  and  $k$  are the parameters defined in equation 5.11. When  $\kappa \rightarrow 0$  the particles will arrange at distance  $a$  no matter

---

<sup>6</sup> $\eta, b, F \in \mathbb{R}$  and unequal to zero

what the potential<sup>7</sup> is. If  $\kappa \rightarrow \infty$  the particles will all be situated at the minima of the harmonic potentials.

Let us now look at the pinned modes a bit more thoroughly and go back to equation 5.19. For pinned modes we get the following equation,

$$x_{i-1} + x_{i+1} - 2x_i + b \sin(x_i) + F = 0 \quad (5.20)$$

As in equilibrium the harmonic interaction averages to zero over the whole chain we see that pinned solutions can only exist whenever  $b \sin(x_i) + F$  has zeros,<sup>8</sup> i.e.  $F < b$ . In the commensurate case the minimal solution is of course the one in which the particles are placed in the minima of the effective potential  $b \cos(x) - FX$ , so

$$x_i = -\pi + \arcsin\left(\frac{F}{b}\right) + 2\pi i \quad (5.21)$$

### 5.2.2 Sliding solutions

Let us define the velocity of the center of mass.

$$v_{cm} = \frac{1}{N} \sum_{j=1}^N x_j \dot{x}_j(t) \quad (5.22)$$

Additionally we define the time average of the preceding equation as

$$\bar{v} = \lim_{T \rightarrow \infty} \frac{1}{T} \int_0^T \sum_{j=1}^N x_j \dot{x}_j(t) dt \quad (5.23)$$

#### Solid sliding

The solid sliding mode is the mode in which all particles move as rigid object and do not move with respect to each other<sup>9</sup>, i.e.

$$x_i(t) = x_1(t) + 2\pi(i-1) \quad (5.24)$$

Consequently we can see the system in the equivalent case of one particle moving through a effective potential  $b \cos(x) - Fx$ ;

$$\ddot{x} + \eta \dot{x} = b \sin(x) + F \quad (5.25)$$

This nonlinear equation cannot be solved analytically. However in the limit  $b = 0$  we can see that the solution attains a constant velocity,  $x_1(t) = \frac{F}{\eta} t$ . Additionally if  $F \gg \eta^2$  we may consider  $\lim_{\eta \rightarrow 0}$ . We find that there is a critical force ( $F_c$ ), i.e. a value of  $F$  such that for lower values sliding solutions are not possible anymore, and a corresponding value for  $b$  ( $b_c$ ). We can use conservation of energy, as we eliminated the dissipative, to calculate the values explicitly. We get

---

<sup>7</sup> $V_0$  is of course assumed to be finite and constant

<sup>8</sup>Notice that these are exactly the minima of the Energy

<sup>9</sup>Notice that this is the sliding case of  $\kappa \rightarrow 0$

$$\frac{\dot{x}^2}{2} = b \cos(x) = E = \frac{v_0^2}{2} + b \quad (5.26)$$

where  $v_0$  is the velocity with which the particles at the maxima of the external potential. Solving the previous equation for  $v_0$  we obtain

$$x(t) = \sqrt{v_0^2 + 2b(1 - \cos(x))} \quad (5.27)$$

At the critical value,  $v_0 \rightarrow 0$  so in that case equation 5.27 reduces to <sup>10</sup>

$$x(t) = \sqrt{v_0^2 + 2b(1 - \cos(x))} = 2\sqrt{b}c \sin\left(\frac{x}{2}\right) \quad (5.28)$$

We determine the energy loss due to friction and the energy gain due to the driving during one period. As the system is Hamiltonian, in this limit, these contributions should be equal

$$\begin{aligned} U_\eta &= \int_0^T \eta v v dt = \int_0^{2\pi} \eta v dx \\ &= 2\eta\sqrt{b} \int_0^{2\pi} \sin\left(\frac{x}{2}\right) dx = 8\eta\sqrt{b} \end{aligned} \quad (5.29)$$

$$U_F = \int_0^{2\pi} F dx = 2\pi F \quad (5.30)$$

Resulting in

$$b_c = \frac{\pi^2}{16} \left(\frac{F}{\eta}\right)^2 \quad (5.31)$$

Assuming that  $\eta$  and  $F$  are of the same order, i.e. examining the system at about constant speed, we obtain  $F \gg \eta^2$  for  $\eta \rightarrow 0$ . Because the ratio  $\frac{F}{\eta}$  is constant. This makes sense qualitatively as in this region the driving force should be much bigger than the frictional term. This equation also makes that quantitative.

### Uniform sliding

Uniform sliding is far more complicated than pinned or solid slide solutions. These sliding modes are characterized by different particle densities each having its own sliding average velocity. In uniform sliding the particles all perform the same motion, but at different times,

$$x_i(t) = ai + vt + f(ai + vt) \quad (5.32)$$

Here  $a$  is once again the average inter particle distance and  $v$  is the average sliding velocity, defined above. When we substitute this equation in the equation of motion, we can describe  $f$ . Using the translational symmetry we know that  $f$  should be periodic and should have a period of  $2\pi$ . If we look at the distance between two neighboring particles at time  $t$ ,

---

<sup>10</sup>In lowest order of  $F$  and  $\eta$

$$x_{i+1} - x_i = a + f(ai + a + vt) - f(ai + vt) \quad (5.33)$$

we note that when  $a = 2\pi$  the particles do not move with respect to each other. Solid sliding is therefore just a special case of uniform sliding, with  $a = 2\pi$ . Solving the equation for uniform sliding is rather difficult in the discrete case, and can be obtained using simulations. One can make the problem easier by taking the continuum limit. And so approximate a discrete system by a continuum one. However it is up to the specific problem whether such an approximation makes sense.

### 5.3 The sine-Gordon equation

The Frenkel-Kontorova model describes a chain of a certain amount of particles with specified masses in the elastic limit, resulting in equation 5.11 as the equation of motion of the system. One can take the continuum limit of this equation by keeping the size of the system constant while letting the particle number  $N$  go to infinity, i.e. making the distance between the particles to zero. This basically means that we treat the discrete values  $x_i$  as function values of a continuous parameter  $x$ , i.e.  $x_i = x(ia)$ , and subsequently let  $N$  and  $a$  go to infinity and zero, respectively.

Let us consider the Frenkel-Kontorova without friction and external force. Equation 5.16 then reduces to

$$\begin{aligned} \ddot{x}_i &= (x_{i+1} + x_{i-1} - 2x_i) - \frac{V_0 y^2}{k} \sin(x_i) \\ \ddot{x}_i + (x_{i+1} - x_{i-1} - 2x_i) + \frac{V_0 y^2}{k} \sin(x_i) &= 0 \end{aligned} \quad (5.34)$$

Notice that  $(x_{i+1} + x_{i-1} - 2x_i)$  is the discrete Laplacian. This becomes the ordinary continuous Laplacian when  $a = x_{i+1} - x_i \rightarrow 0$ . In order to avoid confusional notation,  $\phi$  will be used to denote the function depending on the position  $x$  and time  $t$ . With these considerations in mind it is clear that equation 5.34 reduces, in the continuum limit, to

$$\frac{\partial^2 \phi(x, t)}{\partial t^2} - c \frac{\partial^2 \phi(x, t)}{\partial x^2} + a \sin(\phi(x, t)) = 0 \quad (5.35)$$

Where  $a$  and  $c$  are constants, assumed to be equal to one<sup>11</sup>. Additionally we will use the shorthand notation to denote the partial derivatives, so that equation 5.35 reduces to

$$\phi(x, t)_{tt} - \phi(x, t)_{xx} + \sin(\phi(x, t)) = 0 \quad (5.36)$$

---

<sup>11</sup>This can be done by simply rescaling the variables. However it should be pointed out that when examining real physical problems the constants are of great importance as they will also appear in the Lagrangian and Hamiltonian. For example  $c$  should then be set to a mass, also the speed of light will appear.

The equation above is known as the sine-Gordon equation. Note that in absence of the  $\sin(\phi(x, t))$ -term, equation 5.35 reduces to the Helmholtz-equation. This equation has well-known wave solutions, i.e.  $\phi(x, t) = \mu f(x - ct) + \nu g(x + ct)$ . Where  $\mu, \nu$  are constant determined by the boundary conditions and  $f$  and  $g$  are at least  $C^2$  with respect to  $t$  and  $x$ .

### 5.3.1 Transformation of the sine-Gordon equation

As noted before the sine-Gordon equation looks like the Helmholtz-equation. This can be used to transform the equation. The transformations stated beneath will be used frequently as we expect traveling wave solutions.

Let

$$\xi = \frac{1}{2}(x - t) \quad (5.37)$$

and

$$\eta = \frac{1}{2}(x + t) \quad (5.38)$$

Then, by the chain rule,

$$\frac{\partial}{\partial x} = \frac{\partial \xi}{\partial x} \frac{\partial}{\partial \xi} + \frac{\partial \eta}{\partial x} \frac{\partial}{\partial \eta} = \frac{1}{2} \left( \frac{\partial}{\partial \xi} + \frac{\partial}{\partial \eta} \right) \quad (5.39)$$

$$\frac{\partial}{\partial t} = \frac{\partial \xi}{\partial t} \frac{\partial}{\partial \xi} + \frac{\partial \eta}{\partial t} \frac{\partial}{\partial \eta} = \frac{1}{2} \left( \frac{\partial}{\partial \eta} - \frac{\partial}{\partial \xi} \right). \quad (5.40)$$

This gives,

$$\frac{\partial^2 \phi(x, t)}{\partial x^2} = \frac{1}{4} \left( \frac{\partial}{\partial \xi} + \frac{\partial}{\partial \eta} \right) \left( \frac{\partial \phi(\xi, \eta)}{\partial \xi} + \frac{\partial \phi(\xi, \eta)}{\partial \eta} \right) = \frac{1}{4} \left( \frac{\partial^2 \phi(\xi, \eta)}{\partial \xi^2} + 2 \frac{\partial^2 \phi(\xi, \eta)}{\partial \xi \partial \eta} + \frac{\partial^2 \phi(\xi, \eta)}{\partial \eta^2} \right) \quad (5.41)$$

$$\frac{\partial^2 \phi(\xi, \eta)}{\partial t^2} = \frac{1}{4} \left( \frac{\partial}{\partial \eta} - \frac{\partial}{\partial \xi} \right) \left( \frac{\partial \phi(\xi, \eta)}{\partial \eta} - \frac{\partial \phi(\xi, \eta)}{\partial \xi} \right) = \frac{1}{4} \left( \frac{\partial^2 \phi(x, t)}{\partial \xi^2} - 2 \frac{\partial^2 \phi(\xi, \eta)}{\partial \xi \partial \eta} + \frac{\partial^2 \phi(\xi, \eta)}{\partial \eta^2} \right). \quad (5.42)$$

Plugging these result into equation 5.35, we get<sup>12</sup>

$$\phi(\xi, \eta)_{\eta\xi} = \sin(\phi(\xi, \eta)) \quad (5.43)$$

This was the original form in which the equation was considered in the course of investigation of surfaces of constant Gaussian curvature  $K = -1$ , also called pseudospherical surfaces. Gaussian curvature is an intrinsic measure of curvature, i.e. its value depends only on how distances are measured on the surface, not on the way it is embedded in space. In this thesis this aspect will not be discussed, besides this notification.

---

<sup>12</sup>From now on the notation  $f_x$  is used to denote the partial derivative to  $x$

### 5.3.2 Soliton en breather solutions

The sine-Gordon equation cannot be solved in all generality. However by making the right ansatz several classes of solutions can be found. It is obvious that the solution  $\phi(x, T)$  should not change<sup>13</sup> when the time and space variables are interchanged, due to the symmetry of the sine-Gordon equation. Observe that

$$\begin{aligned}\arctan(\theta) &= -\frac{1}{2}\pi - \arctan\left(\frac{1}{\theta}\right) & \text{for } \theta < 0 \\ \arctan(\theta) &= \frac{1}{2}\pi - \arctan\left(\frac{1}{\theta}\right) & \text{for } \theta > 0\end{aligned}\quad (5.44)$$

This means that interchanging space and time variables preserves the solution. Therefore we make the ansatz,

$$\phi(x, t) = 4 \arctan\left(\frac{\chi(x)}{\psi(t)}\right) \quad (5.45)$$

Plugging the ansatz into the sine-Gordon equation we obtain

$$\frac{\psi^2}{\chi} \chi_{xx} + \frac{\chi^2}{\psi} \psi_{tt} = (\psi^2 + 2\psi_t^2 - \psi\psi_{tt}) + (-\chi^2 + 2\chi_x^2 - \chi\chi_{xx}) \quad (5.46)$$

The right-hand side contains two terms, one depends only on  $t$  and the other only on  $x$ , so it can be eliminated by differentiating the equation with respect to  $t$  and  $x$ . Doing this and dividing the result by  $-2\psi\psi_t\chi\chi_x$  results into

$$\left(\frac{\chi_{xxx}}{\chi^2\chi_x} - \frac{\chi_{xx}}{\chi^3}\right) + \left(\frac{\psi_{ttt}}{\psi^2\psi_t} - \frac{\psi_{tt}}{\psi^3}\right) = 0, \quad (5.47)$$

Or equivalently,

$$\frac{(\frac{\chi_{xx}}{\chi})_x}{\chi\chi_x} + \frac{(\frac{\psi_{tt}}{\psi})_t}{\psi\psi_t} = 0. \quad (5.48)$$

Notice that the left term only depends on  $x$ , whereas the right one only depends on  $t$ . Therefore we can rewrite the equation

$$\frac{(\frac{\chi_{xx}}{\chi_x})_x}{\chi\chi_x} = -\frac{(\frac{\psi_{tt}}{\psi_t})_t}{\psi\psi_t} = -6v^2 \quad (5.49)$$

Here  $v \in R$  is a separation constant, which is assumed to be positive. Separating the two equations then gives

$$\begin{aligned}\frac{d}{dx}\left(\frac{\chi_{xx}}{\chi_x}\right) &= -6v^2\chi\chi_x \\ \frac{d}{dt}\left(\frac{\psi_{tt}}{\psi_t}\right) &= -6v^2\psi\psi_t\end{aligned}\quad (5.50)$$

These can be integrated directly to give

---

<sup>13</sup>That is, change more than by some constant

$$\begin{aligned}\frac{\chi_{xx}}{\chi} &= -3v^2\chi^2 + m \\ \frac{\psi_{tt}}{\psi} &= 3v^2\psi^2 + \sqrt{(m^2 - 1)}\end{aligned}\quad (5.51)$$

Here  $m$  and  $\sqrt{(m^2 - 1)}$  are constants of integration which are connected through equation 5.45. When we clear the denominators we find the final form

$$\begin{aligned}\chi_{xx} &= -3v^2\chi^3 + m\chi \\ \psi_{tt} &= 3v^2\psi^3 + \sqrt{(m^2 - 1)}\psi\end{aligned}\quad (5.52)$$

**Definition 2** A soliton is a stable isolated (i.e., solitary) traveling nonlinear wave solution to a set of equations that obeys a superposition principle and so have the following properties;

1. They are of permanent form
2. They are localized within a region
3. They can interact with other solitons, and emerge from the collision unchanged, except for a phase shift.

The sine-Gordon equation has various soliton solutions. The most simple one is a single-soliton solution, that can be found considering equation 5.52 with  $v = 0$  under the condition that  $\chi_{xx} = \chi_x$  and  $\psi_{xx} = \psi_x$ . The solutions of  $\chi$  and  $\psi$  are then straightforward.

$$\begin{aligned}\chi(x) &= \exp(mx) \\ \psi(t) &= \exp(\sqrt{(m^2 - 1)}t)\end{aligned}\quad (5.53)$$

plugging this into equation 5.45 we obtain

$$\begin{aligned}\phi(x, t) &= 4 \arctan\left(\exp\left(m\left(x - \frac{\sqrt{(m^2 - 1)}}{m}t\right)\right)\right) = \\ \phi(x, t) &= 4 \arctan\left(\exp\left(\frac{x - \beta t}{\sqrt{(1 - \beta^2)}}\right)\right) \\ \beta &= \frac{m^2 - 1}{m}\end{aligned}\quad (5.54)$$

We immediately see that this solution has a lorentz contraction, showing the relativistic invariance of the sine-Gordon equation. In the next section this single soliton will be derived in an alternative way, examining the lorenz invariance more thoroughly.

Notice that the integration constant can be negative. We then get the same solution, only with  $-x$  instead of  $x$ . The positive solution is known as the kink solution, while the negative solution is a so-called anti-kink solution.

We can illustrate what a kink-soliton represents by looking at a pinned commensurate situation. Consider the chain in its trivial ground state, i.e. all

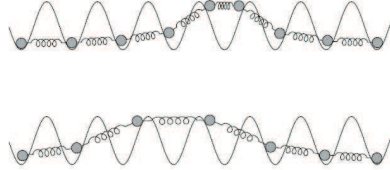


Figure 5.3: *A schematic illustration to get an idea of what a kink and antikink solution represent physically is shown.*

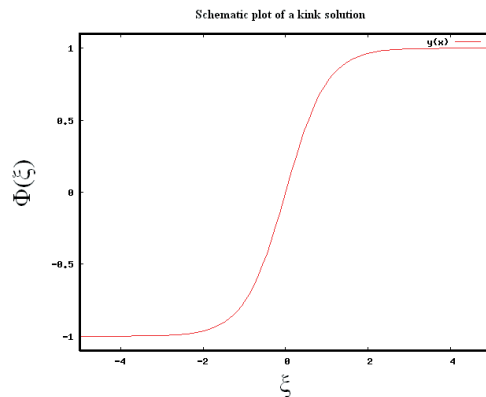


Figure 5.4: *Schematic plot of the kink solution.*

the particles at the bottoms of the potential wells. Now move a group consisting of  $g \in 0, 1 \dots N$  particles one well to the right. Consequently there is a well that contains no particles and, about  $ga^{14}$  to the right, a well that contains two particles (provided that the potential barrier is high enough to prevent the system going back to its trivial ground state). One now speaks of a kink at the site of the empty well and an antikink at the site of the doubly occupied well. In figure 5.3 this is illustrated and one sees that a kink (or antikink) has a certain width, because particles in wells nearby are pulled towards the kink and away from the antikink. Because of this effect, only a very small force is needed to make the kink move one well. In the continuum case we can represent this analogously in terms of densities,i.e a wave of a lower respectively higher density travels through the continuum.

A two-soliton solution can be found in a similar way by considering 5.52 with  $v = 0$  and  $m > 1$ ;

---

<sup>14</sup>were a denotes the average particle distance.

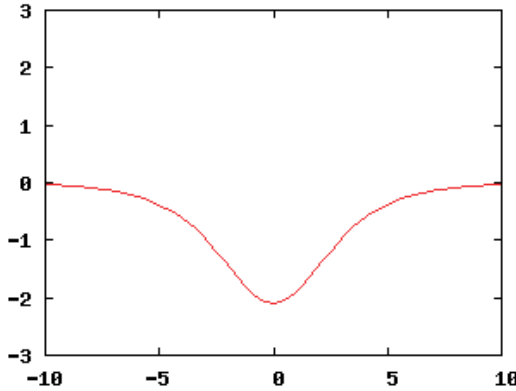


Figure 5.5: Schematic plot of the breather function. During time the solution curve expands and contract.

$$\phi(x, t) = 4 \arctan\left(\frac{\beta \sinh(\beta mx)}{\cosh(\beta mx)}\right). \quad (5.55)$$

Finally also a so-called breather solution can be derived when the case  $v = 0$  and  $m^2 < 1$  is considered;

$$-4 \arctan\left(\frac{\frac{\sqrt{1-\Omega^2}}{\Omega} \sin(\Omega t)}{\cosh x \sqrt{(1-\Omega^2)}}\right) \quad (5.56)$$

Here  $\Omega = \sqrt{1-m^2}$ . The breather is solution is named that way, because the solution (fig 5.5) contacts and expands continuously in time.

From now on we will concentrate on the kink and anti kink solutions.

### 5.3.3 Lorentz invariance and solutions

Let us recall the sine-Gordon equation, in shorthand notation,

$$\phi(x, t)_{tt} - \phi(x, t)_{xx} + \sin(\phi(x, t)) = 0 \quad (5.57)$$

In the static case it becomes,

$$-\phi(x, t)_{xx} + \sin(\phi(x, t)) = 0 \quad (5.58)$$

It is easy to see that this equation allows only two bound, i.e.  $\phi(x, t) \rightarrow 0 \text{ mod } 2\pi$  as  $x \rightarrow \infty$ , solutions.

$$\begin{aligned} \phi(x, t)^+ &= 4 \arctan(\exp(x - q)), \\ \phi(x, t)^- &= 4 \arctan(\exp(-(x - q))), \end{aligned} \quad (5.59)$$

Where we used  $\exp(-mq)$  and  $\exp(mq)$  as integration constants respectively. We see that these solutions satisfy our boundary condition and that the maximum modulo  $2\pi$  is attained at  $x = q$ . So  $q$  can be interpreted as our "  $\phi$  - packet" or "kink". The plus and minus signs refer to the positive and negative helicities.

We expect traveling waves so we define

$$\xi = x - ct \quad (5.60)$$

and use it to make the ansatz<sup>15</sup>,

$$\phi(x, t) = \phi(x - ct) = \phi(\xi) \quad (5.61)$$

We assume that  $c$  is positive from now on, this assumption is not a restriction. We can simply get the exact same solutions (equation 5.63 is not altered if  $\xi$  is replaced with  $\eta$ ). Additionally when  $c=0$  we also get the same solutions, but with the identity that  $1 - c^2 = 1$ . Now using the chain rule to obtain

$$\begin{aligned} \frac{\partial \phi(x, t)}{\partial x} &= \frac{\partial \xi}{\partial x} \frac{\partial \phi(\xi)}{\partial \xi} = \frac{\partial \phi(\xi)}{\partial \xi} \\ \frac{\partial^2 \phi(x, t)}{\partial x^2} &= \frac{\partial}{\partial x} \left( \frac{\partial \phi(\xi)}{\partial \xi} \right) = \frac{\partial \xi}{\partial x} \frac{\partial \phi(\xi)}{\partial \xi^2} = \frac{\partial \phi(\xi)}{\partial \xi^2} \\ \frac{\partial \phi(x, t)}{\partial x} &= \frac{\partial \xi}{\partial x} \frac{\partial \phi(\xi)}{\partial \xi} = -c \frac{\partial \phi(\xi)}{\partial \xi} \\ \frac{\partial^2 \phi(x, t)}{\partial x^2} &= \frac{\partial}{\partial x} \left( -c \frac{\partial \phi(\xi)}{\partial \xi} \right) = -c \frac{\partial \xi}{\partial x} \frac{\partial \phi(\xi)}{\partial \xi^2} = c^2 \frac{\partial \phi(\xi)}{\partial \xi^2} \end{aligned} \quad (5.62)$$

We get the sine-Gordon equation in the  $\xi$  variable,

$$(c^2 - 1)\phi(\xi)_{\xi\xi} + \sin(\phi(\xi)) = 0 \quad (5.63)$$

Upon comparison with equation 5.59 we get

$$\phi_c(\xi) = 4 \arctan \left( \frac{\pm}{(1 - c^2)^{\frac{1}{2}}} (x - q(t)) \right) \quad (5.64)$$

Here the subscript  $c$  refers to the traveling wave at speed  $c$ . Moreover  $q(t) = q(0) = ct$ , which is the position of the kink at time  $t$ . the width of this running kink is then  $(1 - c^2)^{\frac{1}{2}}$ . This Lorentz contraction is a result of the relativistic invariance of this equation which can most easily be understood by looking at the Lagrangian and Hamiltonian and their connection to the Klein-Gordon equation.

---

<sup>15</sup>Which is equivalent to the method of characteristics

### 5.3.4 Hamiltonian, Lagrangian and phase portrait

The sine-Gordon equation contains a lot of physical and mathematical concepts. The sine-Gordon is actually the beginning of the field theory, which describes the physical solutions of many particles in the context of a relativistic continuum. Most physical concepts are contained in the Lagrangian and Hamiltonian.

Recall once again the sine-Gordon equation, in the characteristic variable variable  $\xi$ ;

$$(1 - c^2)\phi(\xi)_{\xi\xi} = \sin(\phi(\xi)) \quad (5.65)$$

or equivalently

$$\phi(\xi)_{\xi\xi} = \frac{1}{(1 - c^2)} \sin(\phi(\xi)) \quad (5.66)$$

Let us find the Hamiltonian, in this setting;

$$\phi(\xi)_\xi = \frac{\partial H(\phi(\xi), \phi(\xi)_\xi)}{\partial(\phi(\xi)_\xi)} \quad (5.67)$$

and

$$\phi(\xi)_{\xi\xi} = \frac{1}{(1 - c^2)} \sin(\phi(\xi)) = \frac{-\partial H(\phi(\xi), \phi(\xi)_\xi)}{\partial(\phi(\xi))} \quad (5.68)$$

then we obtain, defining a new constant  $\mu$ ,

$$H(\phi(\xi), \phi(\xi)_\xi) = \frac{1}{2}(\phi(\xi)_\xi)^2 + \frac{1}{(1 - c^2)}(\cos(\phi(\xi))) + \mu \quad (5.69)$$

Better still is the Hamiltonian in  $x$  and  $t$  coordinates, as this gives more physical insight;

$$H(\phi(x, t)_t, \phi(x, t)_x, \phi) = \frac{1}{2}(\phi(x, t)_t^2 + \phi(x, t)_x^2 + 2(1 - \cos(\phi(x, t)))) + \alpha \quad (5.70)$$

Here  $\alpha$  is a constant.

In this case the Hamiltonian equations are as follows

$$\begin{aligned} \phi(x, t)_{tt} &= -\frac{\partial H((\phi(x, t), \phi(x, t)_t))}{\partial \phi(x, t)} = \phi(x, t)_{xx} - \sin(\phi(x, t)) \\ \phi(x, t)_t &= -\frac{\partial H((\phi(x, t), \phi(x, t)_t))}{\partial \phi(x, t)_t} \end{aligned} \quad (5.71)$$

We can now we can identify  $\frac{1}{2}\phi(x, t)_t^2$  as kinetic energy and  $\frac{1}{2}\phi(x, t)_x^2 + (1 - \cos(\phi(x, t)))$  as potential energy. Therefore the Lagrangian,  $L = T - V$  equals

$$\begin{aligned} L(\phi(x, t)_t, \phi(x, t)_x, \phi) &= -\frac{1}{2}(\phi(x, t)_x^2 - \phi(x, t)_t^2 + 2(1 - \cos(\phi(x, t)))) + \beta \\ & \quad (5.72) \end{aligned}$$

or equivalently

$$L(\phi(x,t)_t, \phi(x,t)_x, \phi) = -\frac{1}{2}(\phi(x,t)_x^2 - \phi(x,t)_t^2 + 4(\sin^2(\frac{\phi(x,t)}{2}))) + \beta \quad (5.73)$$

With  $\beta$  a constant.

Notice that the well-known Klein-Gordon Lagrangian (equation 5.75<sup>16</sup>) does not have the desired translational invariance dictated by our situation,

$$L_{KG}(\phi) \neq L_{KG}(\phi + 2\pi) \quad (5.74)$$

In our situation  $\phi(x,t)$  is the most simple non-trivial manifold, i.e. the unit circle  $S^1$ . Clearly the usual Klein-Gordon Lagrangian should be replaced by the Lagrangian stated in equation 5.73.

For small  $\phi(x,t)$  we can expand  $\sin^2(\phi(x,t))$  in first order, resulting in  $\sin^2(\phi(x,t)) \approx \phi(x,t)^2$ . Consequently equation 5.73 exactly reduces to equation 5.75. This has a simple interpretation; As the unit locally sphere looks flat the Lagrangian of the solution  $\phi(x,t)$  approaches the normal Klein-Gordon Lagrangian.

$$L_{KG}(\phi(x,t)_t, \phi(x,t)_x, \phi) = -\frac{1}{2}(\phi(x,t)_x^2 - \phi(x,t)_t^2) + \phi(x,t)^2 \quad (5.75)$$

To conclude this paragraph we examine the phase portrait of our system. Define  $\vec{x}(\xi) \equiv (\phi(\xi), \phi(\xi)_\xi)^T$ , using equation 5.65 and definitions above we obtain

$$\frac{d}{d\xi} \vec{x}(\xi) = F(\phi(\xi), \phi(\xi)_\xi) \quad (5.76)$$

Here  $F$  is a vector function with components  $\phi(\xi)_\xi$  and  $\frac{\sin(\phi(\xi))}{1-c^2}$ . Expanding  $F$  in first order around an equilibrium point,  $\widehat{\phi(\xi)}$ , results<sup>17</sup> in the linearized system;

$$\frac{d}{d\xi} \begin{bmatrix} \phi(\xi) \\ \phi(\xi)_\xi \end{bmatrix} = \begin{bmatrix} 0 & 1 \\ \frac{\cos(\widehat{\phi(\xi)})}{1-c^2} & 0 \end{bmatrix} \begin{bmatrix} \phi(\xi) \\ \phi(\xi)_\xi \end{bmatrix} \quad (5.77)$$

Referring to the definition of  $F$  we conclude that the equilibrium points with respect to the defined coordinates are  $(0, k\pi)$ ,  $k \in \mathbb{Z}$ . However recall that all points modulo  $2\pi$  are equivalent due to the translational invariance.

The sine-Gordon equation is a Hamiltonian system so every solution is a curve of constant energy. Moreover due to the symmetry of the equations, the curves representing the solution must be symmetric in both axes<sup>18</sup>.

---

<sup>16</sup>Remember that the expected mass, is put to one

<sup>17</sup>Note that the constant term in the first order expansion vanishes per definition of an equilibrium point

<sup>18</sup>The axis with respect to the defined coordinates

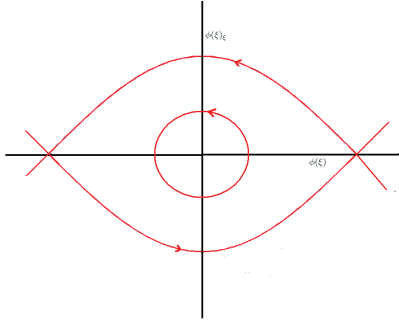


Figure 5.6: Schematic illustration of the phase portrait. Notice the periodic solutions around  $(0,0)$ . All the curves are of constant energy as the system is Hamiltonian. The heteroclinic connection are traveling wave solutions

Examining the eigenvalues of the linearized system around  $(0,0)$  in 5.77 yields  $\lambda^2 = \frac{1}{1-c^2}$ . When  $c^2 > 1$  we obtain eigenvalues that are purely imaginary. Notice that around the other two equilibrium points we get  $\lambda = \frac{1}{\sqrt{-1+c^2}}$ , giving a positive and negative real value of lambda (i.e.  $\lambda = \frac{1}{\sqrt{-1+c^2}}$  and  $\lambda = \frac{-1}{\sqrt{-1+c^2}}$ ). Consequently, the other points are saddle points in this case. This results in the phase portrait depicted in Figure 5.6. The points at  $\pm\pi$  are connected by heteroclinic orbits, which represent the traveling solutions. However it can be proven that the kink solutions are only stable when  $|c| < 1$  (see for example [4]). This is physically interpretable if we recall the relativistic invariance of the equation. In our notation  $c = 1$ , so from a physical point of view we could have expected stable solutions only to occur when  $c < 1$ .

If  $c^2 < 1$ , the eigenvalues of the linearized system around  $(0,0)$  are now the positive and negative real root of  $\lambda - \frac{1}{\sqrt{-1+c^2}} = 0$  and the eigenvalues around the other points are purely imaginary. It looks like the system has been translated ( $n\pi$  with  $n \in \mathbb{Z}$ ). Again we have heteroclinic connections that represent traveling waves. It can be shown that these traveling waves are stable.



## Chapter 6

# Perturbation of the sine-Gordon equation

In the previous chapter we encountered the sine-Gordon and its solutions. This was an example of a Hamiltonian system. In this chapter we add a energy-dissipative term to the equation, resulting in an equation that cannot be solved in general. We will therefore assume that the dissipative terms are small and subsequently apply perturbation methods to study the behavior of kink and antikink solutions. We find traveling solutions for small perturbations, using the Melnikov function and Fenichel's theorem

### 6.1 General starting point

We study the following perturbed sine-Gordon equation

$$\phi(x, t)_{xx} - \phi(x, t)_{tt} + \sin(\phi(x, t)) = \epsilon(\iota - \kappa\phi(x, t)_t) \quad (6.1)$$

In this equation  $\epsilon, \iota$  and  $\kappa$  are real constants and  $\epsilon \geq 0$  for definiteness. in the case  $\epsilon = 0$  we get the sine-Gordon equation with its Hamiltonian structure. Using standard perturbation series, i.e.  $\phi(x, t) = \phi_0(x, t) + \epsilon\phi_1(x, t) + \epsilon^2\phi_2(x, t) \dots$  we get,

$$\begin{aligned} O(1) \quad & \phi_0(x, t)_{xx} - \phi_0(x, t)_{tt} + \sin(\phi_0(x, t)) = 0 \\ O(\epsilon) \quad & \phi_1(x, t)_{xx} - \phi_1(x, t)_{tt} + \sin(\phi_1(x, t)) + \kappa\phi_0(x, t)_t - \iota = 0 \end{aligned} \quad (6.2)$$

Of course the  $O(1)$  equation is just the sine-Gordon equation. If we use the

(anti)kink solutions (with  $c$  positive) we get for the  $O(\epsilon)$  equation

$$\begin{aligned} \phi_1(x, t)_{xx} - \phi_1(x, t)_{tt} + \sin(\phi_1(x, t)) + \kappa\phi_1(x, t)_t - \iota &= 0 \\ \phi_1(x, t)_{xx} - \phi_1(x, t)_{tt} + \sin(\phi_1(x, t)) + \frac{-4c\kappa}{\sqrt{(c^2-1)}} \frac{\exp(\frac{x-ct}{\sqrt{c^2-1}})}{1+\exp(\frac{2(x-ct)}{\sqrt{c^2-1}})} - \iota &= 0 \end{aligned} \quad (6.3)$$

This equation cannot be solved, therefore we will apply other methods.

## 6.2 Traveling waves with speed $c=1$

When we look at solutions with  $c=1$ , i.e.  $\xi = x - t$ <sup>1</sup> we can find a closed form if  $\iota < -1$ . In this case we do not need perturbation theory. In other words we will study the equation

$$\phi(x, t)_{xx} - \phi(x, t)_{tt} + \sin(\phi(x, t)) + \kappa\phi(x, t)_t + \mu = 0 \quad (6.4)$$

Where  $\mu = -\iota > 1$ . We specify our traveling-wave Ansatz as seen above <sup>2</sup>:

$$\xi \equiv \pm x - t, \quad \phi(x, t) = u(\xi) - \pi. \quad (6.5)$$

Accordingly we use the chain rule to see that

$$\begin{aligned} \frac{\partial^2}{\partial x^2} &= \frac{\partial}{\partial x} \left( \frac{\partial \xi}{\partial x} \frac{\partial}{\partial \xi} \right) = \frac{\partial}{\partial x} \left( \frac{\partial}{\partial \xi} \right) = \frac{\partial^2}{\partial \xi^2} \\ \frac{\partial^2}{\partial t^2} &= \frac{\partial}{\partial t} \left( \frac{\partial \xi}{\partial t} \frac{\partial}{\partial \xi} \right) = \frac{\partial}{\partial t} \left( -\frac{\partial}{\partial \xi} \right) = \frac{\partial^2}{\partial \xi^2} \end{aligned} \quad (6.6)$$

Consequently plugging the Ansatz in (6.4) results into

$$\kappa u(\xi)_\xi = \mu - \sin(u(\xi)) \quad (6.7)$$

Assuming  $u(\xi)_\xi$  is not identically zero, we separate the equation

$$d\xi = \frac{\kappa du}{(\mu - \sin(u(\xi)))} \quad (6.8)$$

Integrating then yields<sup>3</sup>

$$\xi - \xi_0 = \kappa \int_{u_0}^u \frac{ds}{\mu - \sin s} \quad (6.9)$$

---

<sup>1</sup>Note that this are characteristics

<sup>2</sup>Where the  $\pi$  is introduced to give the sine term of the sine-Gordon equation a minus sign, which will turn out to be useful in the following transformations. It also fixes the solution with respect to obvious boundary conditions

<sup>3</sup>As  $\mu > 1$  the denominator is positive

Observe that

$$\sin(\alpha) = 2 \sin(\alpha) \cos(\alpha) = \frac{2 \frac{\sin(\alpha)}{\cos(\alpha)}}{\cos^2(\alpha)} = \frac{2 \tan(\alpha)}{1 + \tan^2(\alpha)}, \quad (6.10)$$

and that

$$\cos(2\alpha) = \frac{\cos^2(\alpha) - \sin^2(\alpha)}{\cos^2(\alpha) + \sin^2(\alpha)} = \frac{1 - \tan^2(\alpha)}{1 + \tan^2(\alpha)} \quad (6.11)$$

As a result we obtain

$$\sin(4\alpha) = 2 \sin(2\alpha) \cos(2\alpha) = \frac{4 \tan(\alpha)(1 - \tan^2(\alpha))}{(1 + \tan^2(\alpha))^2}. \quad (6.12)$$

We are looking for traveling waves in the perturbed system. Consequently we make the ansatz that  $u(\xi) = 4 \arctan(Z(\xi))$ . Plugging the ansatz into equation 6.7 and using equation 6.12 we obtain

$$4\kappa \frac{Z(\xi)_\xi}{1 + Z(\xi)^2} = \mu - 4 \frac{Z(\xi)(1 - Z(\xi)^2)}{(1 + Z(\xi)^2)^2} \quad (6.13)$$

This equation can easily be simplified by introducing a new variable  $p(\xi)$ . Define  $Z(\xi) = p(\xi) + \sqrt{1 + p(\xi)^2}$ , subsequently the previous equation reduces to

$$2\kappa p(\xi)_\xi = 2p(\xi) + \mu(1 + p(\xi)^2) \quad (6.14)$$

Notice that due to our translational invariance these transformations are legitimate. Even when  $|p(\xi)|$  diverges at some point, the continuity (and smoothness) of  $u(\xi)$  at that point is preserved; In the worst case, one of the right or left limits is  $\infty$  and other is  $-\infty$ . In this case  $p(\xi) \rightarrow \pm\infty$  implies  $F \rightarrow \infty, 0$  respectively, whence  $g \rightarrow 0 \bmod 2\pi$  in either case.

Putting all definitions from above together we see that we are actually looking for solutions of the form

$$\phi^\pm(x, t) = 4 \arctan(p(\pm x - t) + \sqrt{1 + p(\pm x - t)^2}) - \pi. \quad (6.15)$$

where we denoted the corresponding solutions with  $\xi = \pm x - t$  as  $\phi^\pm$ .

Only for  $\mu \leq 1$  the solutions  $p_\pm = -\mu^{-1} \pm \sqrt{\mu^{-2} - 1}$ , of the second degree equation  $p(\xi)^2 + \frac{2p(\xi)}{\mu} + 1 = 0$  are real and therefore give constant solutions. We are interested in nonconstant solutions and so we separate equation 6.14<sup>4</sup> to obtain

$$d\xi = \frac{2\kappa}{\mu} \frac{dp}{(p(\xi)^2 + \frac{2}{\mu}p(\xi) + 1)} \quad (6.16)$$

---

<sup>4</sup>This can be done piecewise on each interval where  $p(\xi)_\xi$  keeps its sign

Notice that due to the fact that  $\mu > 1$  the discriminant of the equation  $p^2 + 2p\mu + 1 = 0$  is negative. Additionally  $p_{\pm}$  are complex conjugated and do not vanish for any value of  $p(\xi)$ . We rewrite equation 6.14 by setting  $h(\xi) = \frac{p(\xi)\mu+1}{\sqrt{\mu^2-1}}$ . Using  $h^2 + 1 = p^2\mu^2 + 2\mu p + \mu^2$  we get

$$d\xi = d\xi = \frac{2\kappa}{\sqrt{\mu^2 - 1}} \frac{dh}{1 + h^2} \quad (6.17)$$

The resulting equation can subsequently be integrated to give

$$\xi - \xi_0 = 2\kappa \arctan h / \sqrt{\mu^2 - 1} \quad (6.18)$$

Therefore

$$p(\xi) = -\mu^{-1} + \frac{1}{\sqrt{1 - \mu^{-2}}} \tan\left(\frac{\sqrt{\mu^2 - 1}}{2\kappa}(\xi - \xi_0)\right) \quad (6.19)$$

Here  $\xi_0$  is an integration constant.

Notice that the solution found in equation 6.19 is a periodic function with period  $\tau = \frac{2\pi\kappa}{\sqrt{\mu^2-1}}$ . In fact, if we chose  $\xi_0 = 0$  for simplicity, we see that as  $\xi$  varies from  $-\tau/2$  to  $\tau/2$ ,  $p(\xi)$  varies from  $-\infty$  to  $\infty$ . Subsequently  $Z(\xi)$  varies from 0 to  $\infty$  and  $u(\xi)$  varies from 0 to  $2\pi$ .

The solutions have the desired property that  $\phi^{\pm}(x+\tau, t) = \check{\phi}^{\pm}(x, t) \pm 2\pi$ . and can be proven to be stable.

The derived identities describe arrays of evenly spaced kinks traveling with velocities  $\pm 1$ . The condition that  $\mu > 1$  is physically also interpretable. The driving force in the equation, i.e.  $\mu$ , should be large enough to keep the wave going. Otherwise they will die out due to the friction and rerun to the fixed point solutions  $\phi(x, t) = -\arcsin(\mu)$  and  $\phi(x, t) = \arcsin(\mu) + \pi$ . Note that these points only exist when  $|\mu| \leq 1$ . So we have obtained traveling wave solutions and have found the value of the driving force needed overcome the friction and keep the wave going.

### 6.3 Traveling waves and the Melnikov function

Let us return to the equation 6.1. We look at stable kink solutions<sup>5</sup> with initial condition  $x_0 = 0$ , i.e.

$$\phi_c(x, t) = 4 \arctan(\exp(\zeta)) \quad \text{with } \zeta = \frac{x - ct}{\sqrt{1 - c^2}} \quad (6.20)$$

Equation 6.1 is transformed in new variables  $\zeta$ ,  $t$  and  $\phi(x, t) = u(\zeta, t)$  to simplify notation. We obtain

$$\begin{aligned} u(\zeta, t)_{tt} - 2 \frac{c}{\sqrt{1 - c^2}} u(\zeta, t)_{\zeta t} - u(\zeta, t)_{\zeta\zeta} + \sin(u(\zeta, t)) = \\ \epsilon(\iota - \kappa u(\zeta, t)_t + \frac{c\kappa}{\sqrt{1 - c^2}} u(\zeta, t)_\zeta) \end{aligned} \quad (6.21)$$

using that

$$\begin{aligned} \frac{\partial}{\partial t} &\longrightarrow \frac{\partial}{\partial t} - \frac{c}{\sqrt{1 - c^2}} \frac{\partial}{\partial \zeta} \\ \frac{\partial}{\partial x} &\longrightarrow \frac{1}{\sqrt{1 - c^2}} \frac{\partial}{\partial \zeta} \end{aligned} \quad (6.22)$$

For the traveling wave solutions (i.e.  $u \sim u(\zeta)$ ) the above equation becomes

$$u(\zeta, t)_{\zeta\zeta} - \sin(u(\zeta, t)) = -\epsilon(\iota + \frac{c\kappa}{\sqrt{1 - c^2}} u(\zeta, t)_\zeta) \quad (6.23)$$

**Theorem 1** For  $\kappa > 0$  and  $\iota$  fixed,  $\kappa, \iota \in \mathbb{R}$ , there exist an unique smooth curve of parameter  $\epsilon \mapsto c_\epsilon$  and an unique curve of wave shapes  $\epsilon \mapsto u_\epsilon(\zeta)$  such that for small  $\epsilon$ , the waves are traveling solution of equation 6.23 with  $c_\epsilon = c$ . Moreover

$$\lim_{\epsilon \rightarrow 0} u_\epsilon(\zeta) = 4 \arctan(\exp(\zeta)) \quad \text{where } \zeta = \frac{x - c_0 t}{\sqrt{1 - c_0^2}} \quad (6.24)$$

where  $c_0$  is a solution of the equation

$$3\pi\iota + 12 \frac{\kappa c}{\sqrt{1 - c^2}} = 0 \quad (6.25)$$

**Proof 1** We write the problem in a system(slow system) and obtain

$$\begin{aligned} x(\zeta) &= u(\zeta)_\zeta \\ y(\zeta) &= x(\zeta)_\zeta = u(\zeta)_{\zeta\zeta} = \sin(u(\zeta)) - \epsilon(\iota + \frac{\kappa c}{\sqrt{1 - c^2}} x) \end{aligned} \quad (6.26)$$

When we look at the fast variable<sup>6</sup>,  $\sigma\epsilon = \zeta$ , we can write the system as

---

<sup>5</sup>which means that  $|c| < 1$

<sup>6</sup>Note that this corresponds with the concept of scaling, the variable is basically scaled to obtain the fast variable.consequently  $\frac{\partial}{\partial \zeta} = \frac{\partial \sigma}{\partial \zeta} \frac{\partial}{\partial \sigma} = \frac{1}{\epsilon} \frac{\partial}{\partial \sigma}$

$$\begin{aligned} x(\sigma) &= \epsilon u(\sigma)_\sigma \\ y(\sigma) &= \epsilon(\sin(u(\sigma)) - \epsilon(\iota + \frac{\kappa c}{\sqrt{1-c^2}}x)) \end{aligned} \tag{6.27}$$

In the asymptotic case,  $\epsilon = 0$ , this slow system reduces to

$$\begin{aligned} x(\zeta) &= u(\zeta)\zeta \\ y(\zeta) &= u(\zeta)_{\zeta\zeta} = \sin(u(\zeta)) \end{aligned} \tag{6.28}$$

whereas the fast system reduces to

$$\begin{aligned} u(\sigma) &= u(\sigma)_0 \\ x &= x(\sigma)_0 \end{aligned} \tag{6.29}$$

Notice that we are dealing with a nonsingular perturbation problem<sup>7</sup>. If we had added an other perturbation term like  $u(\zeta)_{\zeta\zeta\zeta}$ , we would get a singularly perturbed problem, that can be written in the form<sup>8</sup>;

$$\begin{aligned} \dot{a} &= f(a, b, \epsilon) \\ \dot{b} &= \epsilon g(a, b, \epsilon)_0 \end{aligned} \tag{6.30}$$

Although the system is then singularly perturbed, we can still analyze it in the same way as presented here using Fenichel's theorem( [6],[7],[9],[10],[14],[17]).

Let us return to the system we are considering. From the above discussion (especially equation 6.26) it is clear that the dynamics is given by

$$\begin{aligned} u_\zeta &= x \\ u_{\zeta\zeta} &= y = \sin(u) + \epsilon h_1(u, x, 0) + O(\epsilon^2) \end{aligned} \tag{6.31}$$

Where  $h_1(u, x, \epsilon)$  satisfies

$$h_1(u, x, \epsilon) = -(\iota + \frac{\kappa c}{\sqrt{1-c^2}}x) \tag{6.32}$$

We can determine the Hamiltonian of this perturbed Hamiltonian system in the  $\zeta$  variable. Using the chain rule we see that for  $\zeta = \frac{\xi}{\sqrt{1-c^2}}$  it holds that

---

<sup>7</sup>i.e. the system can be approximated by setting  $\epsilon = 0$ .

<sup>8</sup>where I used the dot notation again

$$\begin{aligned}\frac{\partial}{\partial \xi} &= \frac{\partial \zeta}{\partial \xi} \frac{\partial}{\partial \zeta} = \frac{1}{\sqrt{1-c^2}} \frac{\partial}{\partial \zeta} \\ \frac{\partial^2}{\partial \xi^2} &= \frac{\partial \zeta}{\partial \xi} \left( \frac{1}{\sqrt{1-c^2}} \frac{\partial}{\partial \zeta} \right) = \frac{1}{1-c^2} \frac{\partial^2}{\partial \zeta^2}\end{aligned}\tag{6.33}$$

As a result equation 5.65 reduces to

$$\phi(\zeta)_{\zeta\zeta} = \sin(\phi(\zeta)) \tag{6.34}$$

In the same manner as above we find the Hamiltonian;

$$H(\phi(\zeta), \phi(\zeta)_\zeta) = \frac{1}{2}(\phi(\zeta)_\zeta)^2 + (\cos(\phi(\zeta))) + \mu \tag{6.35}$$

In this situation we have a non-Hamiltonian perturbation<sup>9</sup>, i.e.

$$G(u, x, \epsilon) = \epsilon(0, h_1(u, x, 0) + O(\epsilon^2)) \tag{6.36}$$

In the case that  $\epsilon = 0$  we get the sine-Gordon equation, with heteroclinic solution  $u_0(\zeta) = 4 \arctan(\exp(\zeta))$ . This solution has a well defined  $u_0(\zeta)_\zeta$ ;

$$u_0(\zeta)_\zeta = \frac{4 \exp(\zeta)}{1 + \exp(2\zeta)} = \frac{2}{\frac{1}{2}(\exp(-\zeta) + \exp(\zeta))} = 2 \operatorname{sech}(\zeta) = x_0(\zeta). \tag{6.37}$$

Subsequently we use a Melnikov argument. Calculating the Melnikov function ([5], [6], [10], [13], [17]) is easy;

$$M(\epsilon) = \int_{-\infty}^{\infty} \nabla H(u_0(\zeta)) \cdot G(u_0(\zeta), x_o(\zeta), 0) d\zeta + O(\epsilon) \tag{6.38}$$

which results, using the explicit solution calculated above, into

$$\begin{aligned}M(0) &= \int_{-\infty}^{\infty} \nabla - \iota x_o(\zeta) - \frac{\kappa c}{\sqrt{1-c^2}} x_0(\zeta)^2 d\zeta \\ &= -2\pi\iota - 8 \frac{\kappa c}{\sqrt{1-c^2}}\end{aligned}\tag{6.39}$$

For completeness we want to point out that the Melnikov function can also be directly calculated from an alternative definition ([5], page 187 equation 4.5.6) Write equation 6.31 as

$$\frac{d}{d\zeta} x = f(x) + \epsilon g(x) \quad x = (u(\zeta), u(\zeta)_\zeta)^T \tag{6.40}$$

Then we get

$$M(\epsilon) = \int_{-\infty}^{\infty} f(q^0(\xi - \xi_0)) \wedge g(q^0(\xi - \xi_0)) d\xi \tag{6.41}$$

---

<sup>9</sup>Of course; this is exactly the dissipative term

Where  $q^0$  refers to the orbits and the wedge product is defined by  $a \wedge b = a_1 b_2 - a_2 b_1$ <sup>10</sup>. Consequently

$$\begin{aligned} M(0) &= \int_{\infty}^{\infty} \nabla - \iota x_o(\zeta) - \frac{\kappa c}{\sqrt{1-c^2}} x_0(\zeta)^2 d\zeta \\ &= -2\pi\iota - 8 \frac{\kappa c}{\sqrt{1-c^2}} \end{aligned} \tag{6.42}$$

It follows from the Melnikov-formalism that the heteroclinic connections between the fixed point solutions  $\arcsin(\epsilon\iota)$  and  $\arcsin(\epsilon\iota) + 2\pi$  exist when  $M(\epsilon) = 0$ . Hence we obtain for the lowest order

$$\begin{aligned} 0 &= -2\pi\iota - 8 \frac{\kappa c}{\sqrt{1-c^2}} \\ 0 &= 3\pi\iota + 12 \frac{\kappa c}{\sqrt{1-c^2}} \end{aligned} \tag{6.43}$$

This gives the existence of a curve of heteroclinic connections and a curve of paramors specified in the theorem.

□

This truly represents the strength of the Melnikov function. Although we cannot solve the system analytically, we do know when there are heteroclinic connections, representing the traveling waves. Moreover we see that most of the physics and mathematic is contained in the speed of the wave. Physically this also seems plausible. Adding a small dissipative friction term, mainly changes the speed of the wave and when this term goes to zero solution should look the same as in the unperturbed system.

---

<sup>10</sup>Notice that this is the projection on the normal

# Chapter 7

## Conclusion

Results from the experiments designated to measure the shear modulus  $G$  and the bulk modulus  $B$  show linear response. This confirms our elastic model and its resulting equations. Consequently the quantities pertaining to our measurements can legitimately be linked to  $G$  and  $B$ .

The data obtained from the experiments concerning the shear modulus seems to agree with the prediction that  $G \sim \sqrt{\Delta\phi}$ . The plot of  $G$  can legitimately be fitted with a square root function. Moreover the fit parameters make sense, showing a value of the critical packing fraction  $\phi_c$  equal to 0.847. However in order to rigorously rule out other power laws, with exponents close to 0.5, more measurements are required.

Unfortunately the results from the measurement concerning  $B$  are not convincing enough to make a valid statement about the prediction that  $B$  is essentially independent of  $\phi$  near  $\phi_c$ . We are not able to make measurements at packing fractions near the critical packing fraction. In the region of  $\phi$ , where we are able to measure the bulk modulus, we find that  $B$  has a linear dependence on the packing fraction. It may well be that at lower packing fractions  $B$  becomes independent of  $\phi$ . More measurements in a slightly altered setup are needed to obtain a decisive answer.

In our analysis of systems consisting of two layers of bubbles in a Taylor-Couette geometry we find the sine-Gordon equation, if we take the limit of a Hamiltonian approximation. The sine-Gordon has so-called soliton solutions, representing traveling waves. If we subsequently add a dissipative term to the equation we are able to find an explicit wave solution traveling with speed equal to unity. Moreover, when the dissipative term can be regarded as a perturbation we can confirm the existence of traveling wave solutions.



# Chapter 8

## Appendix

### 8.1 A1:Image analysis

We extract our crucial control parameter  $\phi$ , as well as the average contact number  $Z$  from the experimental images by advanced image analysis, see Figure 8.1). The procedure is straight forward. We first binarize the image, after which both the bubble centers and the interstices appear bright. We then remove the interstices by morphological operations and end up with an image consisting of bright bubble centers. We dilate these centers and add up a negative of the original binary image, in which the bubbles appear as bright rings, to arrive at the final image. In this final image the bubbles are represented by bright discs against a black background. From this image we can readily calculate the area fraction of the white fringes, i.e. $\phi$ . We can locate the center of mass of each bubble in the image, and after Delaunay triangulation and a subsequent removal of bond vectors for non-touching bubbles, we obtain the contact network of the bubbles in the image, from which we calculate  $Z$ . However as the values of  $Z$  are not convincing enough,  $Z$  is not referred to in the rest of this thesis.

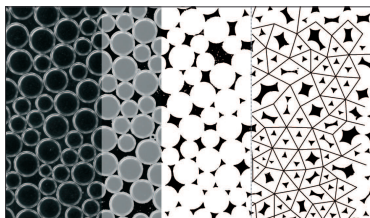


Figure 8.1: *Illustration of the most important stages of the image analysis, shown from left to right. Starting from the original image (presented on the far left), the binarized and the final version are shown respectively. The last stage shows the final stage with the triangulation.*

## 8.2 A2: *idl* -code shear modulus

```
fl = file_lines('z:\slager\shear relax\68torque.txt')
data = fltarr(fl)
openr, 1, 'z:\slager\shear relax\68torque.txt'
readf,1, data
close, 1
x = findgen(f1/23-14)
y = fltarr(f1/23-14)
err =1+0*x
parr=fltarr(f1/200)
Carr=fltarr(f1/200)
phiarr= fltarr(f1/200)
count=0
for i =0, f1/200.-1 do begin
y = data(i*200:(i+1)*200-15)
a=[1,2,y(184)]
result=mpfitexpr('p(0)*(exp(-(x)*(p(1))))+p(2)',x,y,err,a,/quiet)
p=[result(0), 1/result(1), result(2)]

tmpnum=string(i)
filename='figuur68.' + tmpnum
print,filename
set_plot,'ps'
device,filename = 'Z:\slager\anshaer\' + filename + '.eps',/encapsulated
plot, x, y, psym=4
oplot, x, p(0)*(exp(-(x)/(p(1))))+p(2)
device,/close
set_plot,'win'
wait, .5
if p(1) lt 30 then begin
parr(count) = p(1)
count=count+1
endif
Carr(i)=p(2)
endfor

for j=0,15.-2 do begin
phiarr(j)=-3+j
endfor

for j=0,1 do begin
phiarr(j+14)=9-j
endfor

for j=0,1 do begin
```

```

phiarr(j+16)=6-j
endfor

for j=0,4 do begin
phiarr(j+18)=6+j
endfor

filename2='eindresultaatoverallfit68'
set_plot,'ps'
device,filename = 'Z:\slager\anshaer\'+filename2+'.eps',/encapsulated
plot, phiarr, Carr, psym=4
b=[0.5,0.02]
line=mpfitexpr('p(1)*x + p(0)',phiarr,Carr,err,b)
h=[line(0), line (1)]
oplot, phiarr, h(1)*phiarr + h(0)
device,/close
set_plot,'win'
print, mean(parr(0:count-1))
print, h
print, variance(parr)

end

```

### 8.3 A3: *idl* -code bulk modulus

```

temp = file_lines('Z:\slager\bulk\73torque.txt')
data = fltarr(temp)
openr, 1, 'Z:\slager\bulk\73torque.txt'
readf,1, data
close, 1
x = findgen(temp/16-14)
y = fltarr(temp/16-14)
err =1+0*x
parr=fltarr(temp/300)
Carr=fltarr(10)
torquearr= fltarr(temp/300)
y = data(0:300-15)
a=[1,2,y(280)]
result=mpfitexpr('p(0)*(exp(-(x)*(p(1))))+p(2)',x,y,err,a)
p=[result(0), 1/result(1), result(2)]
Carr(0)=p(2)
plot, x, y,psym=4
oplot, x, p(0)*(exp(-(x)/(p(1))))+p(2)

filename='bulk73. 0'

```

```

print,filename
set_plot,'ps'
device,filename = 'Z:\slager\anbulk\' +filename+'.eps',/encapsulated

plot, x, y
oplot, x, p(0)*(exp(-(x)/(p(1))))+p(2)

device,/close
set_plot,'win'

wait,2

for i =1, 9 do begin

y = data(i*300:(i+1)*300-15)
a=[-1,2,y(280)]
result=mpfitexpr('p(0)*(exp(-(x)*(p(1))))+p(2)',x,y,err,a)
p=[result(0), 1/result(1), result(2)]
plot, x, y,psym=4
oplot, x, p(0)*(exp(-(x)/(p(1))))+p(2)

tmpnum=string(i)
filename='bulk73.' + tmpnum
print,filename
set_plot,'ps'
device,filename = 'Z:\slager\anbulk\' +filename+'.eps',/encapsulated

plot, x, y
oplot, x, p(0)*(exp(-(x)/(p(1))))+p(2)

device,/close
set_plot,'win'

wait,2
parr(i)=p(1)
Carr(i)=p(2)
endfor
temp2 = file_lines('Z:\slager\bulk\73eerste10.txt')
torqueapplied = fltarr(temp2)
openr, 2, 'Z:\slager\bulk\73eerste10.txt'
readf,2, torqueapplied
close, 2
filename3='bulkrelaxeerwaardentegentorque73(eerste10).'
set_plot,'ps'
device,filename = 'Z:\slager\anbulk\' +filename3+'.eps',/encapsulated

```

```

device,/close
set_plot,'win'

filename2='eindresultaatoverallfit73'
set_plot,'ps'
device,filename = 'Z:\slager\anbulk\' + filename2 + '.eps',/encapsulated
plot, torqueapplied,Carr,psym=4
b=[-1200,1000]
line=mpfitexpr('p(1)*x + p(0)',torqueapplied,Carr,err,b)
h=[line(0), line (1)]
oplot, torqueapplied, h(1)*torqueapplied + h(0)
device,/close
set_plot,'win'
print, h
print, variance(Carr)
end

```

## 8.4 Acknowledgements

I wish to thank my thesis supervisors prof.dr.M van Hecke and dr. V. Rottschäfer for their motivating and enthusiastic guidance, during the past three months. Despite their busy schedules they always managed to make time to give tips and help me solving my problems.

I also want to thank Gijs Katgert for helping me with the experiments and Joshua Dijksman and Kiri Nichol for their technical support. Additionally I thank prof.dr.ir. W. van Saarloos for his tips concerning the Frenkel-Kontorova model and the sine-Gordon equation.

Last, but certainly not least, I want to thank my family for their magnificent support. Knowing that they will always help me overcome every setback I encounter, truly is a blessing.



# Bibliography

- [1] R.P. Feynman, The Feynman lectures on physics volume 2, Addison-wesley, Massachusetts Sixth edition, 1977
- [2] B. Lautrup, Physics of continuous matter Institute of Physics publishing, Bristol and Philadelphia First edition, 2005
- [3] C. S. OHern, Leonardo E. Silbert,Andrea J. Liu, Sidney R. Nagel, Jamming at zero temperature and zero applied stress: The epitome of disorder, Phys. Rev. E 68, 011306 , 2003
- [4] M.H. Holmes Introduction to Perturbation Methods, Springer, New York, Second edition, 1995
- [5] J. Guckenheimer, P. Holmes Nonlinear Oscillations, Dynamical systems and Bifurcations of Vector fields, Springer, New York Fifth edition, 1983
- [6] O.D. Anosova, On Invariant Manifolds in Singularly Perturbed Systems, Journal of Dynamical and Control Systems, Volume 5, 1999, 501-507
- [7] C.K.R.T. Jones, Geometric Singular Perturbation Theory, Session on Dynamical Systems, 1994 Bristol and Philadelphia
- [8] G. Derks, A. Doelman, S.A. van Gils, H. Susanto, Stability analysis of  $\pi$ -kinks in a  $0 - \pi$  Josephson junction, SIAM J. Appl. Dyn. Syst. , Volume 6 ,Issue 1
- [9] G.Derks , A. Doelman, S.A. van Gils , T.Visser, Travelling waves in a singularly perturbed sine-Gordon equation, Physica D: Nonlinear Phenomena Volume 180, Issues 1-2, 1 June 2003, Pages 40-70
- [10] P. Szmolyan, Heteroclinic Orbits in Singularly Perturbed Differential Equations, IMA preprint series,1989
- [11] G. Fiore, Some explicit travelling-wave solutions of a perturbed sine-Gordon equation, Preprint Matematica e Applicazioni, Universita' di Napol, 2007

- [12] G. Fiore, On soliton and other travelling-wave solutions of a perturbed sine-Gordon equation, Preprint Matematica e Applicazioni, Universita' di Napol, 2007
- [13] A. Fedorova, M. Zeitlin, Melnikov functions and Symplectic Topology, 1997,
- [14] R.A. Gardner, An invariant-manifold analysis of electrophoretic traveling waves, Journal of Dynamics and Differential Equations, Springer Netherlands, 1040-7294 (Print) 1572-9222 (Online), Issue Volume 5, Number 4, 1993 Pages 599-606
- [15] M. Bartuccelli,P. L. Christiansen,N. F. Pedersen, M. P. Soerensen, Prediction of chaos in a Josephson junction by the Melnikov-function technique, Phys. Rev. B 33, 4686 - 4691,1986
- [16] Infeld, E. and Rowlands, G. Nonlinear Waves, Solitons, and Chaos, 2nd edition, Cambridge University Press,Cambridge, England, 2000.
- [17] Jane Cronin, Robert E. O'Malley, Analyzing multiscale phenomena using singular perturbation methods, American Mathematical society,Baltimore,1988,